MEMS TUNABLE SI-BASED EVANESCENT-MODE CAVITY FILTERS: DESIGN, OPTIMIZATION AND IMPLEMENTATION

A Dissertation

Submitted to the Faculty

of

Purdue University

by

ZhengAn Yang

In Partial Fulfillment of the

Requirements for the Degree

of

Doctor of Philosophy

August 2019

Purdue University

West Lafayette, Indiana

THE PURDUE UNIVERSITY GRADUATE SCHOOL
STATEMENT OF DISSERTATION APPROVAL

Dr. Dimitrios Peroulis, Chair

School of Electrical and Computer Engineering

Dr. Dan Jiao

School of Electrical and Computer Engineering

Dr. Byunghoo Jung

School of Electrical and Computer Engineering

Dr. David Janes

School of Electrical and Computer Engineering

Approved by:

Dr. Dimitrios Peroulis

Head of the School Graduate Program

This dissertation is dedicated to my family for all their love and support.

ACKNOWLEDGMENTS

I would like to thank my advisor Dimitrios Peroulis for all his valuable guidance and support during the course of this work. I consider it a true privilege to work with him on a variety of topics in the areas of RF-MEMS. I am also grateful to Prof. Byunghoo Jung, Prof. David Janes and Prof. Dan Jiao for serving on my advisory committee.

I would like to acknowledge the current and former graduate students and post-doctoral researchers who have integrally contributed to the accomplishments of the past years: Dr. Hjalti Sigmarsson, Dr. Juseop Lee, Dr. Tsung-Chieh Lee, Dr. Dimitra Psychogiou, Dr. Xiaoguang Liu, Dr. Wesley Allen, Dr. Juan Zeng, Dr. Mohammad Abu Khater, Dr. Jin Li, Dr. Yu-Chen Wu, Dr. Mark Hickle, Kaiyuan Zeng, Michael Sinanis, Mahmoud Abdelfattah. The staff members at the Birck Nanotechnology Center deserve my sincere thanks as well.

TABLE OF CONTENTS

Page

Page

LIST OF TABLES

LIST OF FIGURES

Figure Page

Figure Page

ABSTRACT

Yang, ZhengAn PhD, Purdue University, August 2019. MEMS Tunable Si-Based Evanescent-Mode Cavity Filters: Design, Optimization and Implementation. Major Professor: Dimitrios Peroulis.

The allocated frequency bands for the incoming fifth generation (5G) wireless communication technologies spread broadly from sub 6 GHz to K and potentially W bands. The evolution of the future generations toward higher frequency bands will continue and presents significant challenges in terms of excessive system complexity, production and maintenance costs. Reconfigurable radio architecture with frequency-tunable components is one of the most feasible and cost-effective solutions to meet such challenges. Among these technologies, evanescent-mode (EVA) cavity tunable resonator have demonstrated many of the needed features such as wide tunability, low loss and high linearity. Such a technology typically employs a movable membrane that controls the resonant frequency of a post-loaded cavity.

The first part of this work focuses on advancing such technology into the mm-wave frequency bands and beyond. Manufacturing tolerance and tuner performance are the two main limiting factors addressed here. This work develops a cost-effective micro-fabrication and package assembly flow which addresses the manufacturing related limitations. On the other hand, introducing micro-corrugated diaphragms and gold-vanadium co-sputtered thin film deposition technology, significantly reduces (4×) the tuning voltage and enhances tuning stability (7×). We demonstrate a tunable two-pole band-pass filter (BPF) prototype as the first EVA cavity tunable filter operating in the K-Ka band.

The second part of this work extensively discusses an optimal RF design flow based on the developed manufacturing technology. It considers all technology constrains and allows the actualization of a high Q transfer function with minimum bandwidth variation within

an octave tuning range. Moreover, a new fully passive input/output feeding mechanism that facilitates impedance matching over the entire tuning range is presented. The devised RF methodology is validated through the design and testing of a two-resonator BPF. Measurements demonstrate a tuning range between 20-40 GHz, relative bandwidth of 1.9%-4.7%, and impedance matching over the entire tuning range which is upto 2× better than previously reported state-of-the-art MEMS tunable filters of this type.

The third part of this work further advances the technology by proposing the first MEMS-based low-power bi-directional EVA tuning approach that employs both the main bias circuitry as well as a new corrective biasing technique that counteracts viscoelastic memory effects. The two key enabling technologies are extensively discussed: a) a new metal-oxide-metal (MOM) sealed cavity that maintains high quality without requiring complicated metal bonding; and b) a new electrostatic bi-directional MEMS tuner that implements the needed frequency tuning without lowering the resonator quality factor. Furthermore, we explore important design and fabrication trade-offs regarding sensitivity to non-ideal effects (residual stress, fabrication imperfections). Measurement of the new prototype bi-directional design, prove that this technology readily corrects residual post-bias displacement of 0.1 μm that shifts the frequency by over 1 GHz with less than 2.5 V. It takes over 100 seconds to recover this error in the uni-directional case. This correction does not adversely affect the filter performance.

1. INTRODUCTION

1.1 Background

Over the past decade, the booming of mobile Internet has been driven the evolution of wireless communication technologies to meet the demands of user experience limited by signal coverage and data-rate. Looking forward this trend is advancing towards Internet-of-everything which connects vast number of wireless terminals with additional demands on bandwidth, latency, and power consumption. As a result, there are significant RF front-end design challenges which require innovations on both the system and device levels. From the system perspective, a typical multi-band front-end, shown in Fig. 1.1(a), switches between multiple static component banks. As the number of supported bands is increasing, system complexity also increases. The idea of cognitive radio (CR) proposes to address such challenges by employing reconfigurable RF front-end. For instance, as reported in [1] and shown in Fig. 1.1(b), replacing banks of static duplex filters and antennas with tunable ones, provides a duplexer function over the air and significantly reduces the system size and power consumption.

Nevertheless, due to scarcity of unlicensed electromagnetic spectrum in lower frequencies, the allocated frequency bands for the incoming—the fifth generation (5G)—wireless communication standards, spread broadly from sub 6 GHz to K and potentially W bands. As such, on the device level, realization of CR concept demands large—more than an octave-tunability. This is a significant technology challenge, especially for RF front-end components that need to maintain their RF performances which directly correlate to system specifications.

1.2 Overview of Tunable Filter Technologies

Reconfigurable filter remains the bottleneck of front-end design. Its main performance specifications are insertion loss, tuning range, power consumption, tuning speed, form fac-

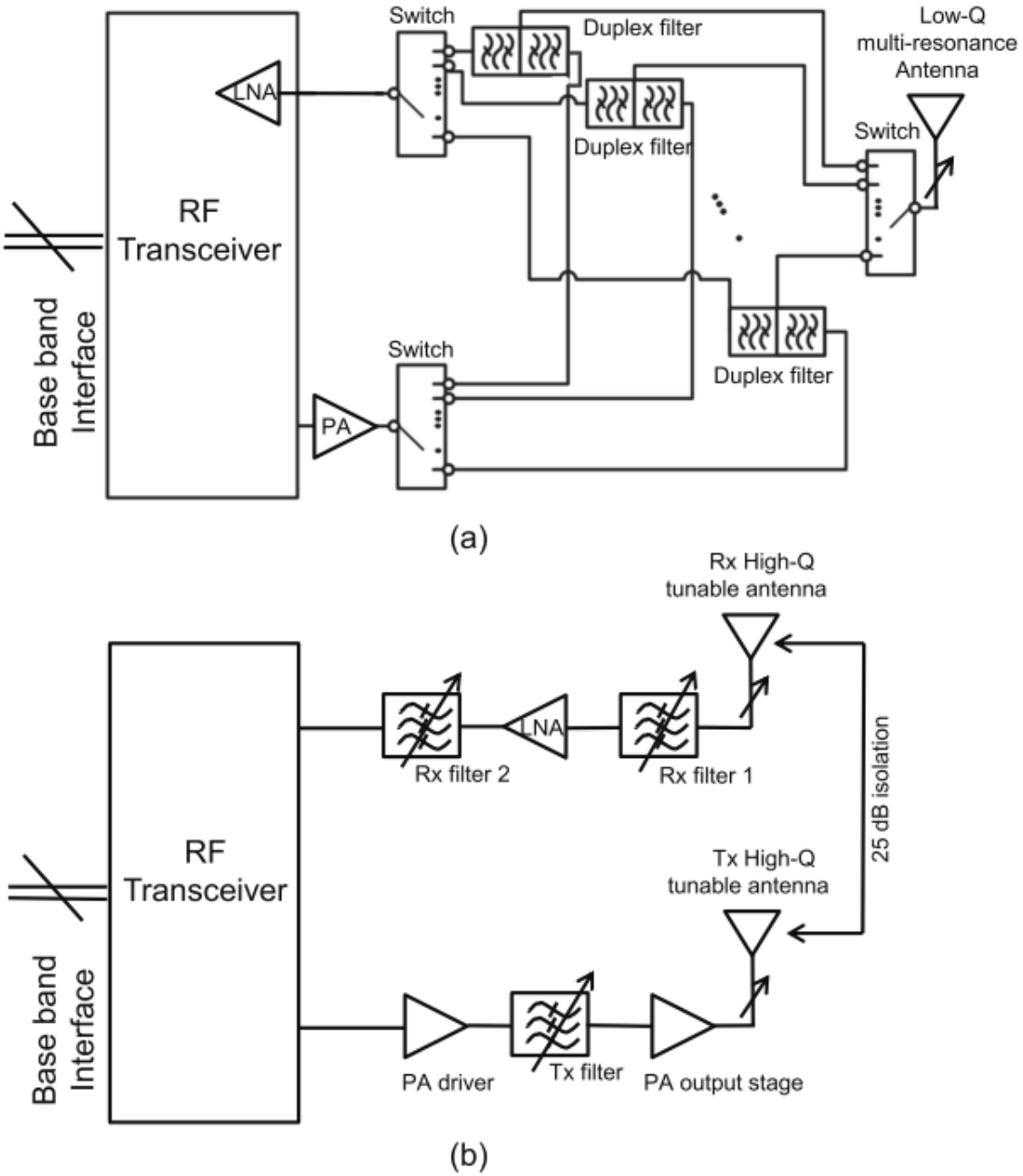

Fig. 1.1. (a) Traditional RF front-end, (b) Reconfigurable RF front-end [1].

tor, linearity, impedance matching, etc,. The filter architecture and tuning technology are two factors dominating the performance matrix. A number of technologies are available for reconfigurable filter design. Despite many having solutions that performs well in one or two dimensions, it is very challenging to identify one that performs well in most of them. Design requirements often result in no obvious solution. For instance, this is particularly true when low loss, wide tunability, and low power consumption need to be simultaneously satisfied.

The considered RF tunable filter architectures include discrete lumped-element (LE)-based resonators [2, 3], planar transmission line (TL)-based geometries [4–6] and three-dimensional (3D) waveguide cavities [7]. Whereas LE-based filters can be monolithically integrated on the RF receiver chip, their low quality factors (Q_u less than 30) render them unsuitable for high-frequency applications particularly above 10 GHz. On the other hand, planar TL-based filters exhibit moderate quality factor Q_u (less than 100-200) and can be readily co-integrated with surface-mount tuning elements. They are suitable for low-to-mid frequency applications but still result in unacceptable high losses in high frequencies. Non-planar (3D) filters outperform the aforementioned technologies with Q_u in the order of 1,000-10,000 depending on the employed technology. Nevertheless, they typically come at the expense of form factor.

Filter's tunability is typically achieved by co-integrating reactive elements such as semiconductor varactors [5, 11], MEMS devices [4] and ferroelectric capacitors [12] within the filter volume. Although semiconductor-based varactors feature compact size and high tuning range, they suffer from low Q_u for frequencies higher than 10 GHz. On the other hand, ferromagnetic varactors exhibit a good compromise among tuning range, speed, and power consumption. However, the requirement for specific substrate materials limits their integration potential. Although they are still at a research stage, MEMS-based tuners have demonstrated excellent RF loss, and are scalable to higher frequencies. [13–22].

Several recent research efforts have successfully demonstrated co-integration of MEMS tuners and 3D waveguides for frequency-agile low-loss transfer functions. However, the actualization of a widely-tunable response remains a significant challenge. In [10, 23],

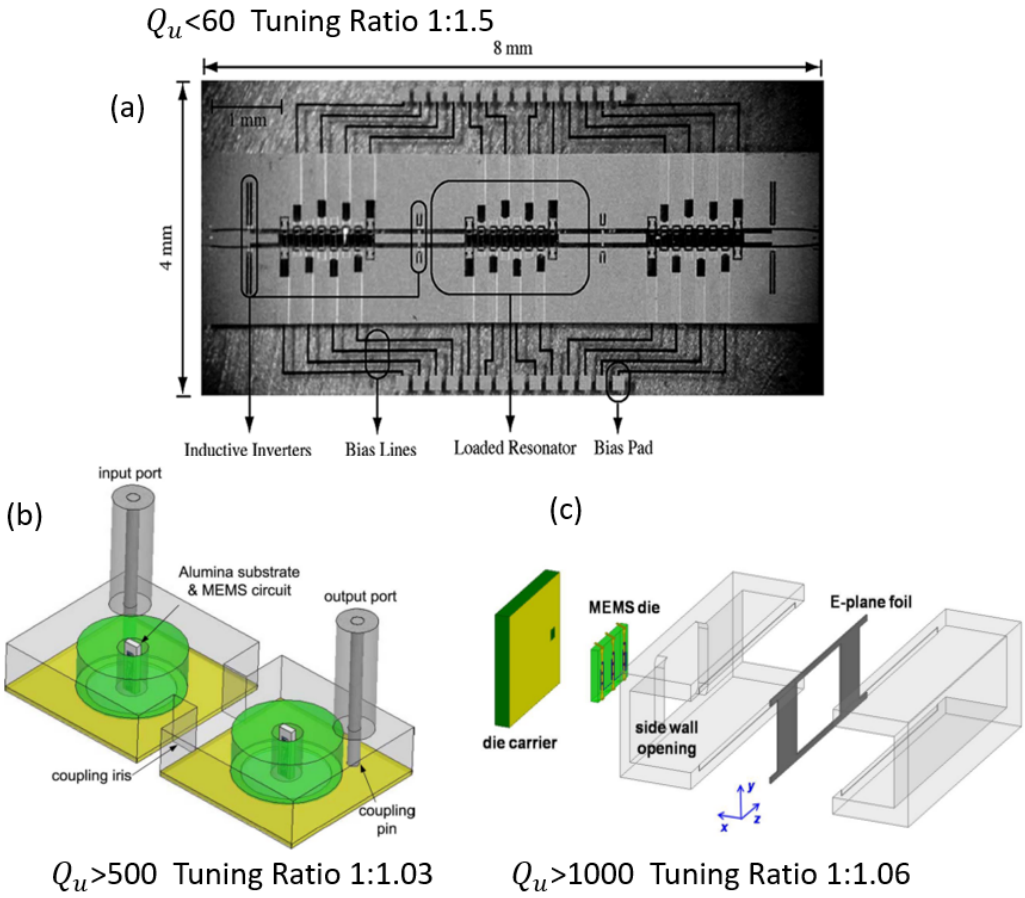

Fig. 1.2. (a) MEMS varactor tuned CPW filter [8], (b) MEMS varactor tuned dielectric resonator filter [9], (c) MEMS switchable waveguide filter [10].

the authors report on a tunable waveguide BPF whose center frequency is reconfigured by integrating ohmic cantilever RF-MEMS switches in the waveguide sidewalls. Whereas high Q_u (larger than 750) is obtained over the entire tuning range, its center frequency is tuned by only 10%. In yet another approach, dielectric-loaded waveguide BPFs are tuned by means of MEMS actuators. They exhibit Q_u larger than 500 and center frequency tuning of less than 3%, [9, 19].

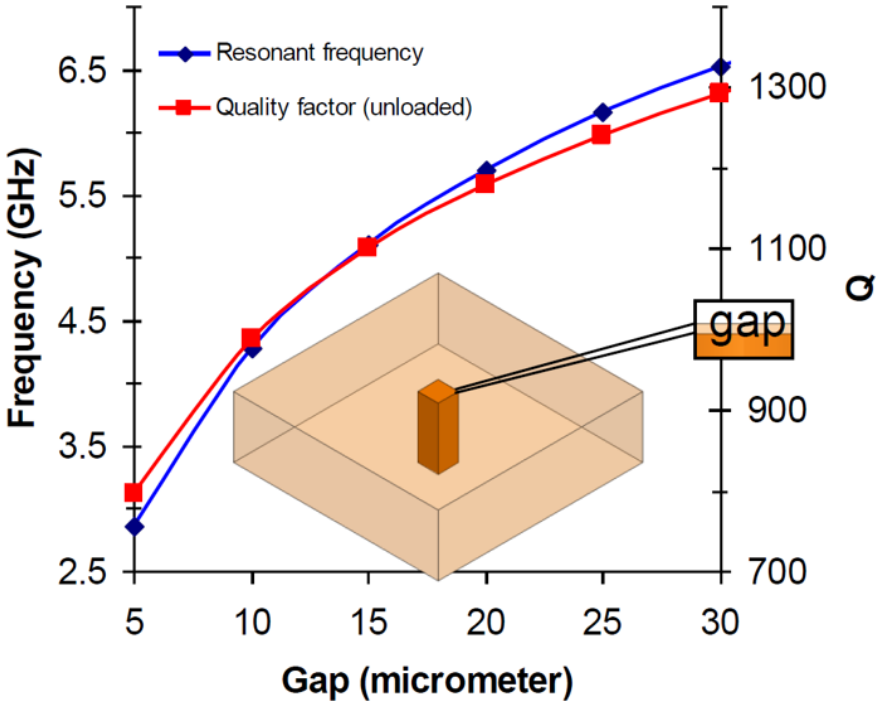

Fig. 1.3. Conceptual view of a EVA tunable cavity resonator.

1.3 Evanescent-Mode Cavity Tunable Filter Technologies

The evanescent-mode (EVA) cavity tunable filter technologies is one of the most promising candidate that possesses advantages in many of the important design specifications, especially for tuning range, form factor, and quality factor. Fig. 1.3 shows its conceptual drawing. Compared to conventional cavity resonator, there is a metallic post in the center

of the cavity. The top surface of the post is nearly touching the cavity ceiling and leaves a small capacitive gap. Such post capacitance significantly lowers the resonance frequency. As such, its cavity volume shrinks typically 10 to 30 $\times$ than the unloaded cavity resonators. Since most of electrical energy is stored within the capacitive gap, minor gap change induces effective frequency tuning. While the fundamental resonance is loaded, its spurious free range becomes much wider—possible to be greater than 35:1, while typical unloaded cavity resonator is 2:1.

Several recent research efforts reported in [24–31] have successfully demonstrated tunable EVA cavity filter concept with variety of tuner selections. [24, 25] laminates piezoelectric tuner disks together with a thin copper sheet on top of the SIW cavity substrate. Such type of tuning technology provides large deflections with moderate-to-high actuation voltage (0 to ±220 V). However, piezoelectric material suffers from low tuning speed (msec) and hysteresis. Besides, the viability of miniaturizing such piezoelectric disks and integrating them on other substrates has not been demonstrated yet.

[32] reports a EVA tunable resonator employing magneto-static diaphragm tuner. Despite its great tunability, high quality factor, magneto-static tuning demands significant amount of current which is a concern for low power applications. Another novel design, [33], utilizing deformation of a electro-static biased liquid metal drop has similar pros and cons as designers employing cantilever beam tuners reported in [26–28]. Both types of tuner feature with faster response (10s of μsec), lower actuation voltage (10s of V) and higher immunity to vibrations. However, their tuning range is severely limited by the small MEMS deflection.

The electro-static tuned SOI diaphragm design reported in [34] is the most prominent approach who demonstrated ultra-high tuning ratio (4:1) and high-quality factors (300-1000). Driving the post-cavity-ceiling gaps into the sub-micron region achieve such high tuning ratios. This came at the cost of relatively large diaphragms (>5 mm diameter) that required high actuation voltages (600 V) for full range analog tuning. The SOI nature of the tuner also made it hard to independently control the frequency of each pole of the filter since the bias electrode was common for all diaphragms-tuners of the filter. The high

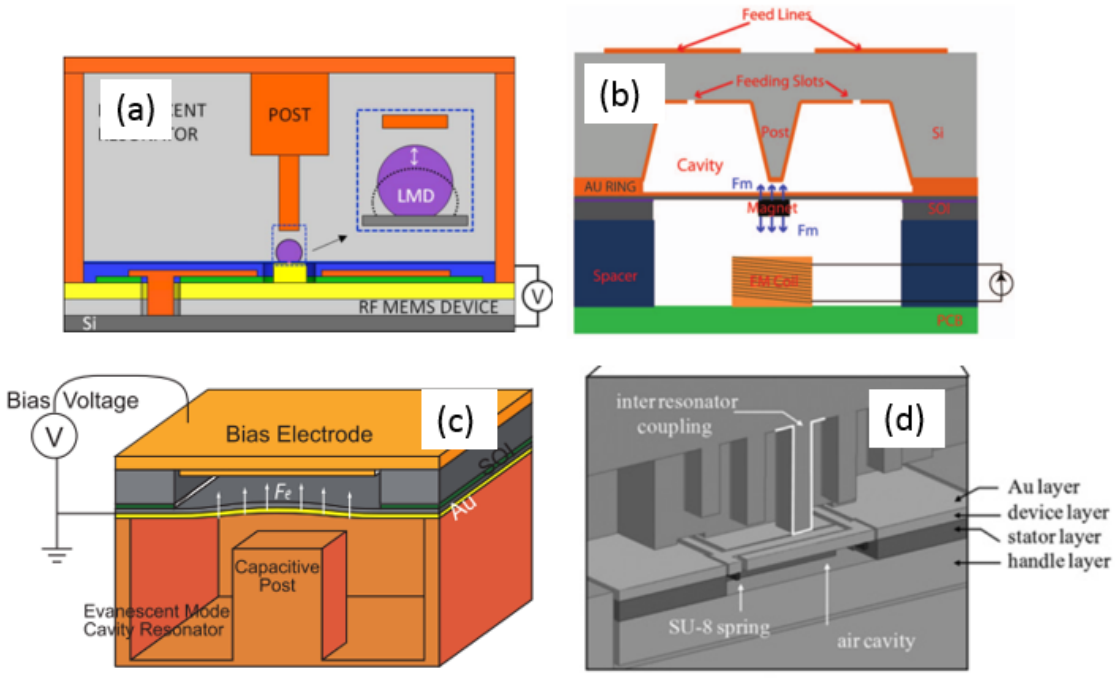

Fig. 1.4. (a) Electro-static actuated liquid metal ball, (b) Magneto-static actuated diaphragm, (c) Electro-static actuated diaphragm, (d) Electro-static actuated beam.

actuation voltage severely limited its application. The tuning voltage will foreseeable grow along with shrinking resonator size for higher operation frequency bands. Such scalability issue essentially becomes the bottleneck.

1.4 Dissertation Overview

The primary objective of this dissertation is 1) to explore novel RF-MEMS designs to advance the tunable EVA cavity filter into the mm-wave region, and 2) to explore advanced MEMS technologies to achieve superior tuning stability. Achieving the above objectives requires innovations in three areas: micro-fabrication technology, microwave cavity filter design and MEMS tuner design.

In Chapter 2, a connectorized RF MEMS tunable two-pole band-pass filter is demonstrated as the first all-silicon evanescent mode cavity filter operating in the K-Ka band. All filter components are fabricated with cost-effective silicon micromachining techniques. The filters poles are controlled by two micro-corrugated MEMS diaphragms that are engineered to be independently controlled with voltages below 140 V. Advanced fabrication techniques are applied for the first time to ensure independent pole-frequency control with no additional filter loss and improved fabrication accuracy and stability. The filters measured tuning range is from 23 GHz to 35 GHz (0-140 V) with fractional bandwidth ranging from 0.8% to 4%. The filters measured loss varies from 4.2 to 1.5 dB including its connectors. The extracted filter quality factor varies from 530 to 750. The maximum actuation voltage of 140 V is 2× lower than previous demonstrations for similar tuning ranges. The filters stability has been tested up to 1 billion cycles (0-70 V cycling) with no failures observed. The filter exhibits a burn-in period of about 40 million cycles.

In Chapter 3, an RF design methodology that takes into consideration all microfabrication-induced constraints determined in Chapter 2—e.g., non-vertical wall profiles and finite MEMS deflection—enables high unloaded factor (Q_u) and also minimizes bandwidth (BW) variation within the octave tuning range is reported. Furthermore, a new passively compensating package-integrated input/output feeding structure that enables optimal impedance matching over the entire tuning range is also presented. To evaluate the RF design methodology, a filter prototype was manufactured and measured at Ka-band. It exhibits a measured frequency tuning between 20 to 40 GHz (2:1 tuning range), relative bandwidth between 1.9 to 4.7%, insertion loss between 3.1 to 1.1 dB and input reflection below 15 dB. This work also explores essential trade-offs between mechanical stability and insertion loss by comparing creep-resistant to pure-Au tuning diagrams.

The MEMS-enabled all-silicon EVA cavity tunable filter has demonstrated its outstanding RF performance of over an-octave tunability and high Q_u in Chapter 3. Nevertheless tuning stability remains a challenge for large actuation of the diaphragm made with the viscoelastic metal such as gold in this application. Feedback-loop controlled voltage compensation is a viable solution. However, due to the nature of electrostatic tuning, the restora-

tion error at the unbiased state is not compensable with the existing uni-directional tuner. Chapter 4 proposes a bi-directional electro-statical MEMS tuner which enables active voltage compensation over the full tuning range. Such design does not introduce significant complexity of fabrication nor structural integration. Furthermore, a proposed RF modeling and optimization method addressed RF performance degradation concerns. A detailed RF-MEMS co-design, optimization flow of the implemented MEMS micro-corrugated diaphragm to maximizing the MEMS tunability are discussed. As an example, a proof-of-the-concept, two-pole filter is fabricated and demonstrates a measured bi-directional tuning range from 18.9 to 39.6 GHz, in which the forward (main) actuation tunes from 21.3 to 39.6 GHz with 120 V and the reverse (corrective) actuation tunes from 21.3 down to 18.9 GHz with 2 V. The measured filter insertion loss varies from 3.14 to 0.78 dB and its instantaneous bandwidth from 0.31 to 1.81 GHz. The extracted unloaded quality factor is 265-510 which is comparable to the state-of-the-art filter of this type employing conventional uni-directional tuners.

1.5 Related Publications

- **Z. Yang**, and D. Peroulis,"A 23-35 GHz MEMS tunable all-silicon cavity filter with-stability characterization up to 140 million cycles, in *IEEE MTT-S Int. Microw. Symp.Dig.*, Tampa, USA, 2014, pp. 1-3.

- **Z. Yang**, D. Psychogiou, and D. Peroulis, "Design and optimization of tunable silicon-integrated evanescent-mode bandpass filters" *IEEE Tran. Microw. Theory Tech.*, vol. 66, no. 4, pp. 1790-1803, Jan. 2018.

2. SI-BASED EVA CAVITY TUNABLE FILTER PROTOTYPE

2.1 General Structure

Fig. 2.1 depicts geometrical details of the proposing MEMS tunable EVA cavity filter for an example case of a two-resonator transfer function. The cavity top ceiling is a silicon substrate sputter-coated with a layer of Au film. Two flexible diaphragms, as part of the Au film, control the resonant frequency of each resonator. A pair of electrodes—Au-coated silicon-etched posts—are placed above the tuning diaphragms through appropriately etched via holes on the back side of the diaphragms. A layer of silicon dioxide electrically isolates electrodes from the silicon substrate. This allows us to independently control each diaphragm. As an additional design detail to be noted, the height of the bias electrode determines the initial electro-static bias gap, which accordingly defines the maximum applied actuation voltage for a given diaphragm deflection. A metallic package houses the filter assembly to facilitate the RF excitation through coaxial-type connectors locating at the bottom side of the package. Those feeding pins are inserted into the filter cavities through the etched via holes and coupled to the cavity resonator by means of magnetic coupling. It should be noted that the feeding pins always maintain DC contact with the cavity upper ceiling for optimal mechanical stability, lower fabrication uncertainty and stronger magnetic field coupling.

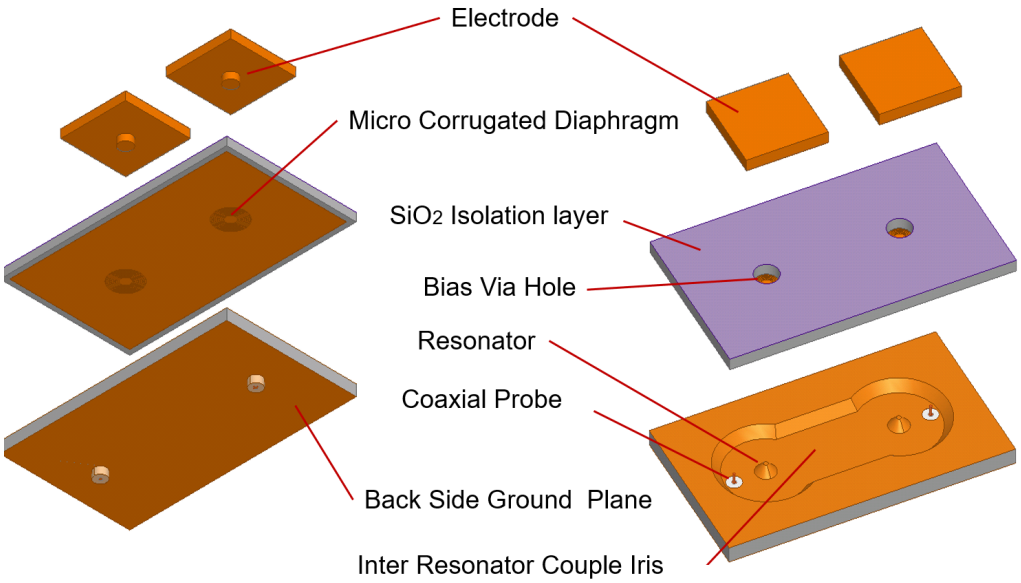

Fig. 2.1. 3-D explosive view of the proposing EVA tunable filter structure.

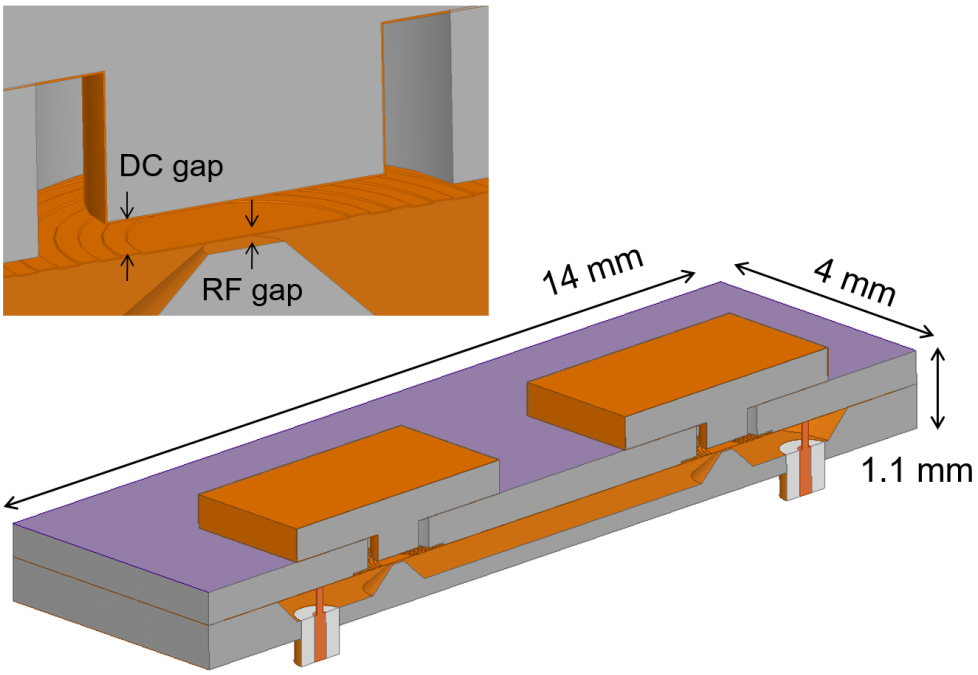

Fig. 2.2. 3-D assembly view of the filter structure.

2.2 Basic MEMS and RF Design

2.2.1 MEMS Tuner Design

Initially EVA cavity filter tuner employs the flat Au-coated SOI diaphragm.The bending behavior of a flat diaphragm can be described by the equations below:

$$P_{flat} = \frac{4t_d}{R_d^2}\left(\sigma_0 + 1.33\frac{E_d t_d^2}{4R_d^2}\right)\Delta g + 2.83\left(\frac{E_d t_d}{R_d^4}\right)\Delta g^3 \tag{2.1}$$

in which P_{flat} is the pressure imposing on the flat diaphragm and Δg is the out-of-the-plane deflection. The E_d, ν, t_d, R_d are Young's modulus, Poisson ratio, diaphragm thickness and diaphragm radius respectively. σ_0 is the diaphragm residual stress. Scaling such a design into a smaller resonator cavity operating on higher frequency demands further reduction of R_d. It results in large P_{flat} and so as high actuation voltage. Pure Au flat diaphragm is a solution, which reduces the t_d and E_d. However, the scaling bottleneck still exists since R_d remains the highest power among all parameters, and particularly true for the third order tension term, which governs the large deflection behavior. Furthermore, without silicon, pure Au diaphragm is susceptible to stress induced reliability issues such as creep and stress relaxation.

Fig. 2.3 shows a conceptual drawing of the proposing MEMS tuner design employing Micro-corrugated diaphragms (MCD). The MCD exhibits significantly lower tensile rigidity in the radial direction [35]. Instead of stretching the material, bending of MCD elongates its corrugation sections and effectively reduces the radial tensile stress. As a result, MCD demands lower bias voltage and suffers less material stretch for the same amount of deflection. The bending behavior of a MCD can be modeled as the superposition of a stress-free corrugated diaphragm and a flat diaphragm with initial stress [35]:

$$P_{MCD} = (A_p\frac{E_d t_d^3}{R_d^4} + \sigma_0\frac{4B_p(1-\mu^2)t_d}{2.83R_d^2})\Delta g + B_p\frac{E_d t_d}{R_d^4}\Delta g^3 \tag{2.2}$$

In the above equation, P_{MCD} represents homogeneous pressure on the diaphragm. The small deflection stiffness coefficient A_p and large deflection stiffness coefficient B_p are both related to the corrugation profile factor, which is dominated by the ratio of t_d to corrugation

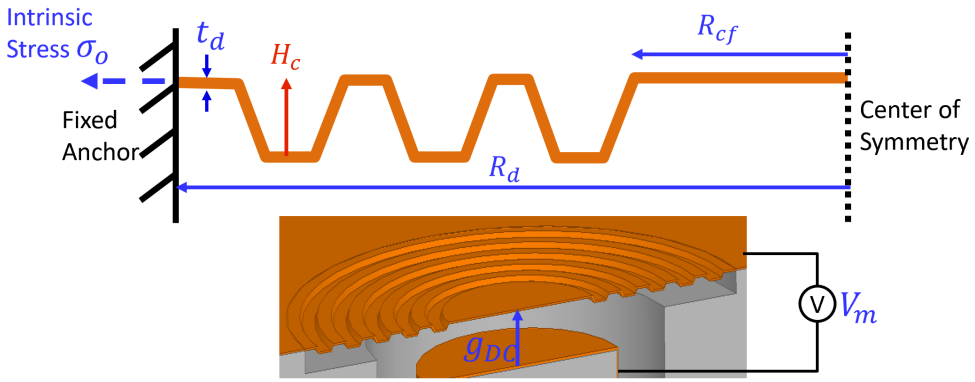

Fig. 2.3. Conceptual drawing of the MCD.

depth H_c. The electro-static pressure induced by two parallel DC biased electrode is given by Eqn. (2.3) (assuming the dimensions of the electrodes are much larger than the DC gap)

$$P_{MCD} = -\frac{\frac{1}{2}\varepsilon_0 V^2}{g_{DC0} - \Delta g} \tag{2.3}$$

where V, ε_0, g_{DC0}, are the bias voltage, vacuum permittivity, an initial gap between the electrode and diaphragm. Equating Eqn. (2.2) and Eqn. (2.3), yields the relationship between bias voltage and diaphragm deflection $V(\Delta g)$. Solving the equation $d(V)/d(\Delta g) = 0$ yields the pull-down voltage and continuous tuning range. The goal of this work is to design a diaphragm with a bias voltage of less than 200 V and having the largest possible continues deflection range. The mathematical equations have been translated into MATLAB code. The final designed dimensions and properties of the MEMS diaphragm are listed as follows: diameter = 1.8 mm, thickness = 1 μm, corrugation height = 3.5 μm, initial DC gap = 45 μm, continues theoretical deflection range = 22.6 μm.

2.2.2 Filter Cavity Design

The filter consists of two circular evanescent mode resonators. The eigenmode simulated Q_u of the resonator is 560-810 assuming the cavity wall is perfectly smooth and perfect connection between the cavity wall and ceiling exists. Two resonators are coupled

through a coupling iris in the center. For a 2:1 frequency tuning ratio, the normalized coupling coefficient has a maximum 8:1 variation ratio. By optimizing the aspect ratio of the coupling iris, coupling variation can be reduced to 2:1. However, the optimized iris design requires too small of inter-resonator distance that cannot fit two side-by-side 2.4-mm connectors. Therefore, an un-optimized design was implemented due to this restriction. The HFSS simulated filter performance is shown in Fig. 2.4.

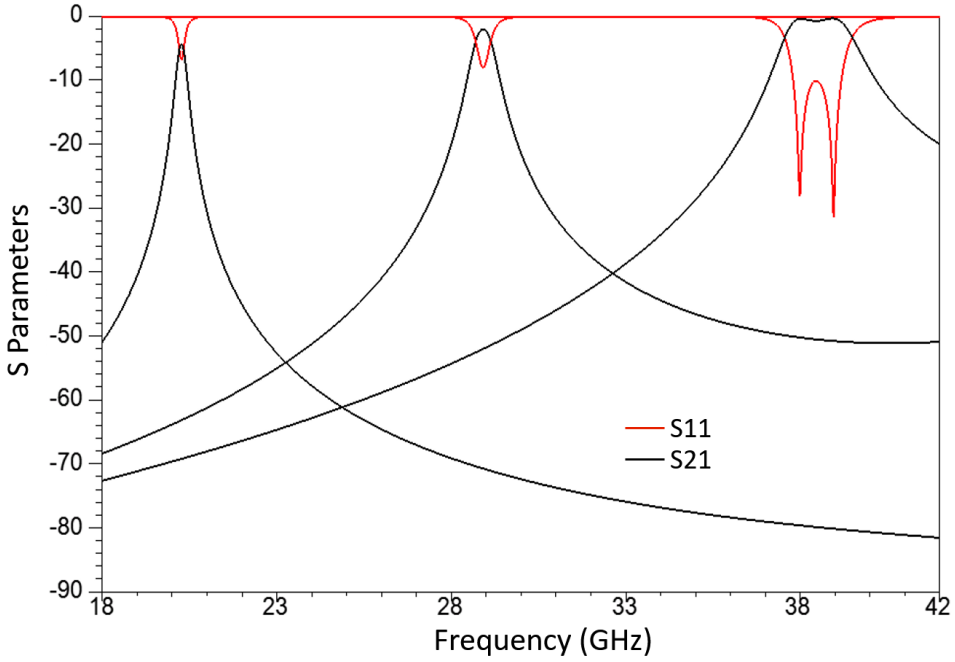

Fig. 2.4. HFSS simulated tunable filter RF performance.

2.3 Micro-fabrication Flow

2.3.1 MEMS Tuner Fabrication Flow

Starting on a 4-inch, 300-μm thick, double side polished silicon (Si) wafer whose crystal orientation is <1 0 0>, the first step defines the sacrificial layer for the membrane. Photo-lithography followed by a buffered-oxide-etch (BOE) process makes the top surface silicon dioxide layer a hard mask of the corrugation pattern. Silicon wet-etching the wafer

in a tetramethylammonium hydroxide (TMAH) bath forms trapezoid corrugation profiles. Based on the study described in [36,37], maintaining the etch bath at 90 °C without stirring while adding Triton X-100 (10 ppm Triton:TMAH volume ratio) surfactant best retains the corrugation geometry and surface smoothness.

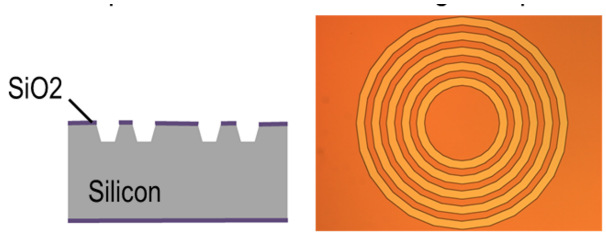

Fig. 2.5. MCD fabrication step 1: Silicon wet-etch patterns corrugations.

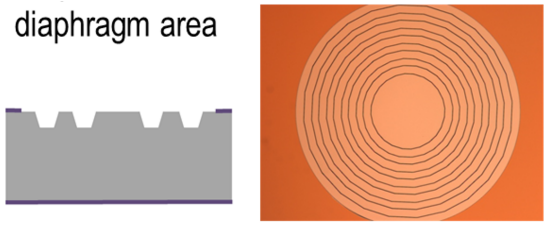

Fig. 2.6. MCD fabrication step 2: Oxide-etch removes oxide under MCD area.

The second step defines the deep trenches for bias electrodes and RF probe feeds. Spin coating then hard baking deposits a layer of thick photo-resist (PR) (15 μm AZ 9260) on the back side of wafer. Lithography and BOE expose silicon on the trench area. Without removing the PR mask, plasma deep-reactive-ion-etching (DRIE) creates deep trenches and stops at a depth of 275 μm while reserving a 25 μm thick layer of silicon as the sacrificial layer of the diaphragm. The DRIE process consumes around 10 μm of PR, which protects the underlying silicon dioxide layer. Such an oxide layer is critical for preventing DC biasing current leakage. Afterwards, the remaining photo-resist is removed in a 80 °C Baker PRS-2000 bath.

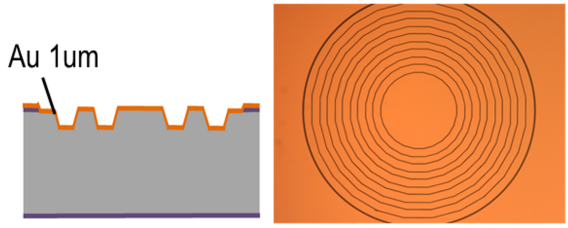

Fig. 2.7. MCD fabrication step 3: Au sputtering.

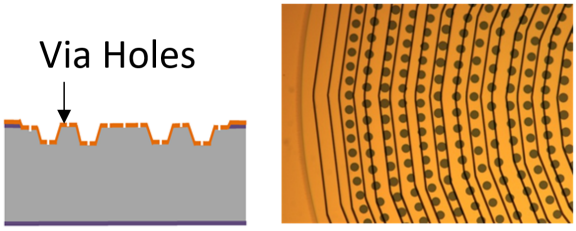

Fig. 2.8. MCD fabrication step 4: Au-etch patterns releasing holes.

In the third step, lithography and BOE removes remaining silicon dioxide hard masks within the diaphragm area. Co-sputtering Au and V deposits a 1 μm Au film on a seed layer of Ti in an argon plasma chamber.

Making the intrinsic stress of the corrugated diaphragm tensile and minimal is critical to maintaining its flatness after releasing. Otherwise, a stressed corrugated diaphragm displays large initial bending and its mechanical behavior does not follow the analysis in Section 4.2.2. To this end, in-house experiments conducted based on [38] show fine tuning chamber pressure to 7.6 mTorr results in the lowest deposited tensile stress 0–45 MPa.

Spin coating PR on the sputtered film builds a lithography mask for Au etching. This thick resist must cover the corrugation edges well. The etching removes large area of gold on the die boundary as well as small releasing holes in the diaphragm area. Prior to the etching, performing an argon plasma surface treatment makes the surface of photo-resist hydrophilic to ensure etchant accessibility to the exposed Au surface. A short bath in the Ti etchant afterwards removes the remaining Ti seed layer.

The forth step deposits a 1-μm thick layer of silicon dioxide using plasma-enhanced chemical vaporized deposition (PECVD) with a seed layer of silicon nitride. Photo-lithography and BOE removes most of the oxide thin film on the Au surface but preserves a small margin near the cavity edge for the MOM sealing. Finally, Xenon-difluoride dry etching removes the silicon sacrificial layer and releases the diaphragm. This step is typically performed after cavity bonding for better yield.

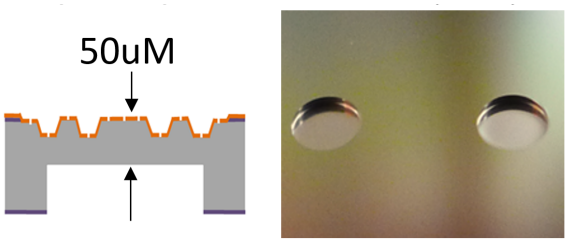

Fig. 2.9. MCD fabrication step 5: Deep-reactive-ion-etching digs back side via holes.

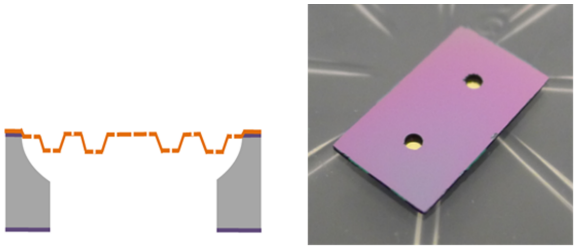

Fig. 2.10. MCD fabrication step 6: Xenon difluoride silicon etching release the diaprhgm.

2.3.2 Filter Cavity and Electrode Fabrication Flow

Starting on a 675-μm thick 4-inch double side polished silicon wafer with crystal orientation <1 0 0> , the same TMAH etching techniques create a 400-μm deep cavity. PECVD deposits a 100 nm silicon nitride layer within the cavity to protect its surface finishing. DRIE etches RF feed via holes through the back of the wafer while the pre-deposited silicon nitride layer automatically stops the etching when the via holes are etched through. After BOE removes all dioxide, repeating sputtering deposits a 1.5 μm Au film on the top

and bottom side of the cavity. Controlling sputtering pressure for the gold film intrinsic stress minimizes the resulted sheet resistance.

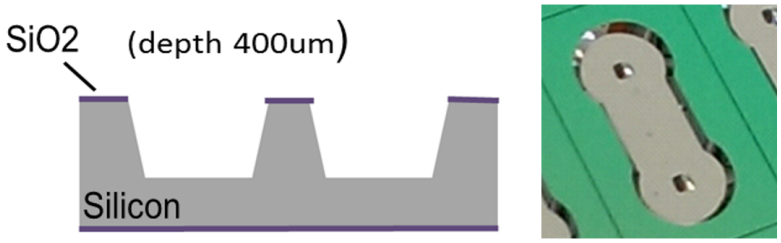

Fig. 2.11. Cavity fabrication step 1: TMAH silicon etch.

Fig. 2.12. Cavity fabrication step 2: Deep-Reactive-Ion-Etching.

Fig. 2.13. Cavity fabrication step 3: Au deposition.

The electrode was fabricated on a 1-mm thick 4-inch double side polished silicon wafer. Firstly, Au sputtering deposits 0.2 μm of Au on the backside of the wafer. Then DRIE on the front side of the wafer creates posts. Finally, Au sputtering then coats the electrode post and side walls. Finally, the sample is diced and cleaned.

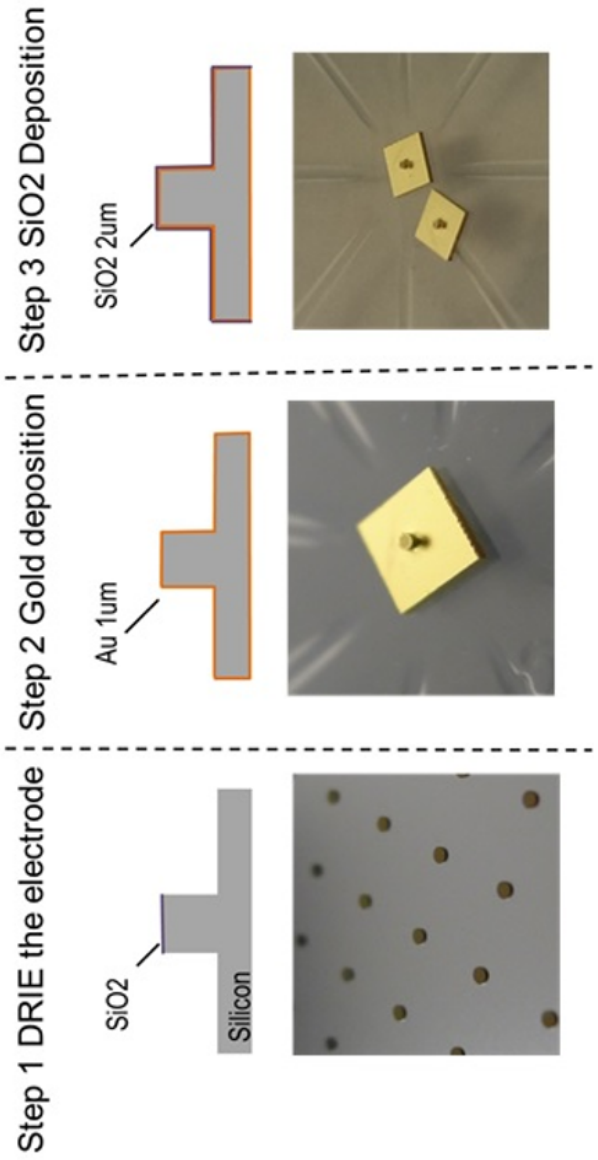

Fig. 2.14. Top electrode fabrication process.

2.4 Die Assembly and Packaging

2.4.1 Substrate Bonding

Conventional bonding process commonly use eutectic gold–tin soldering. However, the solder reflow effect makes the solder layer thickness hard to control so as the RF post gap. As a solderless alternative, conventional thermal compression bonding requires excessive high temperature—larger than 300 °C. Such high temperature plus pressure can severe damages the released diaphragm and lead to meager yield.

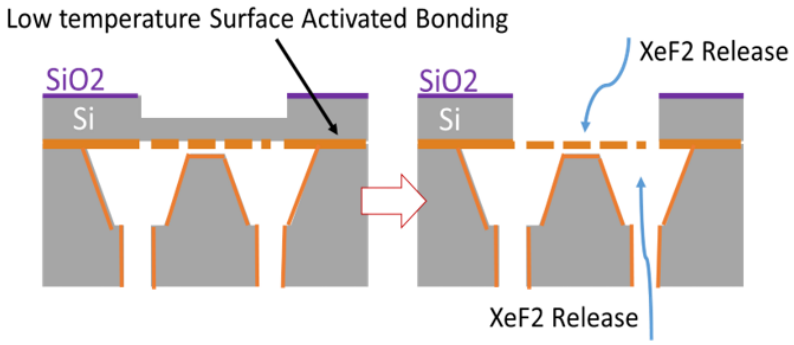

Fig. 2.15. Demonstration of diaphragm release and bonding procedures.

As a mitigation, it is preferable to perform bonding prior to the diaphragm release as such the 45 μm silicon sacrificial layer protects the diaphragm from buckling. Fig. 2.15 depicts the proposed bonding scheme. The unreleased die is bonded with the cavity die prior the XeF2 silicon etch. Since the Au film thoroughly covers the cavity die, there is no impact on the cavity die if exposed in the XeF2 etching. External feeding via holes on the bottom of the cavity essentially becomes the gas venting channel for both of the chamber vacuuming stage and etching stage. Nevertheless, for such bonding flow, the diaphragm surface is within the cavity thus the etching progress no along be able to be checked by an optical microscope. Instead, using infrared microscope addresses such issue, referencing the Fig. 2.16, We can measure and control the etched MCD boundary precisely to the designated value.

On the other hand, reducing the bonding temperature is necessary to prevent diaphragm builds up non-ideal residual stress. For such reason, this work employs a technique so-called surface active bonding reported in [39]. Prior to the bonding, both of the un-released diaphragm substrate and cavity substrate are cleaned with RCA II processes to remove the particles and organic substances on their surfaces. Afterward, We follow the recipes recommended in [39], preparing the clean, active surfaces by irradiation of argon RF plasma (oscillation frequency: 13.56 MHz; RF power: 100 W; plasma pressure: 7.6 Pa). Such process slightly roughen the Au surface with a rate of 30 nm/min. After surface activation, we aligned and bonded the samples using a heated flip-chip bonder of temperature 150 ° C.

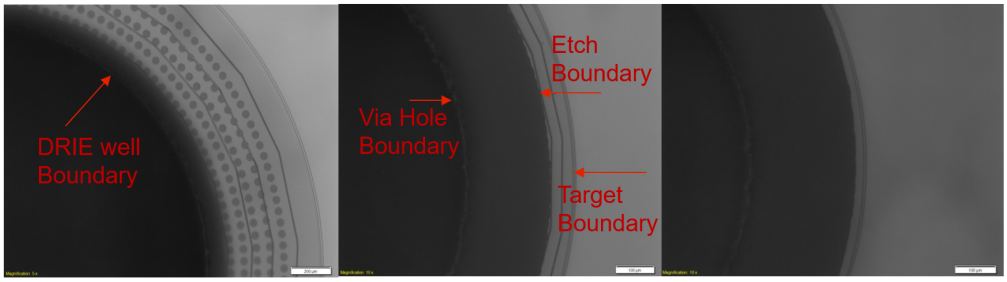

Fig. 2.16. Infrared microscope images of diaphragm release by xenon difluoride.

2.4.2 Filter Package Assembly Flow

Fig. 2.17 summarizes the prototype assembly process. There are two 2.4 mm coaxial ports screw fastened on the aluminum bulk. The center pins with its wrapped dielectric layer go through the aluminum bulk by via holes. While one end of the center pin is inserted into the coaxial port center pin receptor hole, the other end is making contact to the cavity ceiling. There is a friction between the receptor hole and the center probe to maintain the height of the center pin. The sample of the bonded filter silicon die then aligned and pressed into the package. The friction between the cavity port via holes and the center pin dielectric hold it in the aligned state. Afterward, the two tuning electrodes are aligned with each of their post centers to the center of the diaphragm then carefully placed

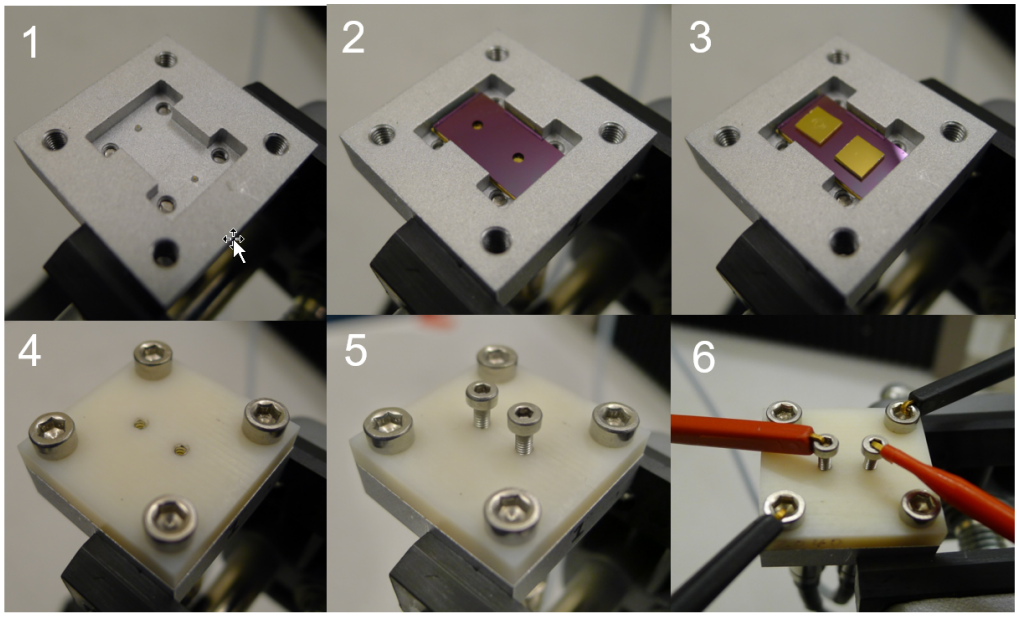

Fig. 2.17. Filter package assemble flow.

on top of the MEMS die. Afterwards, we mount a piece of plastic lid closing the package by fastening four threaded mounting screws in the corners. In this end, We use another two fine-threaded biasing screws screwing into the package and gently touching the electrodes.

2.5 Prototype Measurements

2.5.1 Filter S-parameter Measurements

After the prototype assembly, we measured filter RF functionalities using an Agilent E8361A network analyzer. Two Keithley 2400 power supplies independently bias each resonator and tune the filter from 23.4 GHz to 35.1 GHz. Fig. 2.19 summaries the measurement results. The full-range bias voltage is less than 140 V. By fitting to the HFSS simulation results, the extracted experimentally achieved RF gap is between 1.8 μm to 10 μm. Assuming a back-to-back connector loss is 0.3 dB, the extracted resonator quality factor is 530 to 750 over the tuning range. These results are very close to the ones predicted by HFSS eigenmode simulations of 560 to 810. The measured pass-band ripple level though is

higher than the simulated one. This is due to the external feeding pin not being perfectly in contact with the filter cavity ceiling and thus resulting in a slightly weaker external coupling coefficient.

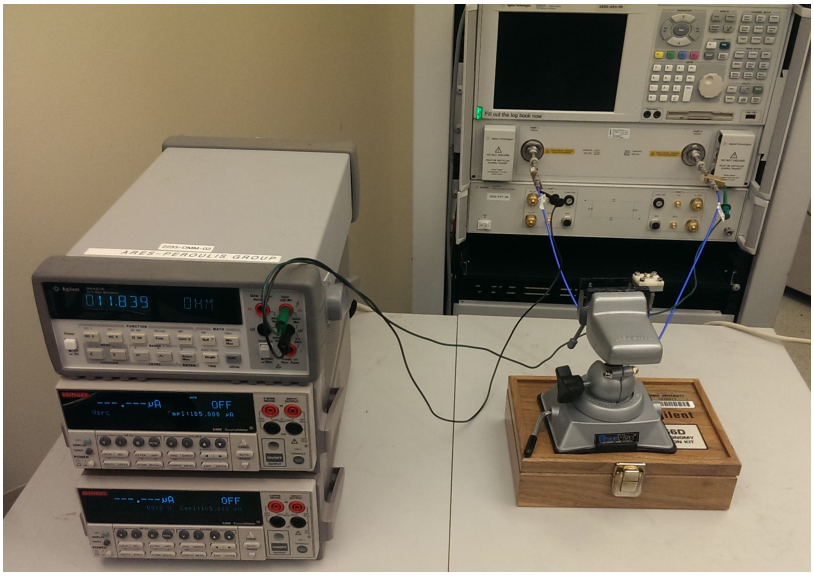

Fig. 2.18. Filter S-parameter measurement setup.

2.5.2 MEMS Tuning Stability Characterizations

In order to qualify the long-term tuning stability, We further tested the filter with a 500 Hz 0-70 V square wave bias signal cycling the MEMS tuners. There is are temporarily short stop for data collection during the cycling process. During the stop time, we record the 0V unbiased frequency and the voltage tunes the filter at 30 GHz. This process lasts until tuner completed 1 billion cycles and Fig. 2.20 plots the results versus number of cycles.

The plots are depicting the so-called ”bathtub” curve for characterizing the phase of the DUT lifetime. The filter finishes its break-in for the first 40 million cycles. Afterward, the device reaches its steady state, and high stability is achieved. During the steady state region, the stress relaxation effect is gradually making the diaphragm softer as such the

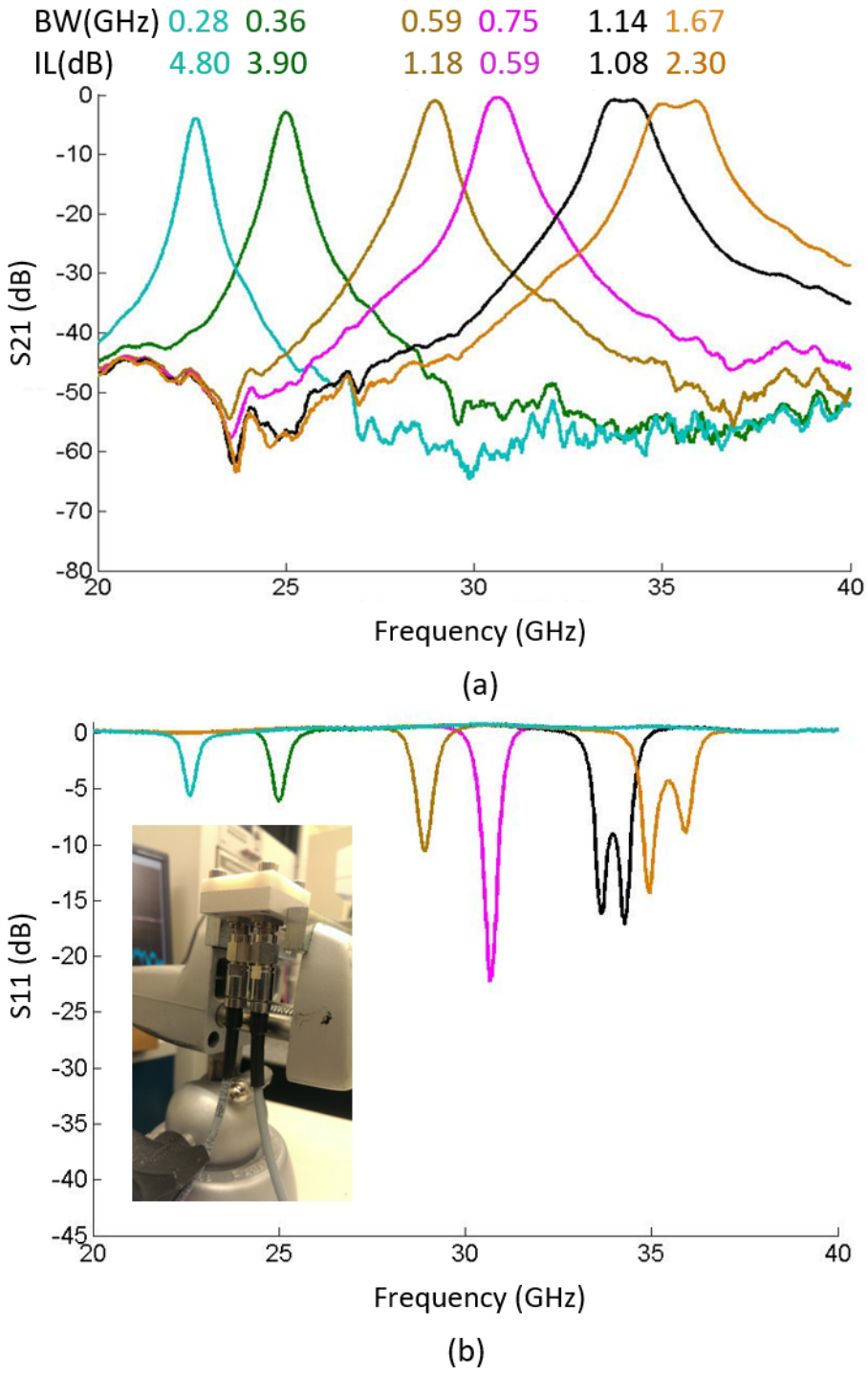

Fig. 2.19. (a) Measured filter transmission coefficient (b) Measured filter reflection coefficient.

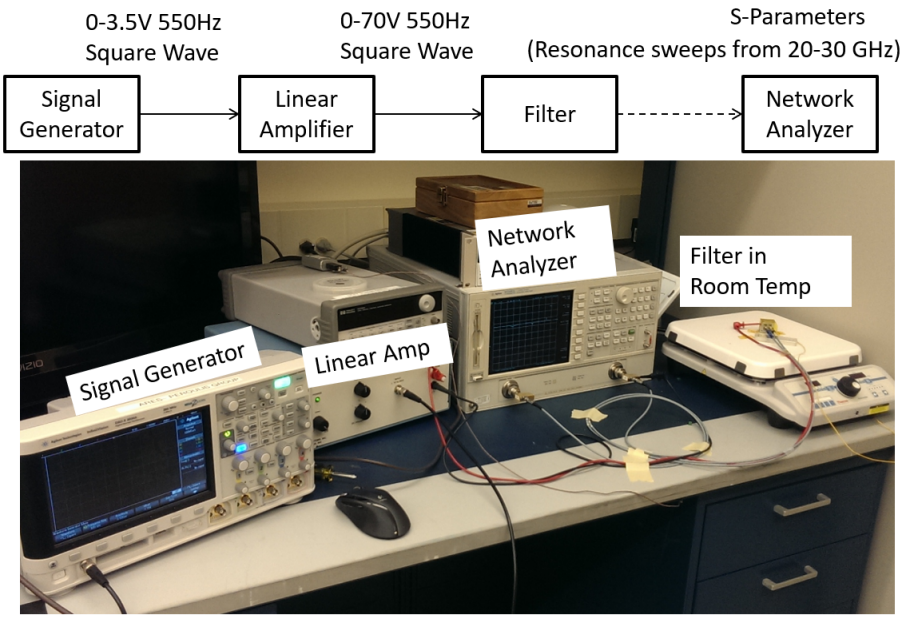

Fig. 2.20. Diaphragm in package cycling test setup.

bias voltage for 30 GHz is stepping down and the neutral position is creeping higher. When the number of cycles reached 600 million, the fatigue accelerates the diaphragm softening and plastically deformed so that the unbiased frequency no longer returning to 20 GHz. It worth to point out that, voltage compensation can correct the tuning error. Nevertheless, the unbiased frequency cannot be compensated, and eventually, lead to a significant reduction. This is the primary failure mode of this technology.

2.6 MEMS Tuning Stability Enhancements

To achieve an octave frequency tuning, the MEMS diaphragm needs to provide a displacement of at least 10 μm. This is a substantial displacement for a 1-to-2-μm thick diaphragm which makes it susceptive to creep/fatigue. This is particularly true when viscoelastic metals such as gold are employed [40]. Employing MCD design partially alleviates the bending stress and reduces creep. Further stability enhancement demands mitigating viscoelasticity of the metallic film.

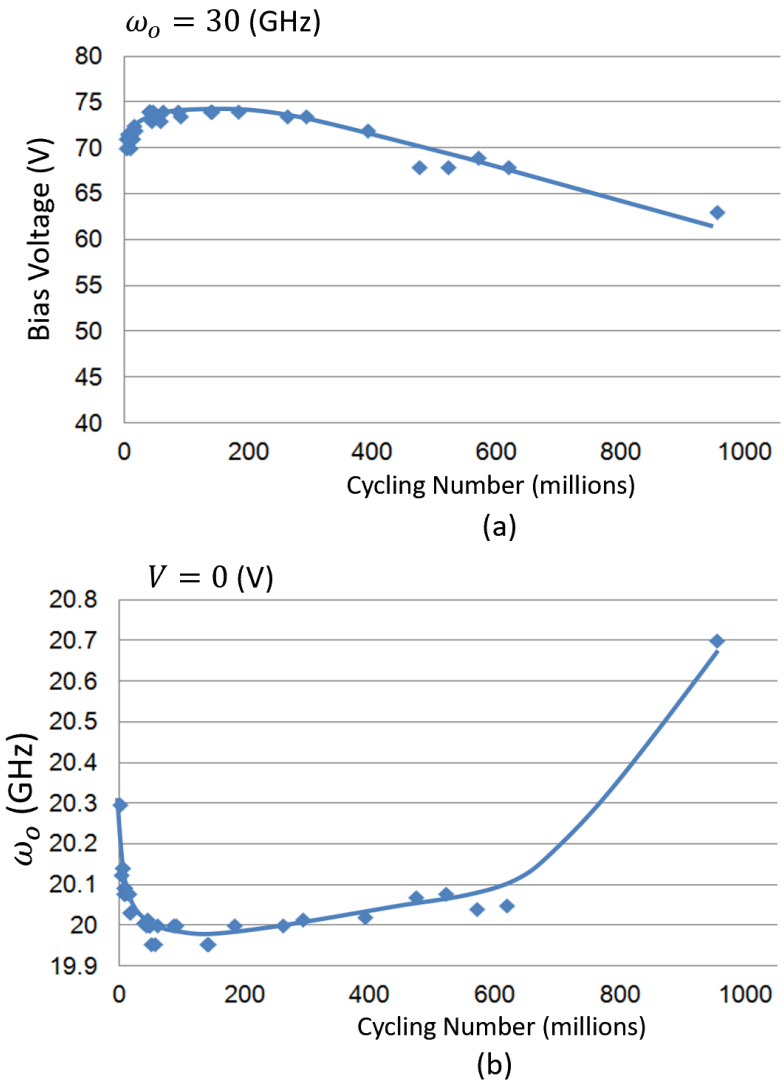

Fig. 2.21. (a) Mid-band (30 GHz) tuning voltage variation of operation cycles, (b) Low-band ($\tilde{2}0$ GHz) unbiased tuned frequency drift over operation cycles.

Creep-resistant thin films have been actively studied [41], [42] and it has been reported that transition elements such as vanadium exhibit promising characteristics. For example, Au-V films show significantly increased resistance to inelastic deformation at high temperatures [41], which is an attractive feature of this material for applications in RF MEMS tunable filters.

Incorporation of Au-V diaphragm requires no extra process but an extra vanadium source simultaneously excited during the Au sputtering process. Sputtering current ratio of V-to-Au is the knob controlling the vanadium concentration. In this work, we set V-to-Au current ratio as 20-to-100 mA. The result shows in the co-sputtered Au-V film V atomic percentage is 2.2 at. %. by characterizing its element composition using X-ray photo electron spectroscopy (XPS).

Fig. 2.22 shows the captured SEM images of the Au and Au-V (2.2 at. % V) surfaces and their surface grains. A simple linear intercept method in [41], calculates the average grain size. There is no abnormal grain growth observed in either of the pure Au or Au-V film surface. The images show obvious reduction of the average grain size from about 133 nm of the pure Au MCD to about 58 nm of the Au-V MCD. Smaller grain size posts more friction preventing the grain dislocation inducing creep/stress relaxation.

Conductivity of vanadium is lower than gold. To see its impacts on the filter performance. We conducted a experiment reveals the impacts of filter's RF performance due to employing Au-V MCD. Insertion loss and extracted unloaded quality factor of filters equipped with Au and Au-V diaphragms are compared in Fig. 2.23. Both filters have the same Au sputtered cavity. The results show that by introducing vanadium in the membrane additional loss of 0.15 to 0.9 dB is generated resulting in an effective quality factor penalty of 30-35%

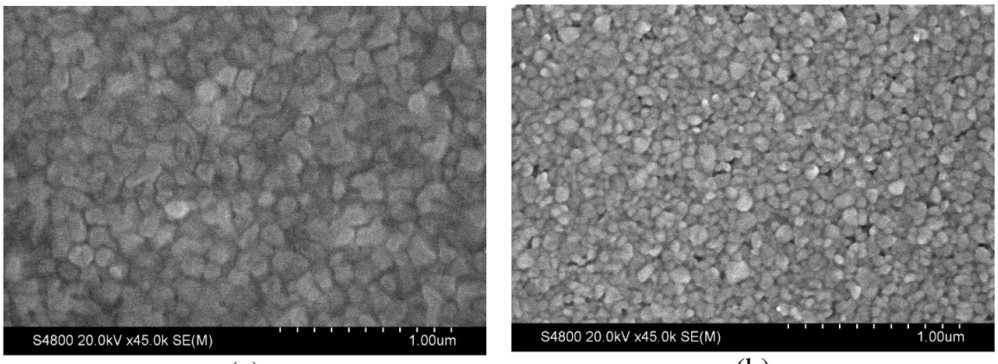

(a) (b)

Fig. 2.22. SEM images of surface grains of (a) pure Au and (b) Au-V (2.2 at.% V) MCDs.

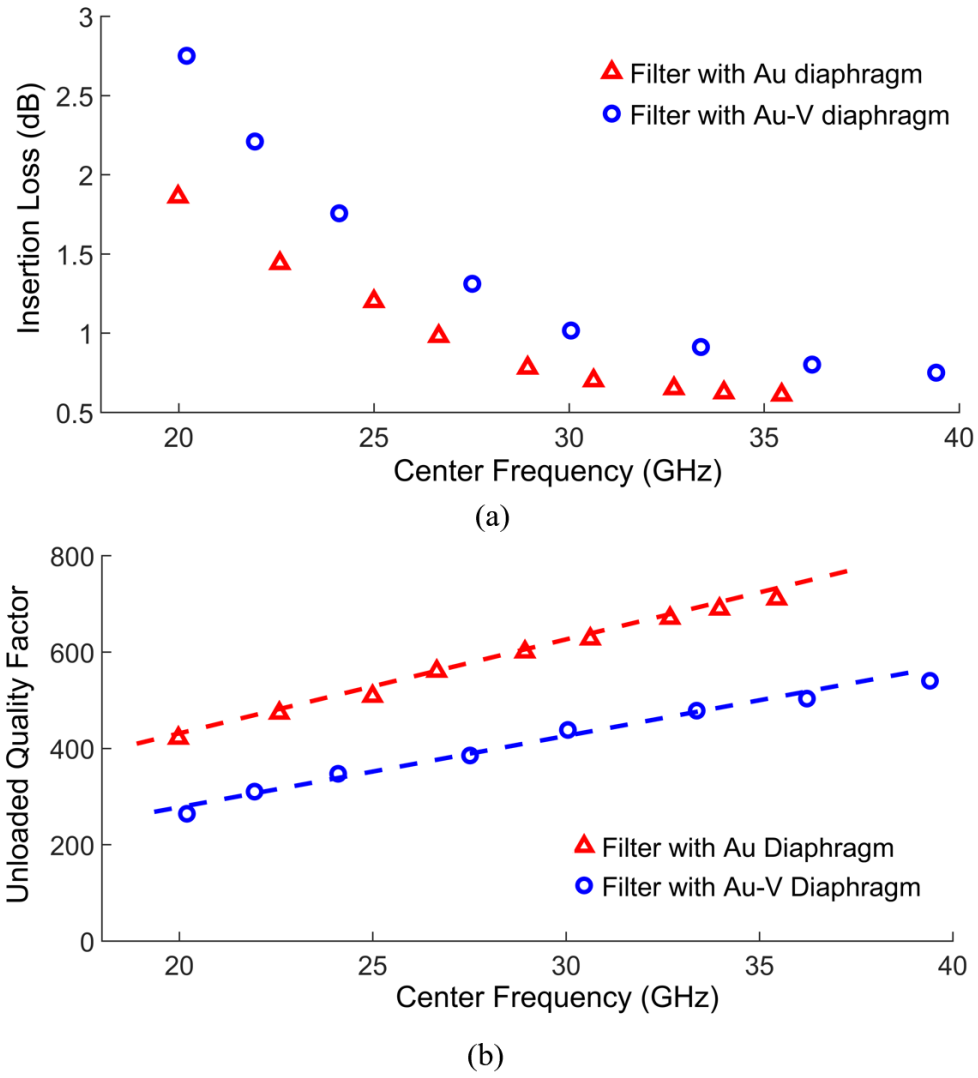

Fig. 2.23. (a) Measured insertion loss with connector loss de-embedded. (b) Extracted unloaded quality factor.

We also performed In-Package frequency stability measurements on the same setup as the S-parameter measurement setup. To simplify the process, only the resonance of one of the resonators is recorded. The resonance of the other resonator is placed at a distance larger than 10 GHz from the resonator under test. Initially, the frequency of the resonator is recorded at a zero-biasing level (relaxed membrane) which corresponds to a frequency of 20 GHz. Subsequently, a constant DC bias voltage is applied to drive the resonance to the designated frequency (24 GHz for this measurement) and the frequency drift data

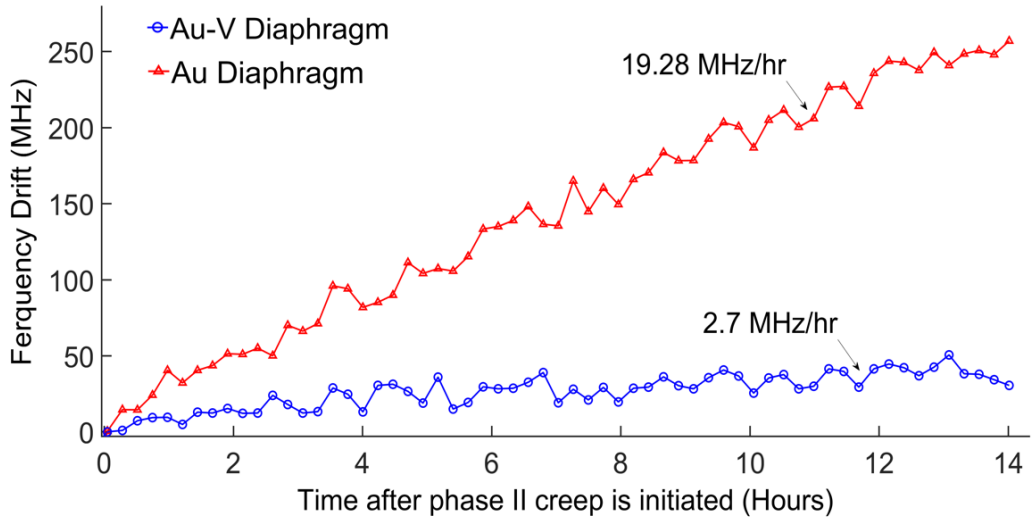

Fig. 2.24. Measured frequency drift after phase II creep is initiated. The measured center frequency is 24 GHz.

is recorded over time. The obtained response (both for Au and Au-V) is summarized in Fig. 2.24. The recorded drift is due to phase II creep also known as the second stage creep. More details are available in [43]. In this stage the creep rate is approximately constant. The Au-V diaphragm exhibits a 7× slower phase II creep rate than the pure Au case that corresponds to a frequency drift rate around 2.7 MHz/hr. Summarizing the above, it is apparent that there is a trade-off between mechanical stability and RF performance when pure Au and Au-V composites are employed. It is a preferable trade-off for most of the applications. Furthermore, a closed feedback control loop [44] can eliminate such drift issue.

2.7 Technology Summary and Design Rules

Based on the prototype fabrication, assembly, and experiments data, Table 2.1 and Fig. 2.25 present the most critical practical realization aspects of the MEMS tunable all-silicon cavity technology and the chosen geometrical details for the further development. They are summarized as: i) maximum MEMS deflection, ii) minimum capacitive gap, iii) slope of

the cavity walls and iv) minimum radius of the cavity post. The selected microfabrication and assembly processes dictates most of these. Specific constraints are described below.

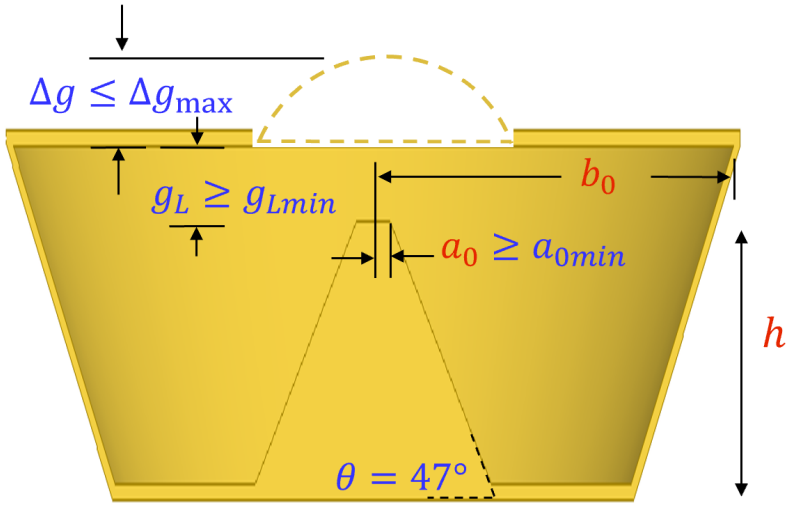

Fig. 2.25. General Design Constraints of MEMS Tunable EVA Filter.

The loading capacitance of the EVA resonator dictates the filter's tuning range. This can be increased by achieving a larger MEMS displacement Δg and by starting from a smaller initial RF gap g_L. We note, however, that larger Δg requires higher DC bias and induces more tensile stress that makes the MEMS diaphragm susceptive to creep. This is particularly critical when viscoelastic metals such as Au are employed [40]. Such issues can be mitigated by introducing corrugations on the MEMS diaphragm that alleviate the stress and creep as discussed in [13]. As such the maximum acceptable DC bias voltage and diaphragm creep rate set the limit for the maximum diaphragm deflection. This is quantified around 15 μm for the MCD used in this work. The minimum initial gap g_L is mostly limited by manufacturing issues and mostly substrate roughness and post-release diaphragm bending. For silicon substrates roughness is negligible compared to the post-release diaphragm bending. As a result, the fabrication process needs to be well tuned to minimize the diaphragm's initial bending. In this work we achieve this by performing a pre-release MEMS-to-cavity bonding that prevents diaphragm buckling during the bonding process. The alternative process of post-release bonding induces severe thermal stresses that typi-

cally lead to unacceptably high post-release diaphragm deflection. Using this process we can minimize g_L to about 1.2 μm with an uncertainty of less than 0.2 μm.

Employing silicon as a structural material for this filter technology also brings some practical realization considerations. In order to realize high-Q_u air-filled cavities, their bulk micro-machined sidewalls need to exhibit low surface roughness as well as to be coated with at least a 1-μm thick metallization layers (i.e. thicker than the skin depth: 0.43 μm at 30 GHz). Smooth cavity walls are achieved with anisotropic wet-etching based on a TMAH + triton X-100 solution. This process though results in undercuts that in turn limit the minimum achievable center post top radius a_0 as discussed in [37]. After performing a set of in-house microfabrication experiments, the minimum post top surface radius was found to be around 55 μm without post shape deterioration. However, such an etching recipe creates 47° sidewalls that need to be considered during the RF design of these filters.

2.8 Related Publications

- **Z. Yang**, and D. Peroulis,"A 23-35 GHz MEMS tunable all-silicon cavity filter with stability characterization up to 140 million cycles, in *IEEE MTT-S Int. Microw. Symp.Dig.*, Tampa, USA, 2014, pp. 1-3.

- **Z. Yang**, and D. Peroulis,"A 20-40 GHz tunable MEMS bandpass filter with enhanced stability by gold-vanadium micro-corrugated diaphragms, in *IEEE MTT-S Int. Microw. Symp.Dig.*, San Francisco, USA, 2016, pp. 1-3.

- **Z. Yang**, D. Psychogiou, and D. Peroulis, "Design and optimization of tunable silicon-integrated evanescent-mode bandpass filters" *IEEE Tran. Microw. Theory Tech.*, vol. 66, no. 4, pp. 1790-1803, Jan. 2018.

- **Z. Yang**, R. Zhang, and D. Peroulis, "Design and optimization of bi-directional tunable MEMS all-silicon evanescent-mode cavity filter" *IEEE Tran. Microw. Theory Tech.*, under review.

Table 2.1.
General Design Constraints of MEMS Tunable EVA Cavity Filter

Design Constraints	Root-of-Cause	Performance Impacts	Values used
Maximun tuner deflection	Tuner specifications	Tuning range, stability and tuning voltage	15 μm
Minimun RF gap	Substrate and assembly tolerance	Tuning range	1.2 μm
Cavity side wall slope	Substrate machining method	Resonator and coupling structure modeling	47°
Minimun post top radius	Fabrication tolerance	Tuning range, quality factor	55 μm

3. ADVANCED FILTER DESIGN AND OPTIMIZATION

3.1 Resonator Design

3.1.1 Analytical Resonator Model

Figure 3.1(a) shows a conceptual drawing of the EVA resonator in all-silicon technology. As mentioned before, wet-cavity etching results in inclined cavity walls as opposed to the vertical ones of a conventional coaxial resonator. The electromagnetic (EM) field distribution within the cavity resembles the TEM mode of a pure coaxial line. As such, the all-silicon resonator architecture can be modeled as a capacitively-loaded tapered coaxial line as shown in the circuit schematic in Fig. 3.1(b). Its characteristic impedance Z_0 at position x can be calculated as:

$$Z_0(x) = \frac{1}{2\pi}\sqrt{\frac{\mu_o}{\varepsilon_o}}\ln\left(\frac{b_0 - \frac{x}{tan(\theta)}}{a_0 + \frac{x}{tan(\theta)}}\right) \tag{3.1}$$

in which a_0 and b_0 are the inner and outer conductor radii at $x = 0$ (Fig. 3.1(a)). Such a linear variation of the inner/outer conductor radius results in a non-linear impedance change. To better model its response, we follow the design approach depicted in Fig. 3.2(a). Specifically, the tapered line segment is discretized into N electrically-short non-tapered coaxial lines whose inner/outer conductor ratio equals the mean ratio of the corresponding tapered line section. For each section we compute its equivalent ABCD matrix leading to a straight-forward calculation of the overall ABCD matrix. The overall ABCD matrix represents an equivalent π-type network [45] with a series inductance L_{coax} and two parallel capacitances C_1, C_2 to ground, Fig. 3.2(a).

To demonstrate this model we apply the aforementioned analysis to an EVA tunable resonator with $a_0 = 0.11$ mm, $b_0 = 2.4$ mm, $h = 1.5$ mm and $\theta = 60°$. Fig. 3.2(b) plots the calculated L_{coax}, C_1, C_2, as a function of the number of transmission line segments N. They are plotted normalized to the $N = 1$ value. As can be seen, all equivalent circuit parameters

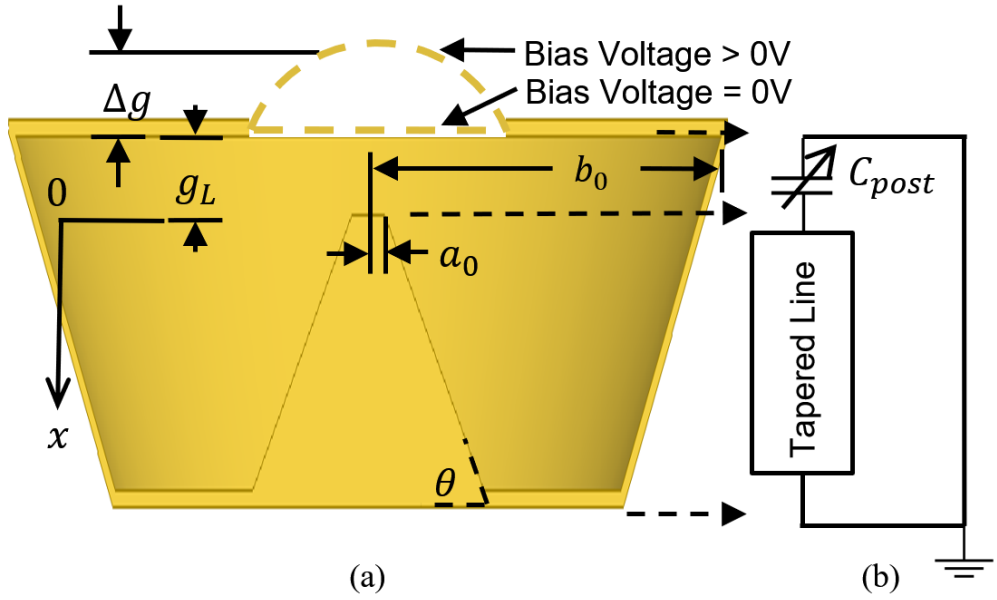

Fig. 3.1. Conceptual drawing of the EVA cavity resonator in all-silicon technology. (a) Cross-section view of the resonator. (b) Equivalent circuit model.

converge for $N \geq 4$. The values of the modeled circuit parameters are also compared to HFSS simulations. While L_{coax} agrees well to the HFSS results, both capacitances are underestimated. This is because the proposed model ignores the vertical electric field caused by the inclined side walls. Nevertheless, this is not a serious limitation, because a) C_2 is shorted and b) C_1 is in parallel with and much smaller than C_{post}. As shown below, even a large error in C_1 hardly affects the computed resonant frequency since it is much smaller than C_{post}.

Besides the TEM mode, part of the electric field energy is stored in an electric field distribution similar to the TM_{010} mode. This part of electric energy is modeled as C_{plate} as shown in Fig. 3.3(a). As expected, this mode is significant only when C_{post} is small, i.e. only when the cavity is not heavily loaded. This is clearly shown in Fig. 3.3(b). To quantify the significance of C_{plate}, the resonance frequency ω_0 is calculated assuming C_{plate} is negligible so as:

$$\omega_0 \approx 1/\sqrt{L_{coax}(C_{post} + C_1)} \tag{3.2}$$

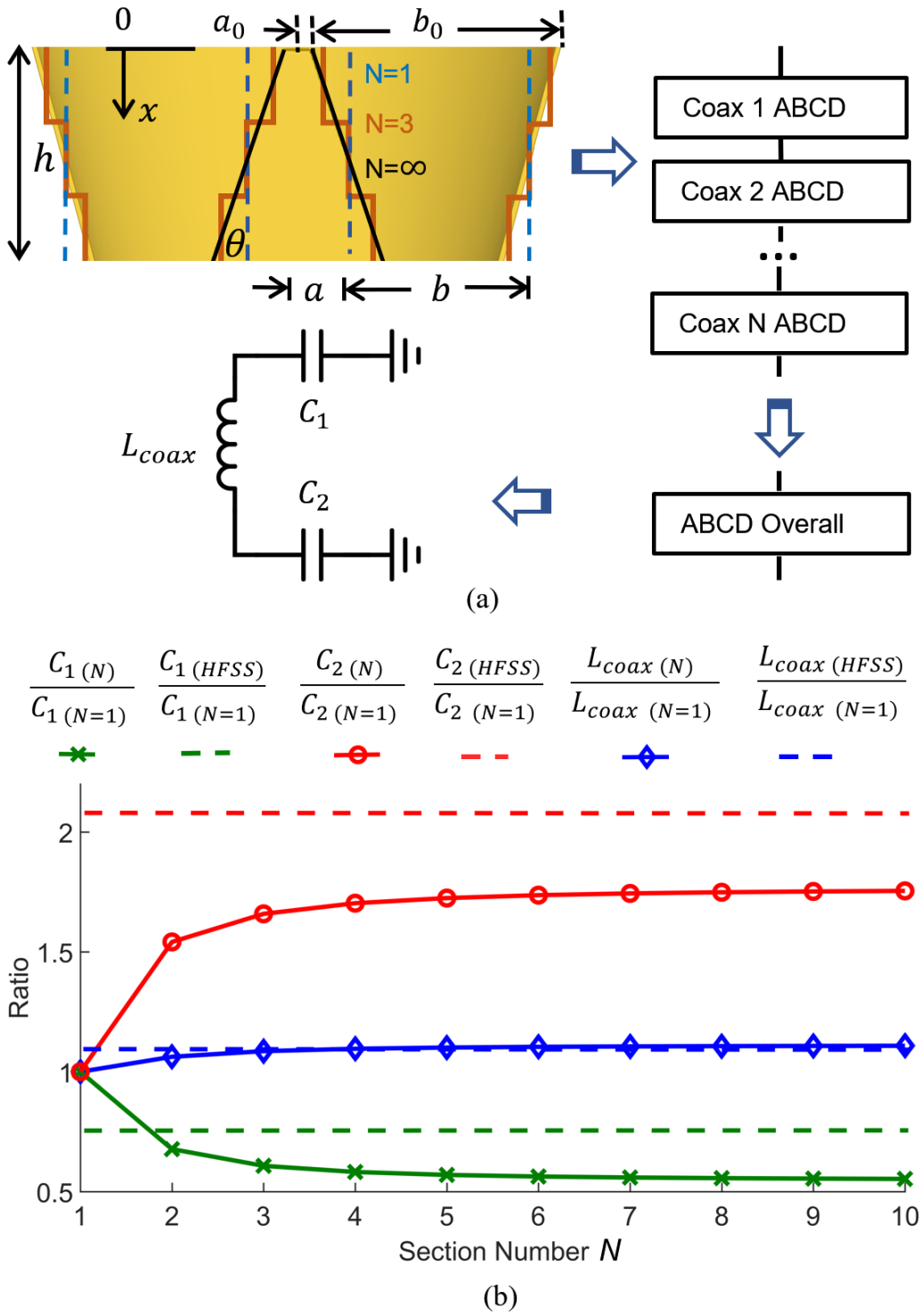

Fig. 3.2. Tapered coaxial line. (a) 1-D discretization approach and its resulting equivalent π-type circuit model. (b) Equivalent circuit parameters for different number (N) of transmission line segments.

and plotted in Fig. 3.3(b). Comparing these to HFSS results shows that we may get a 10% error if C_{plate} is ignored. While it is not easy to analytically model C_{plate}, HFSS simulations can easily estimate it if higher than 10% modeling/design accuracy is desired.

To summarize, the parallel combination of C_{post}, C_1, and C_{plate} forms the total capacitance of the resonator

$$C_{resonator} = C_{post} + C_1 + C_{plate}. \tag{3.3}$$

For micrometer-scale capacitive gaps (1 to 20 μm in this case), C_{post} in parallel with C_{plate} tend to dominant as they are typically 5× larger than C_1. As such, a 20% error in C_1 will not generate significant error on the center frequency estimation, Fig. 3.3(b). In other words, we observe no significant difference in the calculated ω_0 by increasing the modeling section number N from 1 to 4. For simplicity, therefore, we can model the tapered line by using just a single section ($N = 1$ in Fig. 3.3). Based on the above analysis, L_{coax} and C_1 can be approximated as

$$L_{coax} \approx \frac{1}{6\pi \times 10^8} \sqrt{\frac{\mu_0}{\varepsilon_0}} \ln\left(\frac{b}{a}\right) h \tag{3.4}$$

$$C_1 \approx \frac{2\pi}{6 \times 10^8 \sqrt{\frac{\mu_0}{\varepsilon_0}} \ln\left(\frac{b}{a}\right)} h. \tag{3.5}$$

3.1.2 Tuning Range Analysis

According to the schematic shown in Fig. 3.3(a) and assuming C_{post} is significantly larger than C_1, the frequency tuning ratio can be calculated as

$$\frac{\omega_{0H}}{\omega_{0L}} = \left(\frac{g_L}{g_L + \Delta g_{max}} + \frac{C_1 + C_{plate}}{C_{postL}}\right)^{-\frac{1}{2}} \tag{3.6}$$

in which ω_{0H}, ω_{0L} are the highest and lowest frequencies of the tuning range. The capacitance C_{postL} represents the initial post capacitance when the MEMS tuner is at its unbiased position. This can be approximated as

$$C_{postL} \approx \frac{\varepsilon_0 \pi a_0^2}{g_L}. \tag{3.7}$$

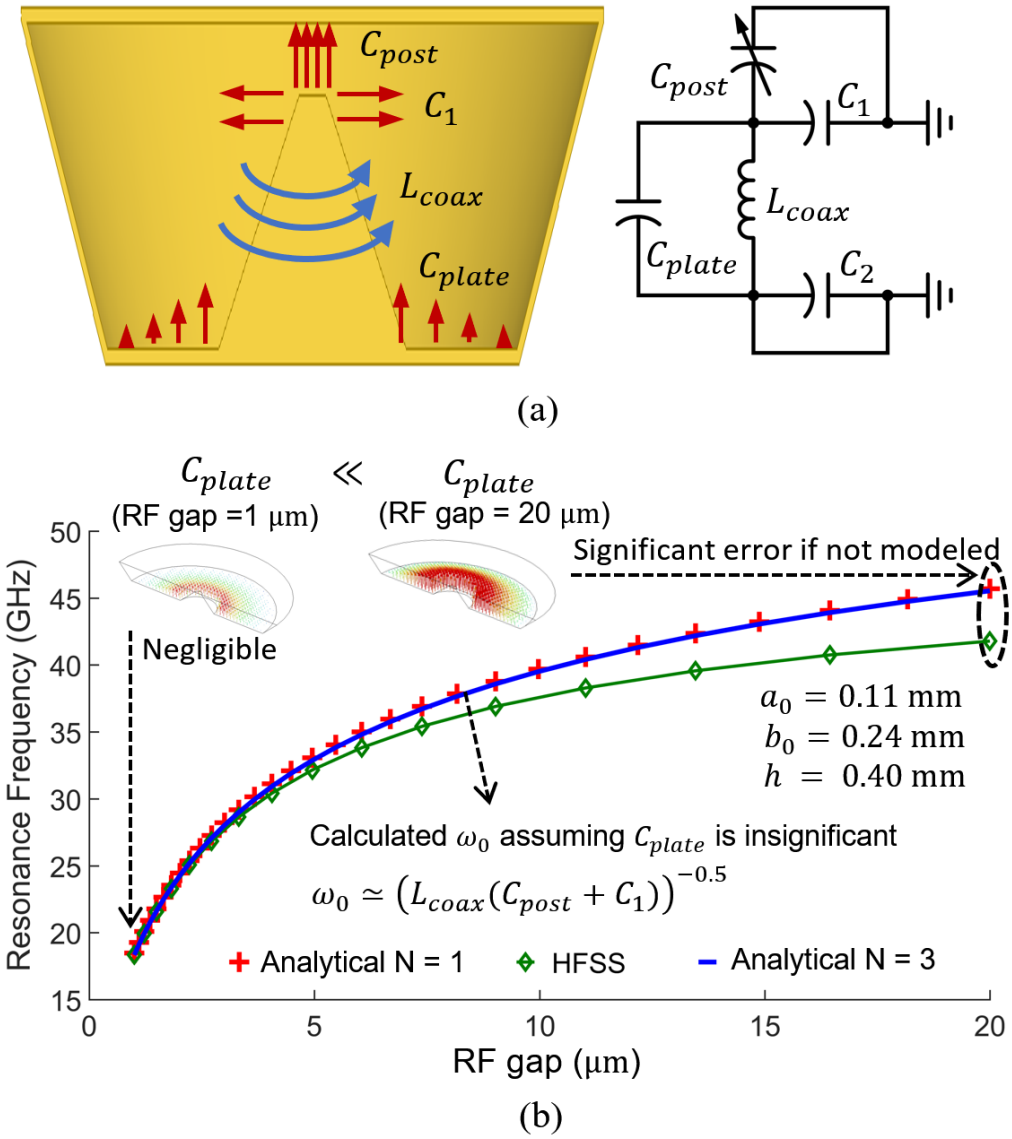

Fig. 3.3. (a) Equivalent circuit of an all-silicon EVA resonator. (b) Resonance frequency versus capacitive gap.

Note that the first term in (3.6) is controlled by the MEMS tuner deflection, while the second term is mostly related to the cavity dimensions. A larger tuning ratio can be achieved for a smaller initial gap g_L. Consequently, we fix g_L to the smallest initial RF gap g_{Lmin} that can be manufactured or tolerated from a power handling point of view [30]. With a fixed g_L, C_{postL} is only related to a_0. The second term in (3.6) also shows that larger C_{postL} (i.e. a_0) leads to higher tuning range. We should also keep in mind that for each selected C_{postL} (or a_0), there exists an optimal set of b and h that minimize the numerator—$C_1 + C_{plate}$—of the second term in (3.6) leading to the highest possible tuning ratio.

We can obtain further insight on these aspects by inserting (3.4) and (3.7) into $\omega_{0L} = 1/\sqrt{L_{coax}C_{postL}}$. This yields

$$h = \frac{g_L(6\times 10^8)}{\omega_{0L}^2 a_0^2 \sqrt{\mu_0\epsilon_0}} \frac{1}{\ln\left(\frac{b}{a}\right)}. \tag{3.8}$$

This equation defines the b-h relationship for given a_0, g_L and ω_{0L}. Also this equation for h can be used in (3.5) to calculate C_1. This allows us to make the following observations. First, a low C_1 requires a large b; h will be calculated by (3.8). On the other hand, a large b value increases C_{plate} —please see design example in Fig. 3.4(b). As a result, there is an optimal set of b and h to minimize the sum of $C_1 + C_{plate}$. This optimization is better performed with the aid of an FEM simulator.

Let us demonstrate this optimization process for a resonator with vertical sidewalls shown in Fig. 3.4(a). In this example, $g_L = 1$ μm, $\Delta g_{max} = 19$ μm and $\omega_{0L} = 20$ GHz. If the post radius is chosen as $a_0 = 90$ μm, (3.8) will return various possible cavity designs with different aspect ratios. As shown in Fig. 3.4(a) the maximum tuning ratio is obtained for $h = 0.6$ mm and $b = 0.83$ mm. In general, high-aspect ratio cavities should be avoided when a large tuning range is required.

Fig. 3.4(b) summarizes the $C_{resonator}$ and C_{plate} values at the ω_{0H} tuned state as extracted by the values shown in Fig. 3.4(a). The analytically-calculated C_1, L_{coax} and FEM-simulated C_{post} values have been used here. As expected, there exists an optimal b value that maximizes the tuning range.

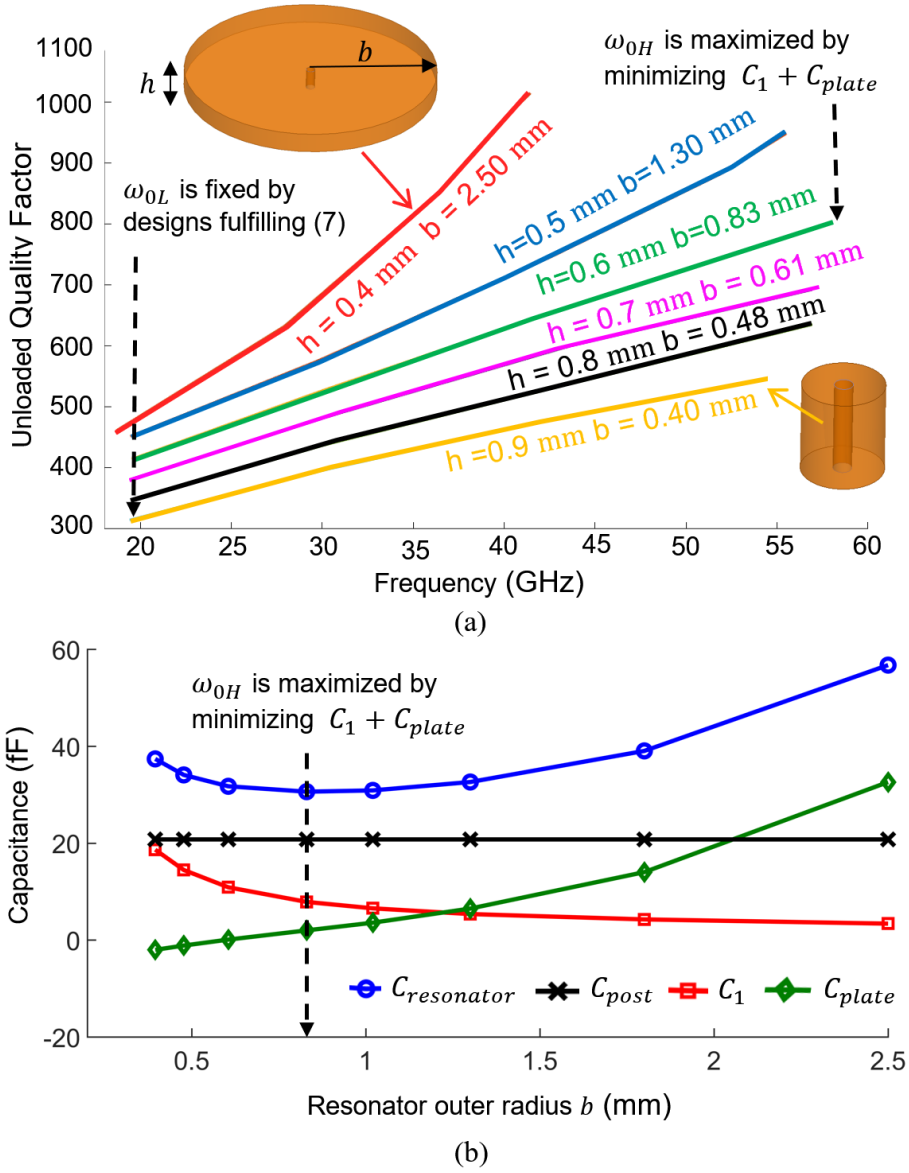

Fig. 3.4. (a) Simulation results of unloaded quality factor and tuning range for a given RF gap variation of 19 μm, center post radius of 90 μm and initial gap of 1 μm. (b) Extracted capacitances versus different cavity designs with various b values.

3.1.3 Quality Factor Analysis and Optimization

The analytical equation for Q_u of an EVA cavity resonator has been derived in [46] as $Q_u = \frac{\omega_0\mu_0}{R_s}\frac{\ln\left(\frac{b}{a}\right)h}{\left(\frac{1}{a}+\frac{1}{b}\right)h+2\ln\left(\frac{b}{a}\right)}$ where R_s is the sheet resistance of the cavity sidewalls. In [46], the optimum relationship for maximum Q_u is obtained when the ratio between the inner and outer radii equals 0.28. However, this is only valid for static resonator designs. A new design approach is needed for a tunable design particularly when many practical design and fabrication considerations have been to be taken into account.

Four independent design variables (g_L, a, b, h) along with the required tuning range and fabrication limitations dominate Q_u. There is no easily-derived analytical equation that directly leads to optimized cavity dimensions. Numerically exhaustive searching is also impractical. Nevertheless, we obtain useful insights by reorganizing the aforementioned Q_u expression as

$$Q_u = \frac{\omega_0\mu_0}{R_s(2\times 10^{-7})}\frac{L_{coax}}{\left(\frac{1}{a}+\frac{1}{b}\right)h+2\ln\left(\frac{b}{a}\right)}. \tag{3.9}$$

It is interesting to note that $\frac{\partial(Q_u)}{\partial(L_{coax})}$ is significantly higher than any of the other partial derivatives ($\frac{\partial(Q_u)}{\partial(a)}$, $\frac{d\partial(Q_u)}{\partial(b)}$ and $\frac{\partial(Q_u)}{\partial(h)}$). Thus Q_u is dominated by L_{coax}. Consequently, as shown by (3.6) and (3.9), although a large L_{coax} leads to high Q_u, it also leads to a small C_{postL} and reduced tuning ratio. It is clear then that Q_u and tuning ratio is an important trade-off pair. The right strategy is to find a design that meets the tuning range requirement with the smallest possible C_{postL} and thus the highest possible Q_u.

The iterative optimization procedure is summarized then as follows

1. Decide on the minimum gap $g_L = g_{Lmin}$ based on fabrication limitations and the needed power handling/linearity requirements [30].

2. Start by setting a_0 to its smallest fabrication-achievable value a_{0min}. This will result to the minimum C_{postL} for the given gap $g_L = g_{Lmin}$ and therefore the highest Q_u.

3. Find the largest possible tuning range by optimizing the cavity aspect ratio with the procedures detailed in the previous sub-section B.

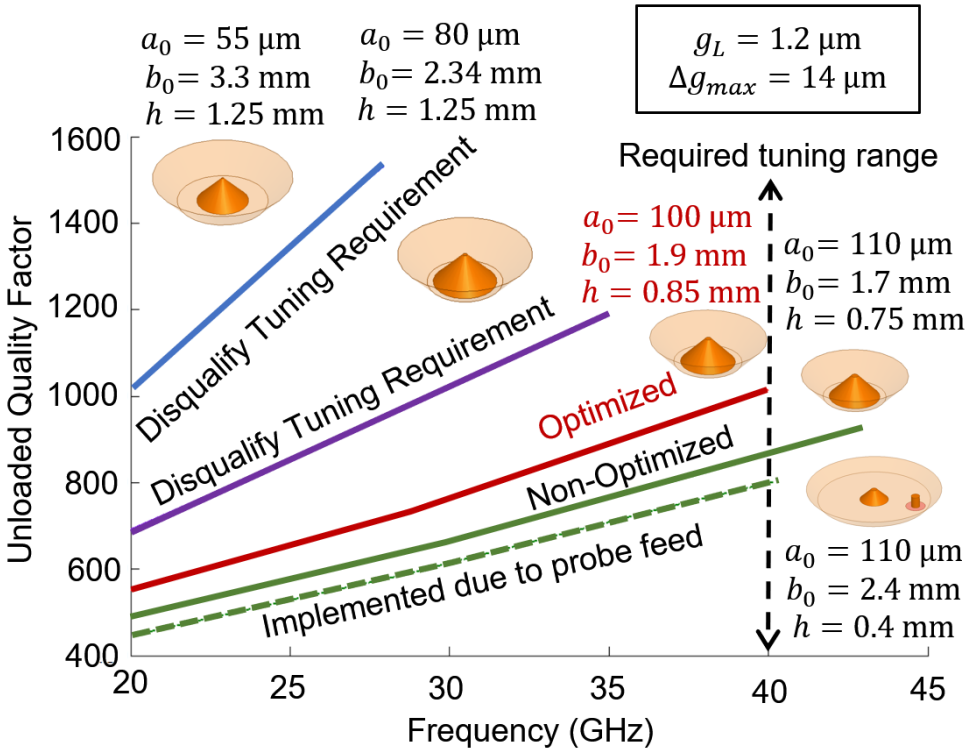

Fig. 3.5. Quality factor optimization of a 20-40 GHz resonator that fulfills all tuning requirements under design constraints.

4. If the achieved tuning range is smaller than the target, increase a_0 until the obtained tuning ratio reaches the target. If the achieved tuning range is higher than the target, increase g_L (so to increase Q_u as well as power handling) and repeat steps 2 to 3.

A design example of a 20 to 40 GHz resonator is illustrated in Fig. 3.5. The design constraints for this work are listed in Table I. By following the above design procedures, we see that for designs with a_0 less than 100 µm there is no practical solution that fulfills the tuning requirements. The red solid line in Fig. 3.5 is the best possible design in the sense that all remaining solutions will have larger than required tuning range at a cost of lower Q_u. The design implemented in this work is shown with the dashed green line in Fig. 3.5 (a_0 = 110 µm, b_0 = 2.4 mm, h = 0.4 mm). Such design was necessary due to a) the bottom area requirement for the coaxial probe feed, b) limited choices of available wafer thicknesses and c) in-house fabrication capabilities.

3.2 Inter-Resonator Coupling Design

The general inter-resonator coupling structure of an all-silicon EVA tunable filter is shown in Fig. 3.6. Note that, adjacent EVA resonators are synchronously or asynchronously tuned and coupled through a coupling iris whose cross-section is a trapezoid due to anisotropic silicon etching. This is represented in Fig. 3.6(a) with a solid line. As reported in [47], such waveguide can be approximated as an equivalent rectangular waveguide with width W shown in Fig. 3.6(a) (dashed line). The depth of the iris—defined by silicon wet-etching—is the same as the resonator depth h. The coupling strength is determined by the resonator separation D and the iris width W. While for a single-frequency design a range of D and W values provide the required coupling strength, the situation is more complex for a tunable filter. In the latter case it is important to select the optimal D and W values that minimize bandwidth variation over the tuning range while simultaneously providing the needed coupling strength. To this end, it is preferable to have an analytical model that guides the inter-resonator coupling structure design process.

Significant research results [48–50] have been reported in the literature regarding the design and modeling of evanescent mode waveguide bandpass filters. The inter-resonator coupling section is defined as the area between the two cavity posts. Capacitive loading on the cavity post drives the coupling section under evanescent mode operation. In [48] an evanescent-mode coupling section without step-discontinuity ($W = 2b$) is modeled as a transmission line assuming only the fundamental TE_{10} mode within the coupling section. It is also capacitively loaded as shown in Fig. 3.7(c). The evanescent-mode characteristic impedance jX_0 of the transmission line and its propagation constant γ_0 can be calculated as

$$jX_0 = j\frac{465h}{W\sqrt{(\frac{\lambda}{2W})^2 - 1}} \tag{3.10}$$

$$\gamma_0 = \frac{2\pi}{\lambda}\sqrt{(\frac{\lambda}{2W})^2 - 1}. \tag{3.11}$$

In this work, the diameter of the loading post is small compared to the outer conductor. As such, the inductance associated with the coaxial structure is not negligible. The resonator inductance—derived in Section III as L_{coax}—is included in parallel to C_{post}. In

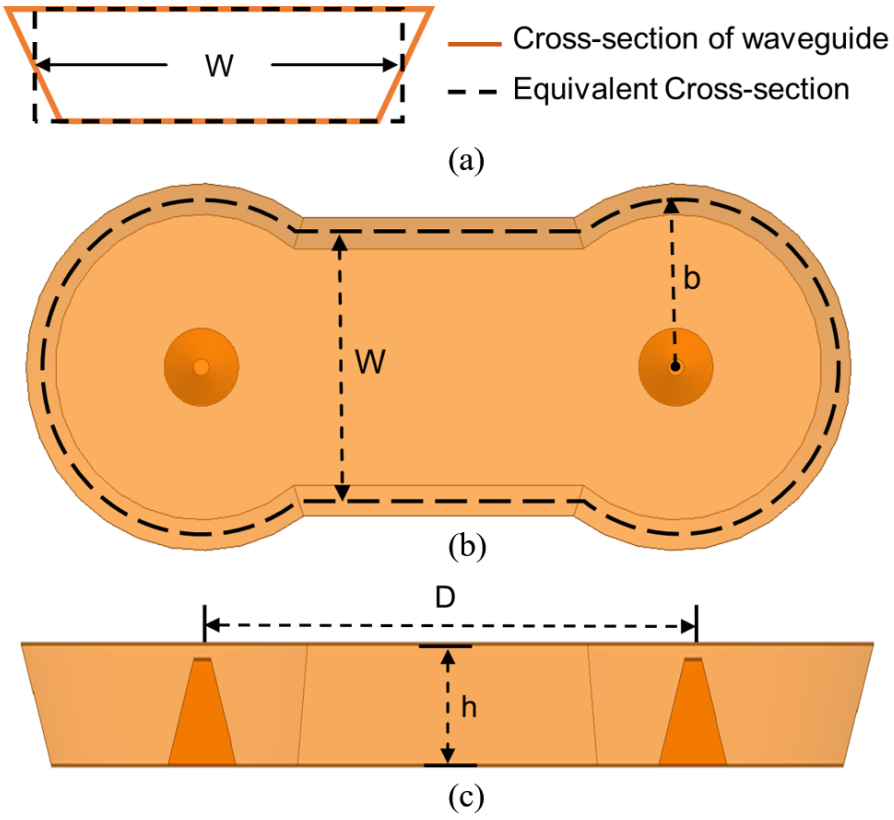

Fig. 3.6. (a) Equivalent rectangular waveguide for a tapered waveguide, (b) Top-view of inter-resonator coupling structure, (c) Side-view of inter-resonator coupling section.

addition, the model is further generalized for a coupling structure with step discontinuities as shown in 3.7(b). The shunt susceptance generated by the step discontinuity assuming the TE_{10} mode has been derived in [51]. Such susceptance behaves as a lumped inductor L_{step} whose value is negative within the frequency range under its cutoff frequency. The analytical expression of L_{step} based on the geometry shown in Fig. 3.6 can be written as

$$L_{step} = -\frac{465\frac{h}{W}(4b)(1-\rho/2)}{2\pi(3\times 10^8)(\rho^2(1+\rho)\ln\frac{2}{\rho})} \tag{3.12}$$

where $\rho = 1 - W/2b$ is the geometrical ratio of the step discontinuity.

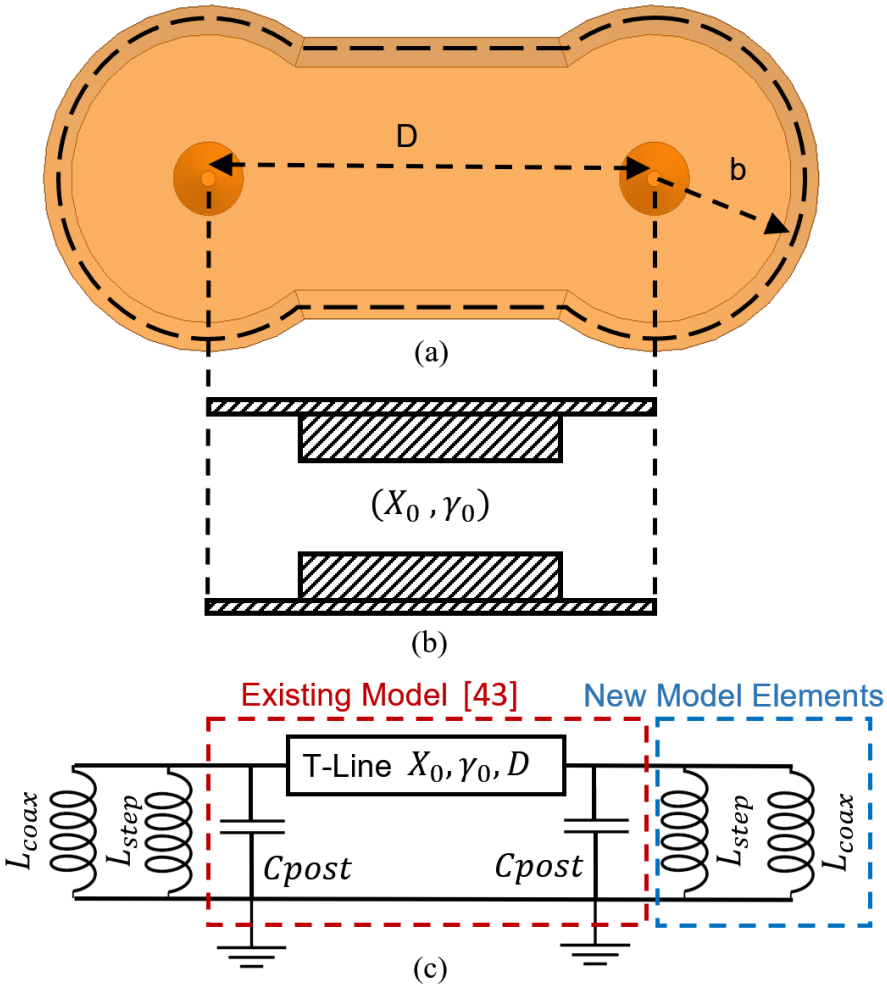

Fig. 3.7. (a) Top-view of inter-resonator coupling structure, (b) Equivalent inter-resonator coupling structure, (c) Equivalent circuit of the coupled resonators.

The evanescent-mode transmission line in Fig. 3.7(c) can be transformed into an equivalent π-network and rearranged as the circuit shown in the blue box in Fig. 3.8 with the following parameters

$$L_m = \frac{X_0 \sinh \gamma_0 D}{\omega} \tag{3.13}$$

and

$$L_e = \frac{X_0 \tanh \gamma_0 D}{\omega}. \tag{3.14}$$

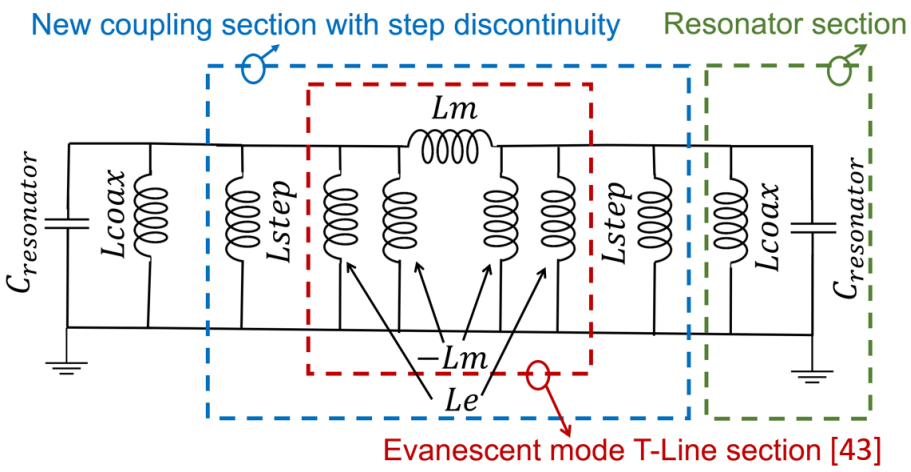

Fig. 3.8. Further derived equivalent circuit of the coupled resonators.

Thus the circuit shown in Fig. 3.8 is in the form of a coupled resonator and the coupling coefficient can be calculated as $K(\omega) = (L_e \parallel L_{coax} \parallel L_{step})/L_m$ by linear circuit analysis. However, both L_m and L_e are non-linear in the sense that both inductance values are frequency dependent. Such disagreement is fixed by multiplying a correction factor Δ which is derived in the appendix of [48]. In this work, the model is expanded with two extra elements, L_{coax} and L_{step}. Consequently, the original formula of Δ is re-derived into

$$\Delta' = \frac{2}{1 + \frac{L_e \| L_{coax} \| L_{step}}{L_{coax} \| L_{step}} + \frac{1}{1-(\frac{\lambda_c}{\lambda})^2}\left(1 - \frac{L_e \| L_{coax} \| L_{step}}{L_{coax} \| L_{step}}\right)} \tag{3.15}$$

in which $\lambda_c = 2W$ is the cut-off wavelength. Equation (3.15) is reduced to the original $\Delta = 2\left(1 + \frac{1}{1-(\lambda_c/\lambda)^2}\right)^{-1}$ by setting $L_{coax} = L_{step} = \infty$. The coupling coefficient $K(\omega)$ can be derived by using the aforementioned expressions for L_e, L_m as

$$K(\omega) = \frac{\Delta'}{\sinh(\gamma_0 D)\left(\frac{X_0}{\omega(L_{coax} \| L_{step})} + 1\right)}. \tag{3.16}$$

The validity and significance of the proposed circuit model is demonstrated by comparing it to HFSS simulations as shown in Fig. 3.9. To extract K from HFSS simulations we follow the process outlined in [52] for magnetically-coupled synchronously tuned res-

onators and write $K = (f_e^2 - f_m^2)/(f_e^2 + f_m^2)$. The frequencies f_e and f_m represent the even- and odd-mode resonant frequencies that correspond to the lowest two resonant frequencies obtained by HFSS eigenmode simulations. In Fig. 3.9(a) we validate L_{coax} with a coupled EVA resonator pair with no step discontinuity in the coupling section. The predicted K from the proposed model is in close agreement with the simulation results. In Fig. 3.9(b) we introduce a step discontinuity. The proposed model that includes both L_{step} and L_{coax} agrees well with the simulation results.

The aforementioned analysis and equivalent circuit assume that only the evanescent TE_{10} mode exists within the inter-resonator coupling region. Such approximation is valid only when the iris step discontinuity is small ($W/2b$ close to 1) or far from its adjacent resonator posts ($D/2b$ larger than 1). Otherwise, the above analysis underestimates the coupling strength due to excluding higher order modes generated by the step discontinuity. Full-wave simulation is necessary for accurate results when those higher order modes are significant. One way to make the model capture such effect is to replace the physical iris width W with an effective iris width W_e given by $W_e/W = m(D/2b)^{-n}(1 - W/2b)^2 + 1$. The coefficients $m = n = 1.5$ are extracted from numerical FEM experiments. As expected for large $D/2b$ or when $W/2b \approx 1$, W_e is equal to W.

As mentioned before, a widely-tunable filter imposes additional requirements on its coupling coefficient in order to minimize frequency dispersion. This can be quantified by calculating the derivative of (3.16). By keeping only the dominant terms, this derivative can be approximated as

$$\frac{\partial K}{\partial \omega} \simeq \frac{\Delta' D(-\frac{\partial \gamma_0}{\partial \omega})}{\sinh(\gamma_0 D)(\frac{X_0}{\omega(L_{coax}\|L_{step})} + 1)}. \tag{3.17}$$

Comparing to (3.16), (3.17) can be further simplified as

$$\frac{\partial K}{\partial \omega} \approx D\left|\frac{\partial \gamma_0}{\partial \omega}\right| K. \tag{3.18}$$

Typically this equation is minimized at the center of the band ω_{0M} where the optimal coupling is designed to be $K_{|\omega_{0M}} = FBWm_{ij}$ where FBW is the desired fractional band-

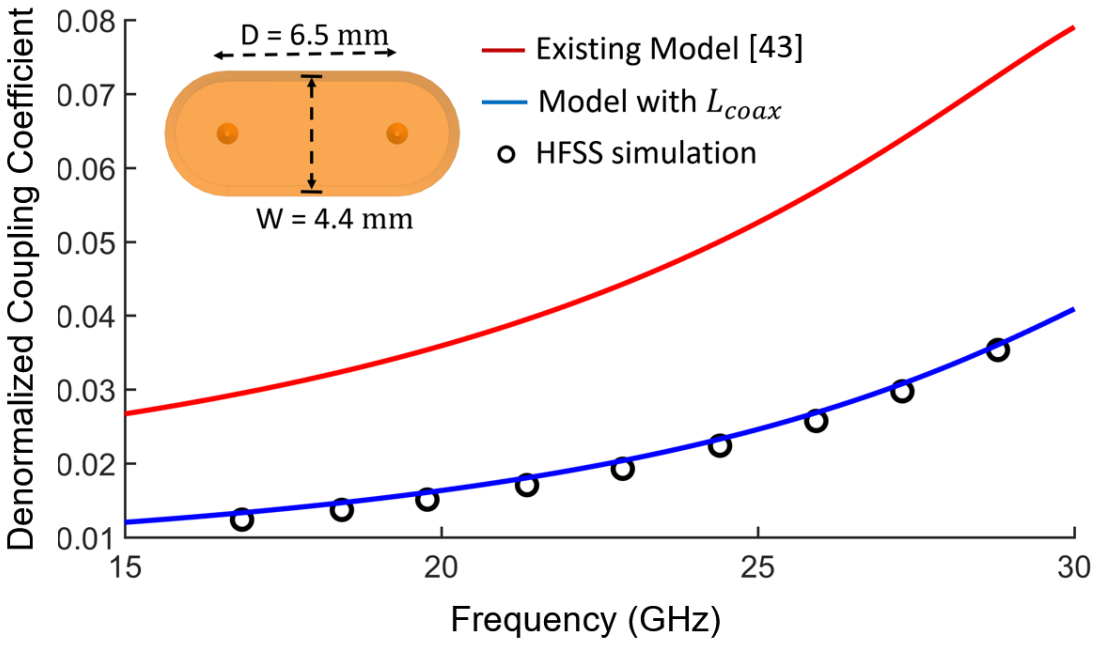

(a)

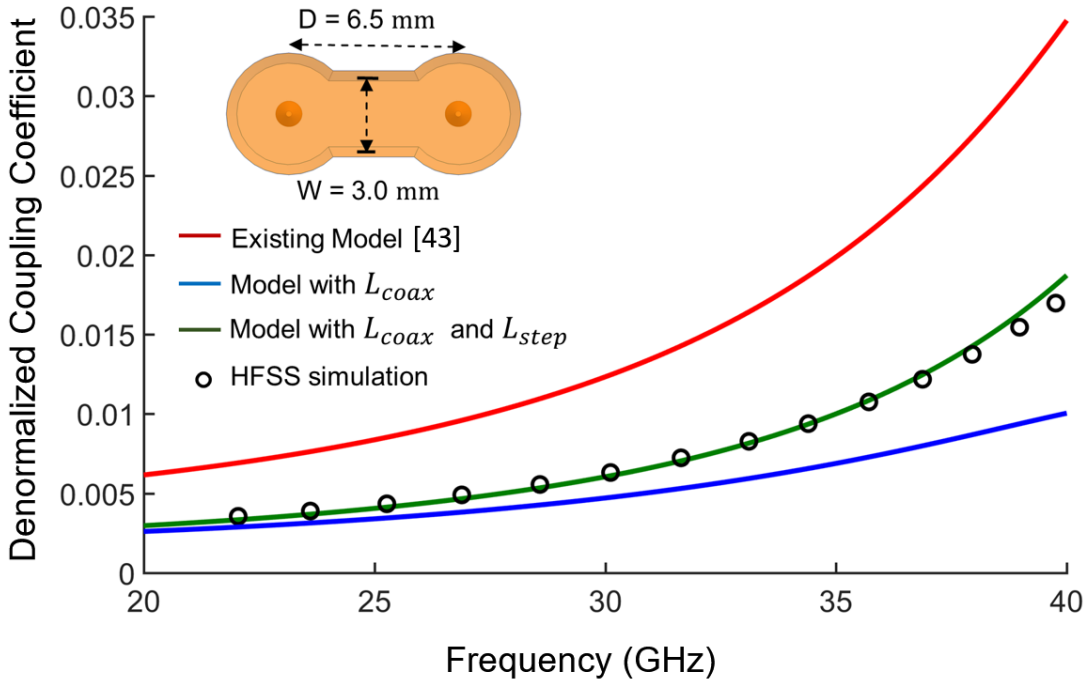

(b)

Fig. 3.9. (a) Model validation of coupling structure without iris. (b) Model validation of coupling structure with iris.

width and m_{ij} is the synthesized normalized coupling coefficient between the i-th and j-th resonators. Thus at the center of the band we have

$$\frac{\partial K}{\partial \omega}_{|\omega_{0M}} = D\left|\frac{\partial \gamma_0}{\partial \omega}\right|(FBWm_{ij}). \tag{3.19}$$

Based on the expression of γ_0 and (3.16), choosing a small W reduces $\frac{\partial \gamma_0}{\partial \omega}$ while it also results in a small D to maintain the same center-frequency condition $K_{|\omega_{0M}} = FBWm_{ij}$. Consequently, limiting frequency dispersion requires us to reduce W to the geometric limit $2b \geq W \geq 2\sqrt{b^2 - D^2/4}$.

This coupling design procedure is illustrated on a two-pole tunable filter example with FBW = 0.025 and $m_{12} = 0.707$. In Fig. 3.10 we have graphed the normalized coupling coefficient for different design choices. At the center of the tuning band (30 GHz) we have maintained $K_{|\omega_{0M}} = 0.017$ for all designs. As expected the worst results occur for the maximum possible width $W = 2b$. Optimal results are obtained for the smallest possible width $W = 2\sqrt{b^2 - \frac{D^2}{4}}$. We choose the coupling design with the lowest frequency dispersion achieved by $D = 4.3$ mm and $W = 1.9$ mm to proceed.

3.3 External Coupling Design

The external coupling mechanism scheme is shown in Fig. 3.11(a). We employ a magnetic coupling mechanism since nearly all electric field is concentrated on top of the post. Nevertheless, the presented design technique is not limited to the selected geometry. The external coupling coefficient is mainly controlled by the distance between the center pin of the coaxial probe and the center post (D_{probe}). This coupling structure can be represented by the equivalent circuit model shown in Fig. 3.11(b). In particular, the coupling to the resonator is modeled as an ideal transformer whose turn ratio n is a function of frequency and D_{probe}. A transmission line with characteristic impedance Z_0 and length L_{phase} is included to represent the phase shift that is generated by the coaxial probe discontinuity—calculated at the defined reference plane—. Due to the nature of this geometry, there exists no closed-form equation to accurately determine Q_e and L_{phase}. Hence numerical simulations need to be performed in order to extract the aforementioned parameters.

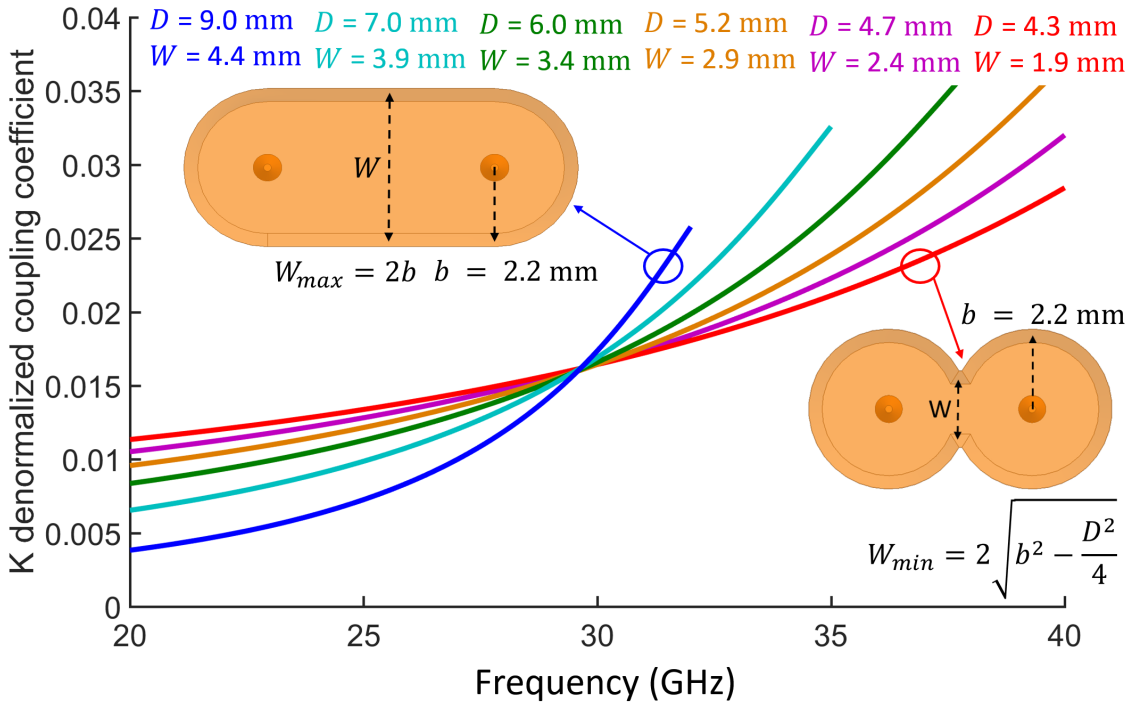

Fig. 3.10. Coupling structure design with frequency dispersion optimization.

As an example, we design the external coupling for the previously-selected resonator dimensions $a_0 = 0.11$ mm, $b_0 = 2.4$ mm and $h = 0.4$ mm. Both Q_e and L_{phase} are extracted by HFSS simulations. Specifically, L_{phase} is determined from the phase offset of the simulated reflection coefficient shown in the Smith chart of Fig. 3.11(c). The value of L_{phase} (0.85 mm in this case) does not depend on D_{probe} which confirms the validity of the suggested equivalent circuit model. With the simulated reflection coefficient S_{11}, Q_e can be extracted as $Q_e = \omega_0 \frac{\tau_{S11}(\omega_0)}{4}$ in which $\tau_{S11}(\omega_0)$ is the reflection group delay at the tuned resonance frequency ω_0. The extracted Q_e for various D_{probe} is plotted in Fig. 3.11(d). It can be seen that Q_e varies monotonically with D_{probe} and frequency. There is a unique D_{probe} value that yields the desired Q_e at a single tuned frequency (often taken as the center of the band ω_{0M}).

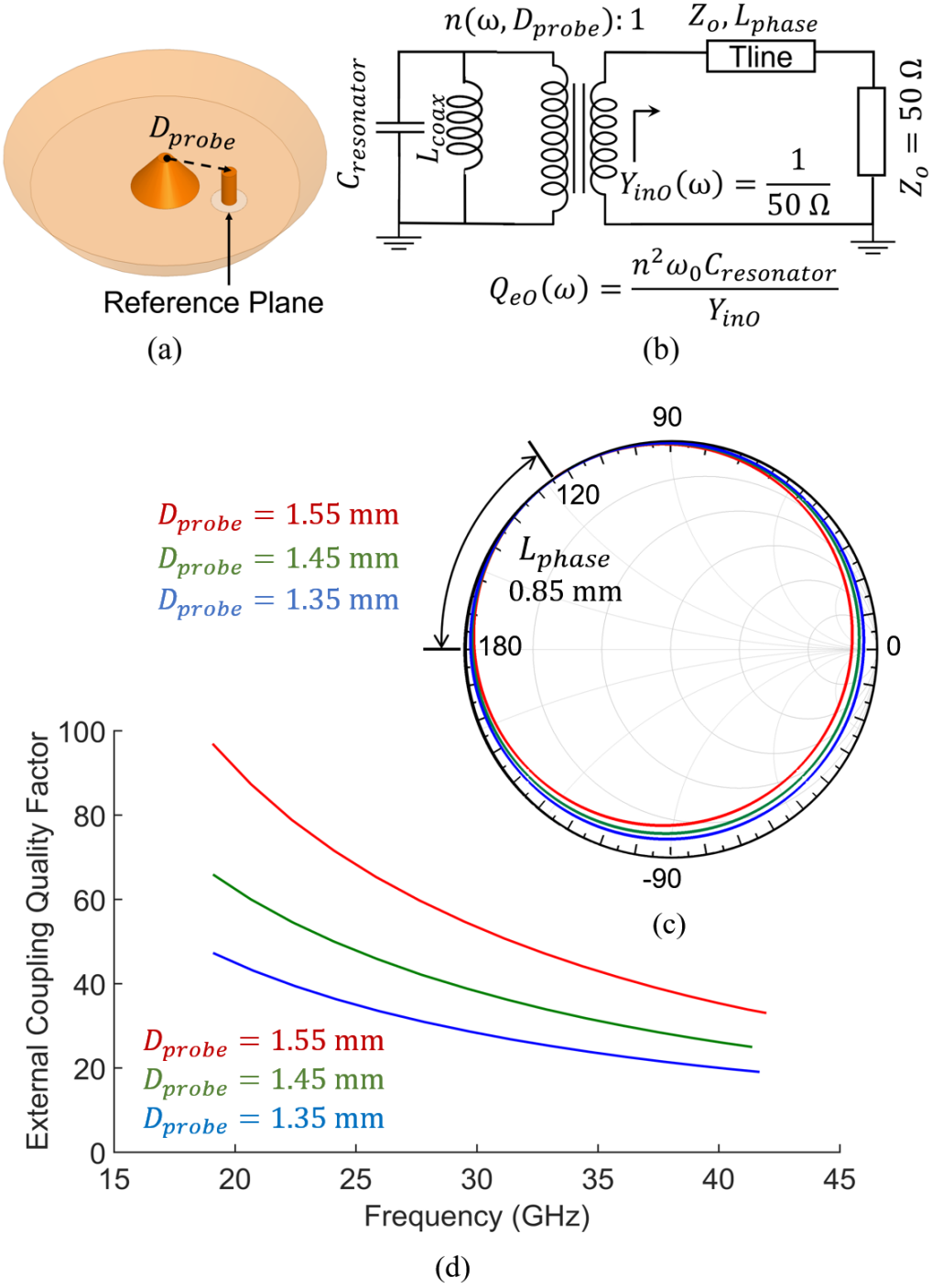

Fig. 3.11. (a) Basic probe-coupling scheme. (b) Equivalent circuit model. (c) Simulated reflection coefficient shown on the Smith chart for calculating L_{phase}. (d) Simulated external quality factor as a function of the probe position.

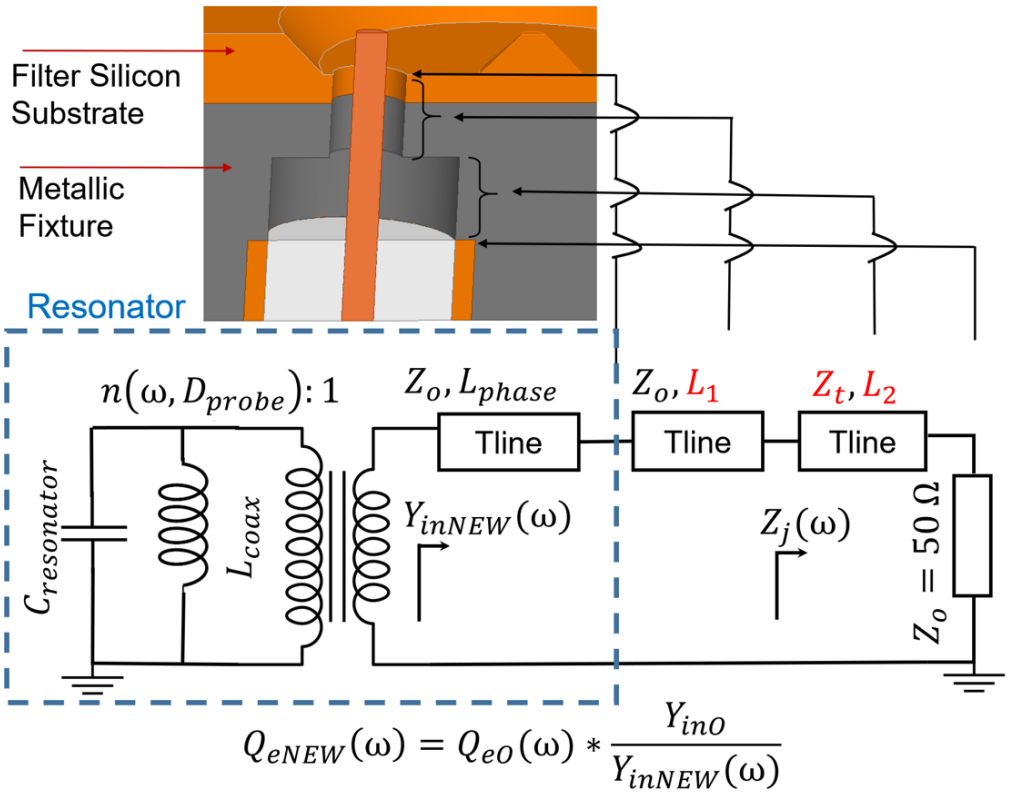

Fig. 3.12. External matching network structure and its circuit model.

Similarly to the inter-resonator coupling design, the frequency dependence of the external coupling is important for widely-tunable filters since it determines the available impedance matching. While active compensation is possible, it comes at the cost of additional loss and non-linearity. In this work we opt for passive compensation as shown in Fig. 3.12. This technique includes two transmission line sections with lengths L_1 and L_2 and impedances Z_0 and Z_t cascaded in series. This mechanism is explained below.

The original unmodified external quality factor without the two-line matching network in Fig. 3.11(b) can be calculated as $Q_{e0} = (n^2\omega C_{resonator})/Re(Y_{in0})$ where Y_{in0} —typically $\frac{1}{50\Omega}$ —is the input admittance shown in the figure. The effect of the two-line matching network can be understood by comparing the real parts of the input admittances

$$\frac{Q_{eNEW}}{Q_{e0}} = \frac{Re(Y_{in0})}{Re(Y_{inNEW})} \tag{3.20}$$

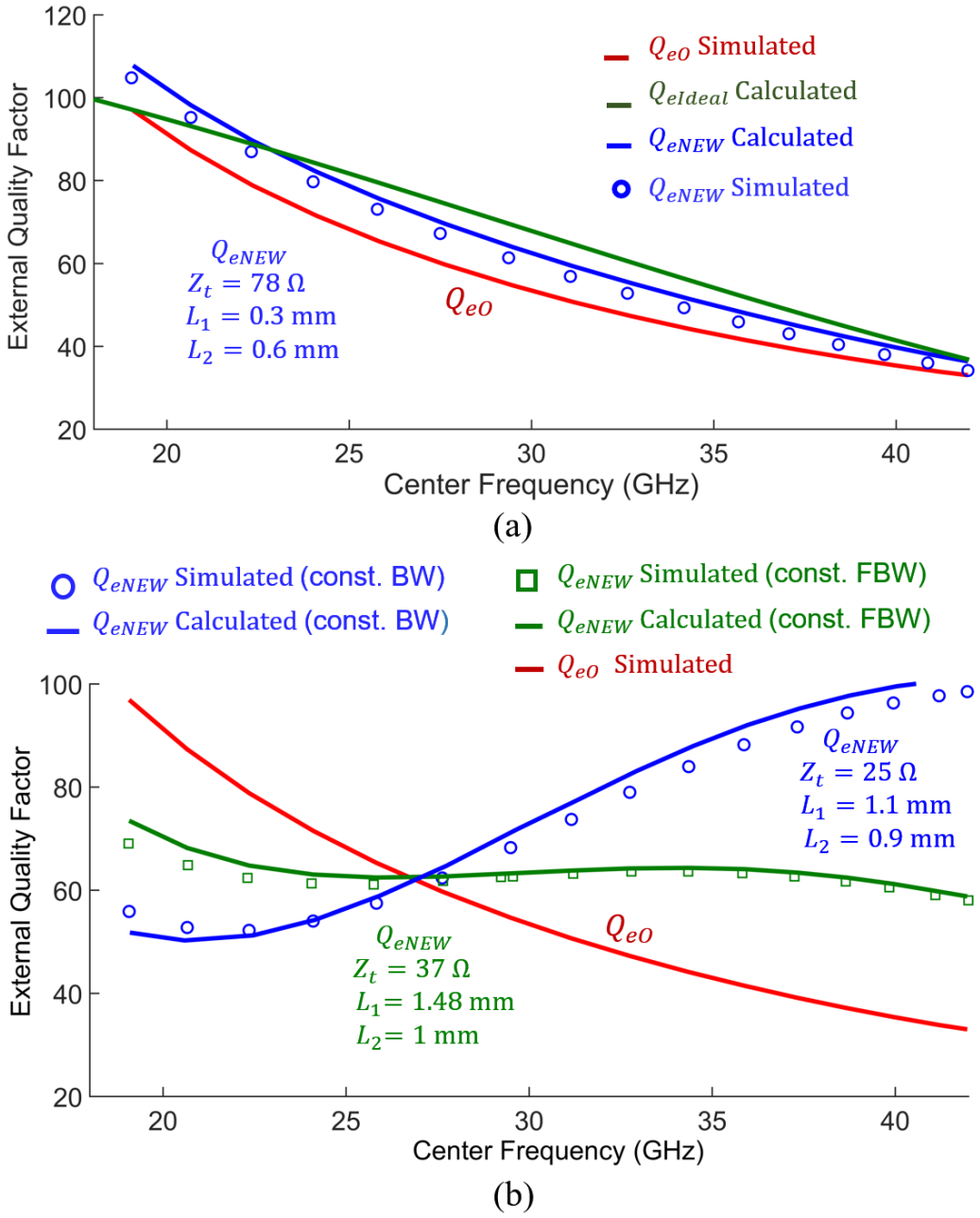

Fig. 3.13. (a) Example of external quality factor tailored by matching network. (b) Example of external coupling tailored by matching network for filter maintains FBW and absolute BW.

where Q_{eNEW} is the tailored external quality factor achieved with the addition of the two-line matching network. The ratio of Y_{in0} over Y_{inNEW} can be understood as a correction factor calculated as

$$\frac{1}{Y_{inNEW}} = Z_j \frac{Z_0 + jZ_j \tan(\beta(L_1 + L_{phase}))}{Z_j + jZ_0 \tan(\beta(L_1 + L_{phase}))} \tag{3.21}$$

where $Z_j = Z_0 \frac{Z_t + jZ_0 \tan(\beta L_2)}{Z_0 + jZ_t \tan(\beta L_2)}$ is the input impedance observed at the connection point between the lines and β is the propagation constant.

The main idea then is to design the two-line network so the external quality factor achieves its optimal value. This value is determined by perfect impedance matching over the entire tuning range. This requires an external quality factor equal to

$$Q_{eIdeal}(\omega) = \frac{1}{K_{ij}(\omega)} \frac{m_{ij}}{m_{si}^2} \tag{3.22}$$

in which, K_{ij} is pre-determined by the inter-resonator coupling design and m_{s1}, m_{ij} represent the needed de-normalized external and inter-resonator coupling coefficients respectively.

To realize an external quality factor as close as Q_{eIdeal} we can follow a two-step design process. First, vary D_{probe} until we achieve the best implementable probe position that makes Q_{e0} as close as possible to Q_{eIdeal}. Second, we choose the two-line section parameters to further tune the coupling coefficient until the obtained Q_{eNEW} becomes nearly equal to Q_{eIdeal}.

To illustrate this process with an example we design the external coupling of a two-pole filter with $m_{s1} = 0.78$, $m_{21} = 0.707$ as shown in Fig. 3.13(a). Here we have selected $K_{21}(\omega)$ to have the least frequency dispersion shown in Fig. 3.10 with the red curve. The calculated Q_{eIdeal} and the best possible Q_{e0} are shown in Fig. 3.13(a). The designed Q_{eNEW} approximates Q_{eIdeal} quite well with $Z_t = 78\ \Omega$, $L_1 = 0.3$ mm, and $L_2 = 0.6$ mm.

Furthermore, in Fig. 3.13(b) we demonstrate that the presented passive compensation scheme can successfully modify Q_{e0} to realize tunable filters with constant FBW or constant BW over an octave tuning range. This is achieved by appropriately selecting the dimensions of the two cascaded coaxial lines.

3.4 Overall Filter Design Flow

Fig. 3.16 graphically summarizes the overall filter design process discussed in detail in the previous sections. By following these design steps we obtain the main filter design parameters, i.e. Q_u, K, Q_e over the entire tuning range. Consequently, a frequency dependent N+2 coupling matrix m(ω) can be constructed and the scattering filter parameters can be

calculated using the method in [52]. Figure 3.14 graphically represents these for the designed filter along with the ones obtained by HFSS simulations. The calculated response is in very good agreement with the HFSS response further validating the presented approach.

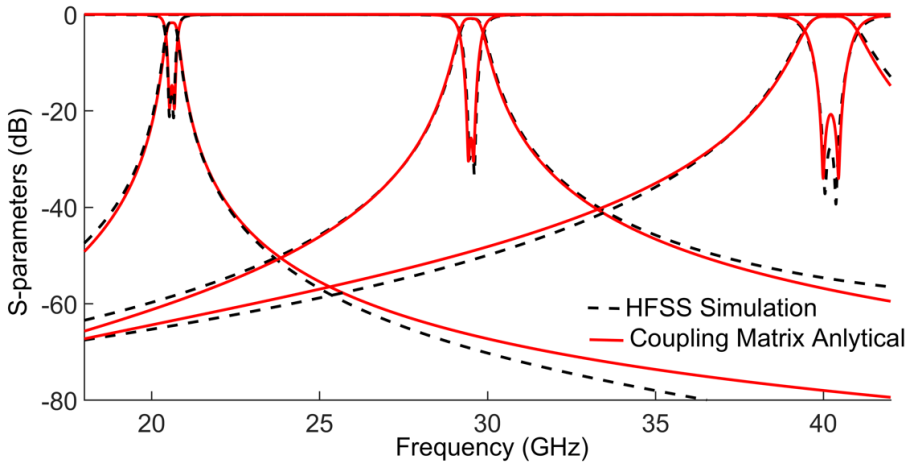

Fig. 3.14. Filter design, HFSS versus analytical coupling matrix theory.

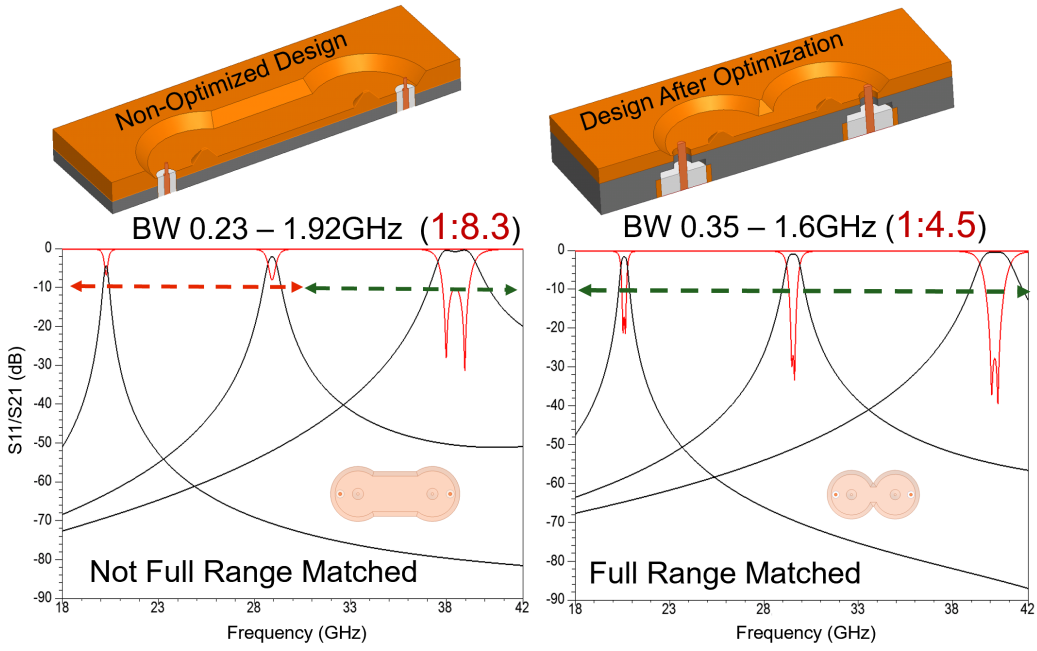

Fig. 3.15. Filter performance comparison: non-optimized versus optimized.

3.5 Implementation and Measurements

A two-pole all-silicon filter prototype was fabricated at the Birck Nanotechnology Center at Purdue University to experimentally validate the presented theory. The fabrication process described in [53] was employed. Filter prototypes with both pure Au and Au-V diaphragms were built. Figure 3.17(b)-(d) includes pictures of the fabricated MEMS diaphragm dies, filter cavity, and DC electrodes.

In addition to the individual fabrication steps, the final filter assembly is also conducted in the cleanroom. Prior to this assembly, an RCA clean is performed to remove particle-caused contamination. The critical assembly steps can be summarized as follows. First, we perform the die-to-die bonding of the filter cavity with the top ceiling wafer with special attention paid to the MEMS diaphgram-cavity post alignment. Second, the MEMS diaphragm is dry-etch released (Xenon Difluoride). The post-release RF gap can be determined by a laser conformal microscope through the back side DC biasing via hole. It is possible to finely adjust the initial RF gap by adding extra etching cycles to slightly change the post-release bending of the diaphragm. These techniques allow us to achieve the desired gap within about 0.2 μm. Third, we place the bonded MEMS die to the metal fixture shown in Fig. 3.17(e). This metal fixture was manufactured by CNC machining. Two miniaturized coaxial ports were inserted and soldered within the fixture body. The insertion depth of the coaxial port is well controlled by the fixture recess depth. Slight adjustments to center the coaxial pins were conducted under a microscope. The fourth and last step is to insert and bond the DC actuation electrodes over the MEMS diagrams.

Fig. 3.17 depicts the employed characterization setup. The S-parameters were measured using an Agilent E836lA vector network analyzer through a pair of coaxial connectors that are placed underneath the Au-metalized fixture. Each resonator is individually controlled by a separate DC bias voltage applied through a DC probe connected to a Keithley 2400 source-meter. Fig. 3.18 shows the measured filter performance for several bias states. The center frequency of the filter can be tuned between 20 to 40 GHz for an applied DC bias voltage between 0-180 V. This corresponds to an effective diaphragm deflection

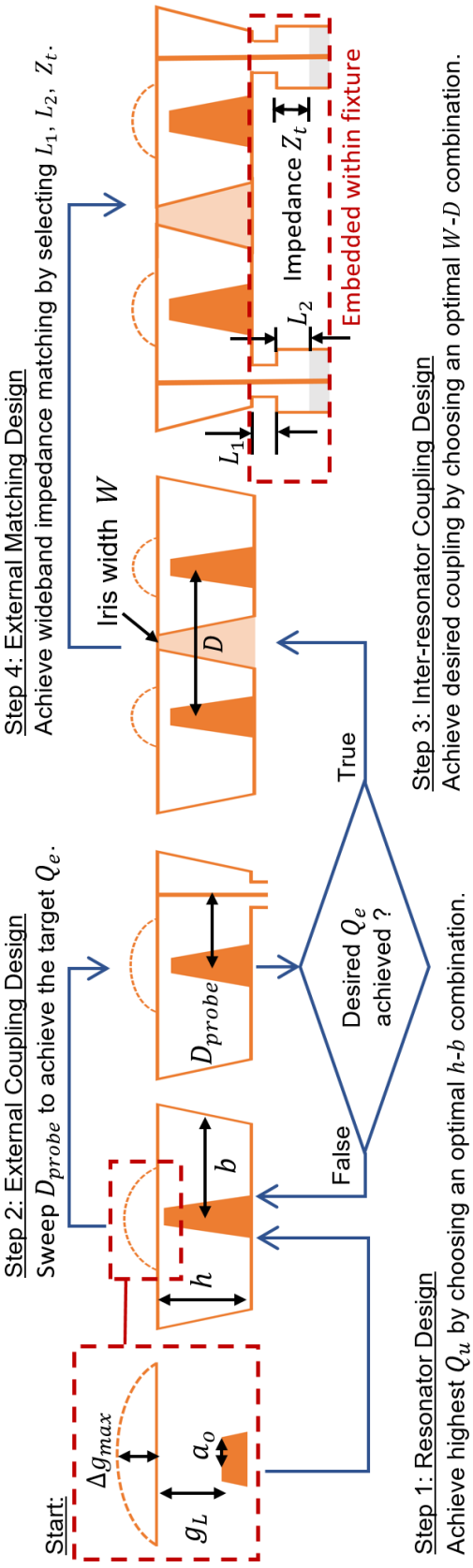

Fig. 3.16. Design and optimization flow of the EVA all silicon filter.

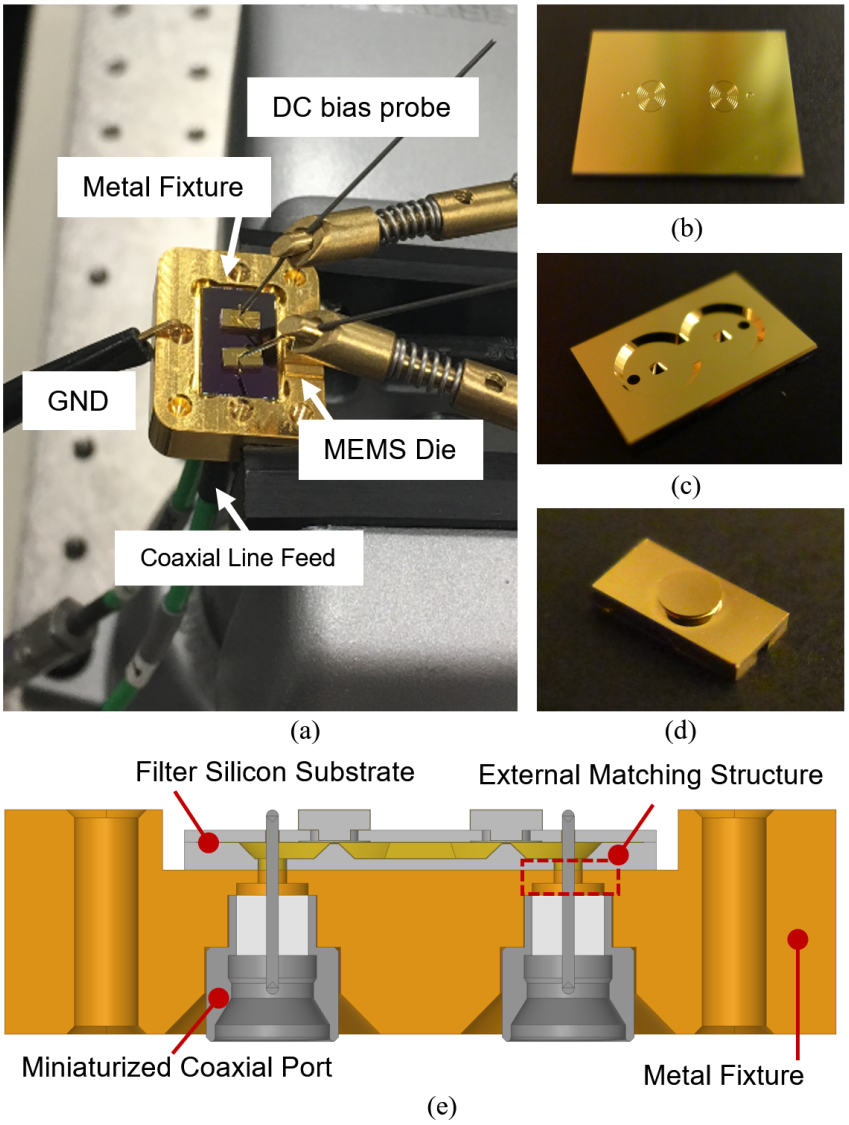

Fig. 3.17. (a) RF characterization setup of the two-resonator all-silicon BPF. (b) Front view of the manufactured die of the diaphragm. (c) Front view of the manufactured die of the cavity. (d) Side view of the manufactured die of the DC biasing electrode. (e) Cross-section view of the packaged device.

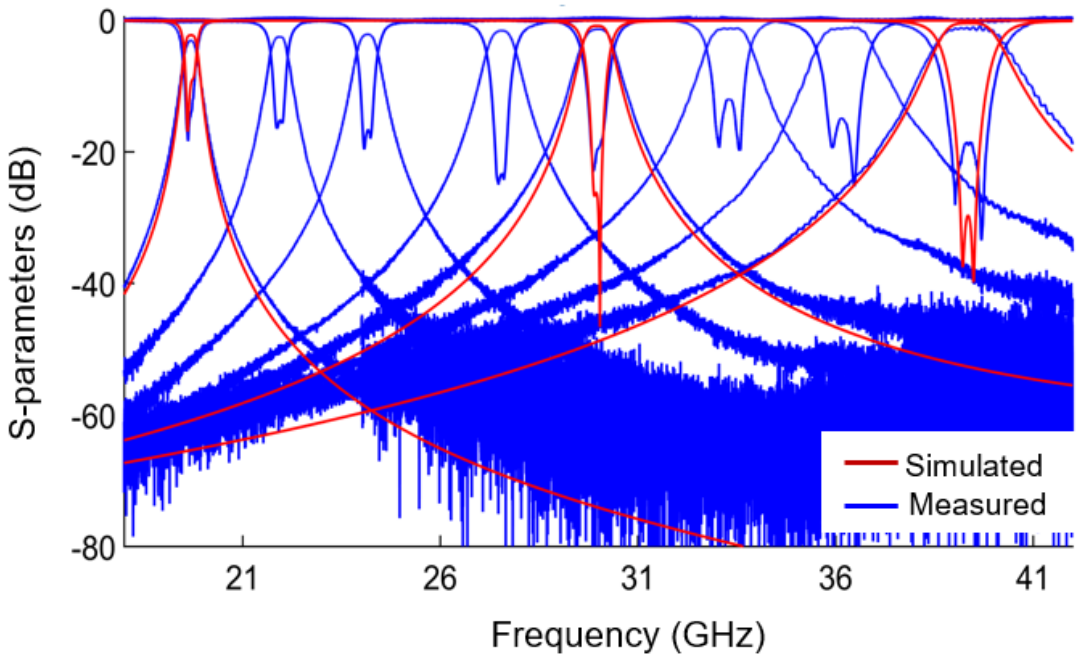

ω_o (GHz)	19.7	21.9	24.1	27.6	30	33.3	36.2	39.6
Voltage (V)	0	20	30	50	70	95	125	175
BW (GHz)	0.37	0.44	0.55	0.71	0.87	1.17	1.44	1.88
HFSS BW (GHz)	0.34				0.73			1.45
IL (dB)	3.09	2.58	2.15	1.63	1.37	1.26	1.14	1.07
HFSS IL (dB)	2.32				0.89			0.47

Fig. 3.18. Measured filter S-parameters and tuning performance over its 20-40 GHz tuning range.

of 17 μm. This was determined by fitting the measured RF response to the electromagnetic model. The measured insertion loss is less than 3 dB and the return loss is less than 15 dB. The fractional bandwidth was measured between 1.9% to 4.7% which is a bit larger than the calculated range (1.7% to 3.9%). This is attributed to the undercut of the wet etching that enlarged the width of the coupling iris. Considering the measured insertion loss and bandwidth we can estimate Q_u throughout the tuning range between 264 to 540.

3.6 Conclusions

This chapter reports on a detailed design technique for achieving optimal MEMS-tunable evanescent-mode cavity-based bandpass filters (BPFs) with continuously variable center frequency over an octave tuning range. The devised filters are manufactured using silicon-micromachining techniques that enable their actualization for frequencies located in the millimeter-wave (30-100 GHz) regime. For the first time we present an RF design methodology that takes into consideration all microfabrication-induced constrains—e.g. non-vertical wall profiles and finite MEMS deflection—and allows for high unloaded quality factor (Q_u) and minimum bandwidth (BW) variation to be achieved over the desired tuning range. A new fully passive input/output compensating structure integrated within the filter's package controls the filters external coupling and further enhances the filters performance.

A two pole 20-40 GHz tunable EVA filter is designed, optimized and experimentally demonstrated to validate the presented concepts. The fabricated filter incorporates electrostatically tuned micro-corrugated diaphragm (MCD) with enhanced tuning stability by co-sputtered Au-V material. Measurements demonstrated a tuning range between 20-40 GHz, relative bandwidth of 1.9%-4.7%, and impedance matching over the entire tuning range which is 22%, 1.9×, and 2× better than previously reported state-of-the-art MEMS tunable filters of this type [13].

3.7 Related Publications

- **Z. Yang**, D. Psychogiou, and D. Peroulis, "Design and optimization of tunable silicon-integrated evanescent-mode bandpass filters" *IEEE Tran. Microw. Theory Tech.*, vol. 66, no. 4, pp. 1790-1803, Jan. 2018.

4. ADVANCED MEMS TUNER DESIGN AND IMPLEMENTATION

4.1 Introduction

For all-silicon MEMS tunable EVA technology, the diaphragm is operated without contact, thus catastrophic failure requires severe negligence. However, non-ideal factors such as creep and stress relaxation affect the long-term filter tuning robustness. Although employing micro-corrugations and creep-resistive co-sputtered Au-V thin films [53] are effective in mitigating some creep effects, full recovery has not been accomplished yet.

Demonstrated in [54], utilizing feedback loop controlled bias voltages to actively compensate tuning error is a viable solution. The primary challenge for existing designs is due to the uni-directional nature of electrostatic MEMS actuators. Such uni-directional tuner can only be actuated away from its neutral position towards the DC electrode regardless of the actuation voltage polarity. Shown as Fig. 4.1(a), consequently the uni-directional mechanical stress leads to non-coverable creep that tends to slowly shift the tuners neutral position away from the cavitys center post. Such drift is non-compensable and leads, over time, to degradation of the tunability.

The ultimate solution for maintaining tunability is enabling bi-directional electrostatic tuning. Literatures [55, 56] reported successful demonstrations of bi-directional electrostatically actuated MEMS tuners on planar RF/microwave circuits. These designs require an additional electrode to enable bi-directional motion. However, such design remains challenging for 3-D cavities applications, because introducing an additional electrode within the resonator cavity complicates the MEMS structure and typically lead to significant degradation of RF performance.

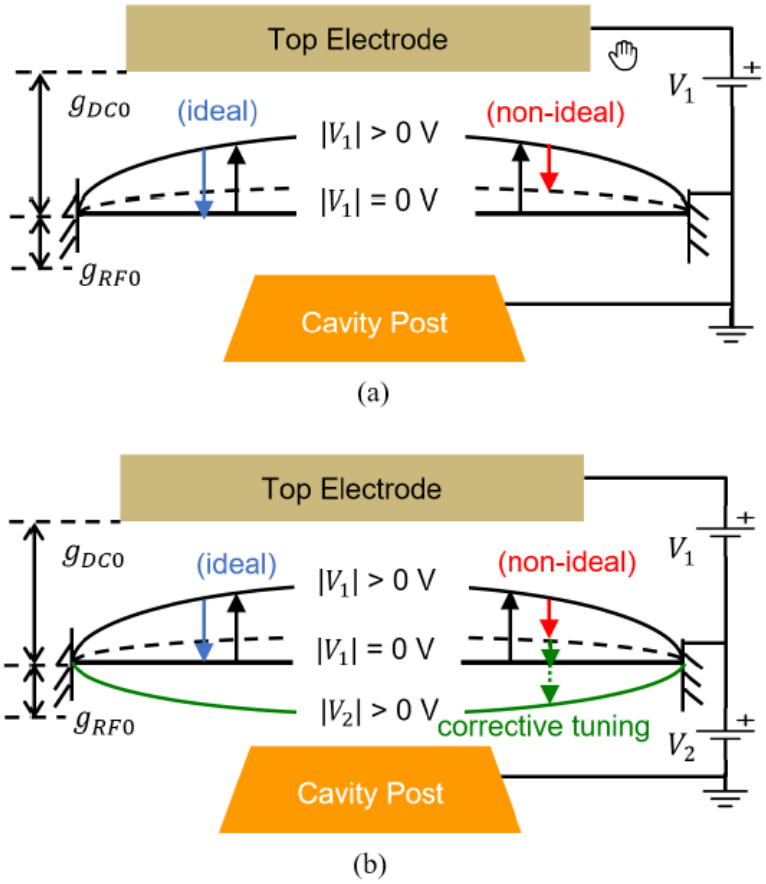

Fig. 4.1. (a) Uni-directional tuning, (b) Bi-directional tuning.

4.2 Design

Fig. 4.1 depicts the main idea of the proposed design. Similar to conventional uni-directional designs, a post-loaded cavity is tuned by a flexible diaphragm that is suspended above the cavity post. Displacements in the order of 5–30 μm typically yield octave K-band tuning performance. Such a displacement is induced by biasing the flexible diaphragm against a bias electrode above it. This electrode is outside the RF cavity and does not interact with its resonant field.

However, unlike with uni-directional designs, the center post in the bi-directional design cavity is DC biased against the tuning membrane. While this needed voltage is small (typically 2-3 V), it is critical for implementing the needed corrective tuning, as explained

below. It is for this reason that the MEMS tuner needs to be isolated from the rest of the cavity. As Section 4.2.1 shows, this is realized by the novel MOM sealing technique.

4.2.1 MOM-sealed Cavity Resonator Design

Fig. 4.2(b) depicts the proposed EVA resonator structure. Here, there is a MOM sealing structure formed on the silicon die flat boundary area by a thin dielectric bonding layer with a thickness of H_d. This layer does not disturb the electromagnetic (EM) fields within the cavity. At the fundamental mode, the electromagnetic wave propagates into the MOM seal

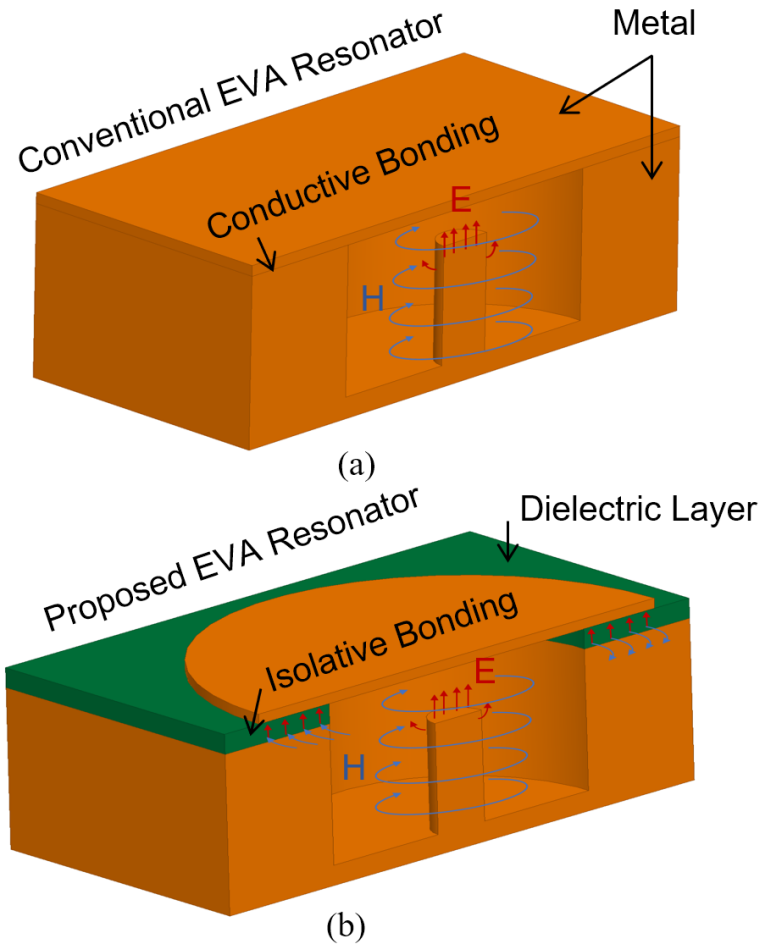

Fig. 4.2. (a) Conventional EVA resonator, (b) Proposed EVA resonator

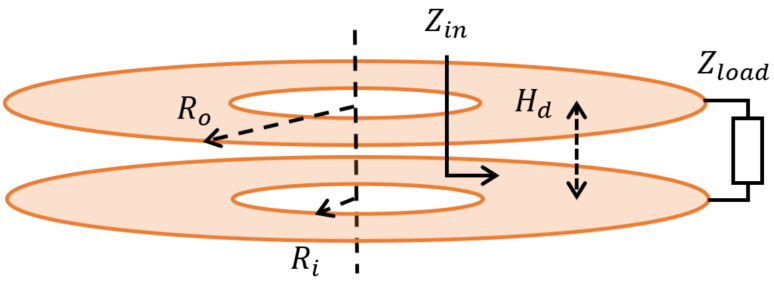

Fig. 4.3. Radial transmission line model.

in radial direction. Such a structure essentially becomes a radial transmission line whose TEM mode is excited. According to [57], if the radial line is terminated with ideal open $R_L = \infty$ at the conductor outer edge shown in Fig. 4.3(a), the input impedance Z_{in} at the inner radius R_i, looking outward into the radial line is derived as (4.1):

$$Z_{in} = -jZ_o(R_i)\cot(kR_i, kR_o) \tag{4.1}$$

in which

$$Z_o(R_i) = \frac{60H_d}{R_i\sqrt{\epsilon_r}} \tag{4.2}$$

is the characteristic impedance at the inner-radius of the radial line. ϵ_r is the relative permittivity of the dielectric. $\cot(kR_i, kR_o)$ is the radial cotangent function:

$$\cot(kR_i, kR_o) = \frac{N_0(kR_i)J_1(kR_o) - J_0(kR_i)N_1(kR_o)}{J_1(kR_i)N_1(kR_o) - N_1(kR_i)J_1(kR_o)} \tag{4.3}$$

in which $J_m(x)$ is the Bessel function of the first kind of order m and argument x and $N_m(x)$ is the Bessel function of the second kind of order m and argument x. Both conduction and dielectric loss are accounted for by assuming a complex propagation constant k [57]:

$$k = \beta + j\alpha. \tag{4.4}$$

β is phase constant. When loss is small can be calculated as:

$$\beta = \frac{2\pi\sqrt{\epsilon_r}}{\lambda_0} \tag{4.5}$$

α is attenuation constant:

$$\alpha = (R_s\sqrt{\epsilon_r})/120\pi + \frac{\beta}{2}\tan(\delta) \tag{4.6}$$

in which R_s and $\tan(\delta)$ are the conductor surface resistivity and dielectric loss tangent respectively.

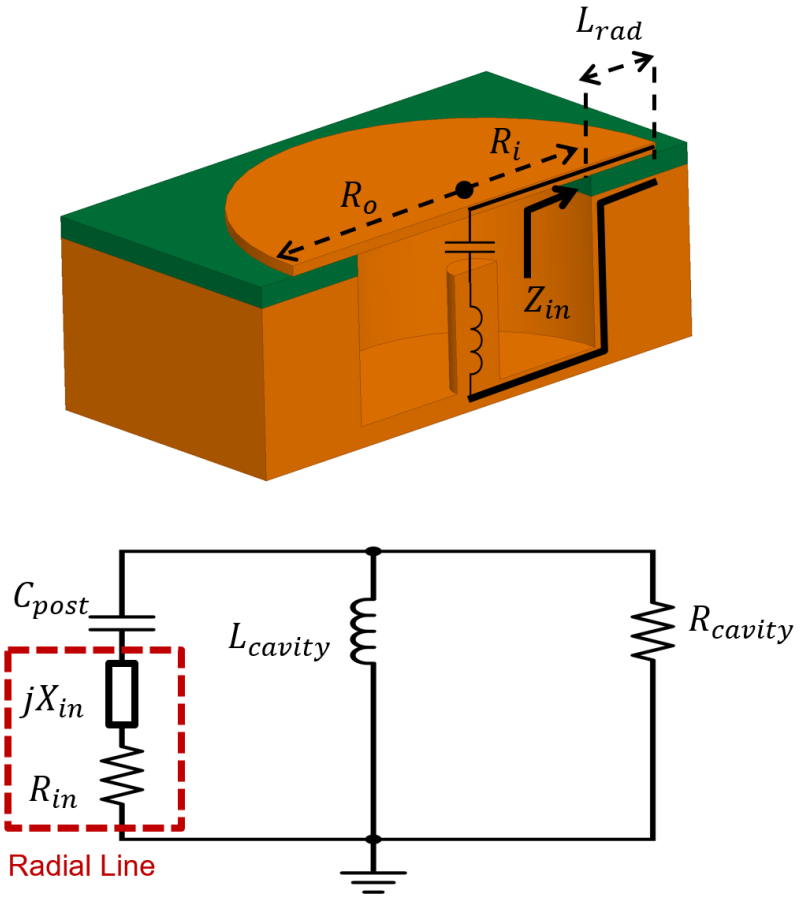

Fig. 4.4. Equivalent circuit model of bi-directional tunable resonator.

According to Fig. 4.4, Z_{in} is in series with C_{post} and in parallel with L_{cavity}. As such, the input reactance X_{in} shifts the resonance frequency and the input resistance R_{in} degrades the quality factor significantly. Thus, the design goal is to minimize X_{in} and R_{in}, in order to enable bi-directional tunability without compromising performance or complicating design flow.

According to eqns. (4.1)–(4.6), X_{in} and R_{in} are functions of R_i, L_{rad}, H_d, $\tan(\alpha)$, and ϵ_r. The resonator design fixes R_i and the selection of dielectric material sets ϵ_r and $\tan(\alpha)$.

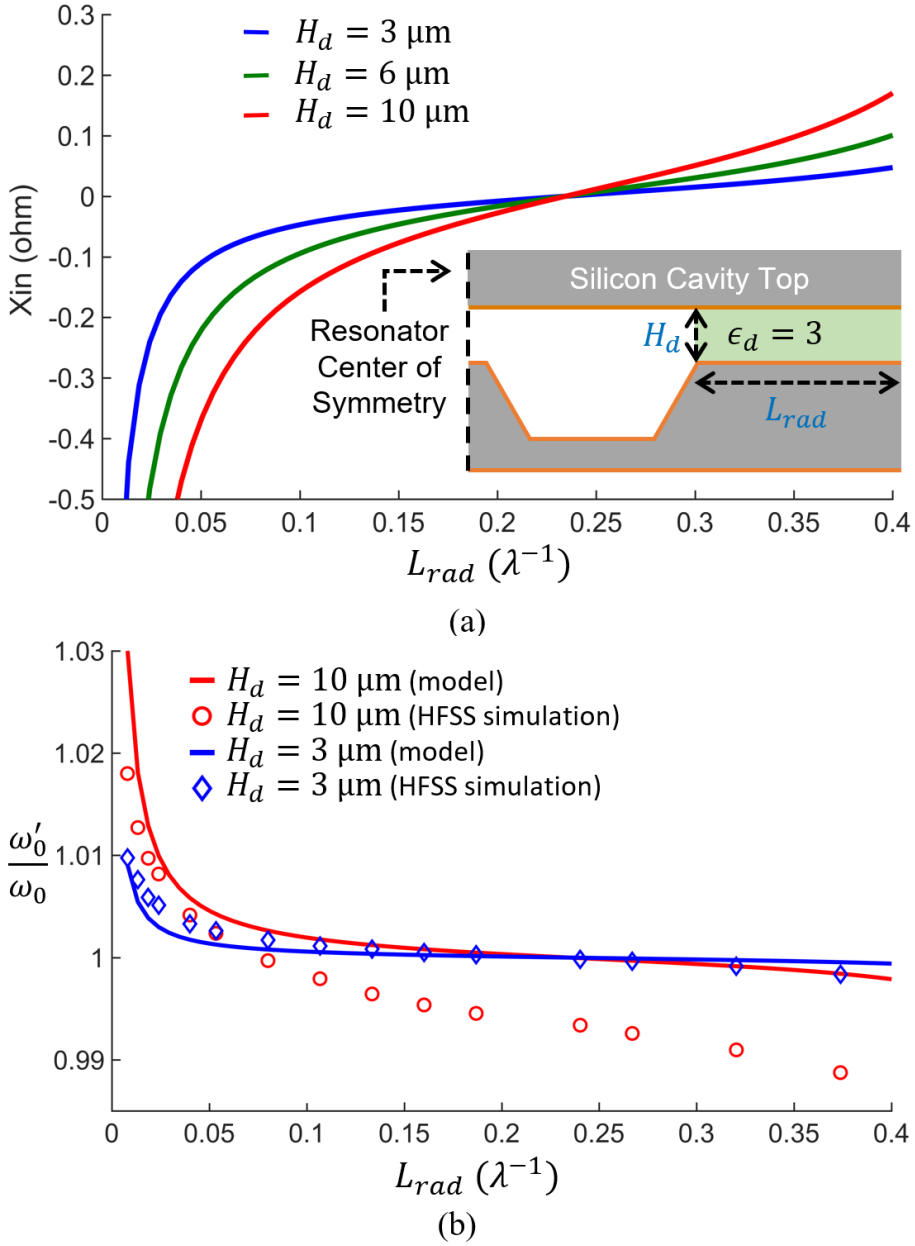

Fig. 4.5. (a) Input suseptance versus L_{rad} , (b) Frequency shift versus L_{rad}.

H_d and L_{rad} remain as the two major design parameters. Practical values of H_d for the proposed technology range from a few to tens of μm while L_{rad} is less restricted.

For illustration and comparison, this work presents a design example for enabling bi-directional tunability on an all-silicon EVA tunable filter reported in [58] whose R_i equals 2.4 mm and whose frequency tuning ranges from 20 to 40 GHz. The analysis is performed at its highest tuned frequency (40 GHz) and then generalized by normalizing the design parameters to wavelength. Fig. 4.5(a) correlates the resulted X_{in} with variations of H_d and L_{rad}. The model shows X_{in} can be either capacitive or inductive and is minimized when L_{rad} is a quarter wavelength. The X_{in}-induced resonance frequency shift can be quantified as:

$$\frac{\omega_o'}{\omega_o} = \sqrt{1 + \frac{C_{post}}{C_{in}}} \tag{4.7}$$

in which ω_o' is the shifted resonance frequency after the radial line is introduced and ω_o is the intrinsic resonance frequency. C_{in} is an equivalent capacitance calculated as $C_{in} = -1/(\omega X_{in})$, which is negative in the inductive region. For a typical EVA tunable resonator design, C_{post} is far larger than C_{in}. As such, the frequency shift is negligible (less than a few percent), as is shown in Fig. 4.5(b) for this example.

The insertion loss of the MOM sealing is due to conduction loss R_{inc} and dielectric loss R_{ind} which can be quantified by setting $\tan(\delta)$ and R_s equal to 0, respectively. From Fig. 4.6(a), it should be noted that dielectric loss contributes less when H_c is smaller than $10\mu m$. This broadens the options of which dielectric bonding materials can be utilized based on the application needs. The following equations quantify the impact to the quality factor Q_{uNew}:

$$\frac{Q_{uNew}}{Q_{u0}} = \frac{R_{new}}{R_{res}} \tag{4.8}$$

in which $R_{new} = R_{in} \parallel R_{res}$.

Fig. 4.6(b) summarizes the Q_u impact for different H_d and L_{rad}. It shows good agreement between the analytical model and full wave simulation, though there is a maximum discrepancy of 10-20%. This error results from the neglect of fringing effects, higher order modes, and non-ideal open terminations in the model.

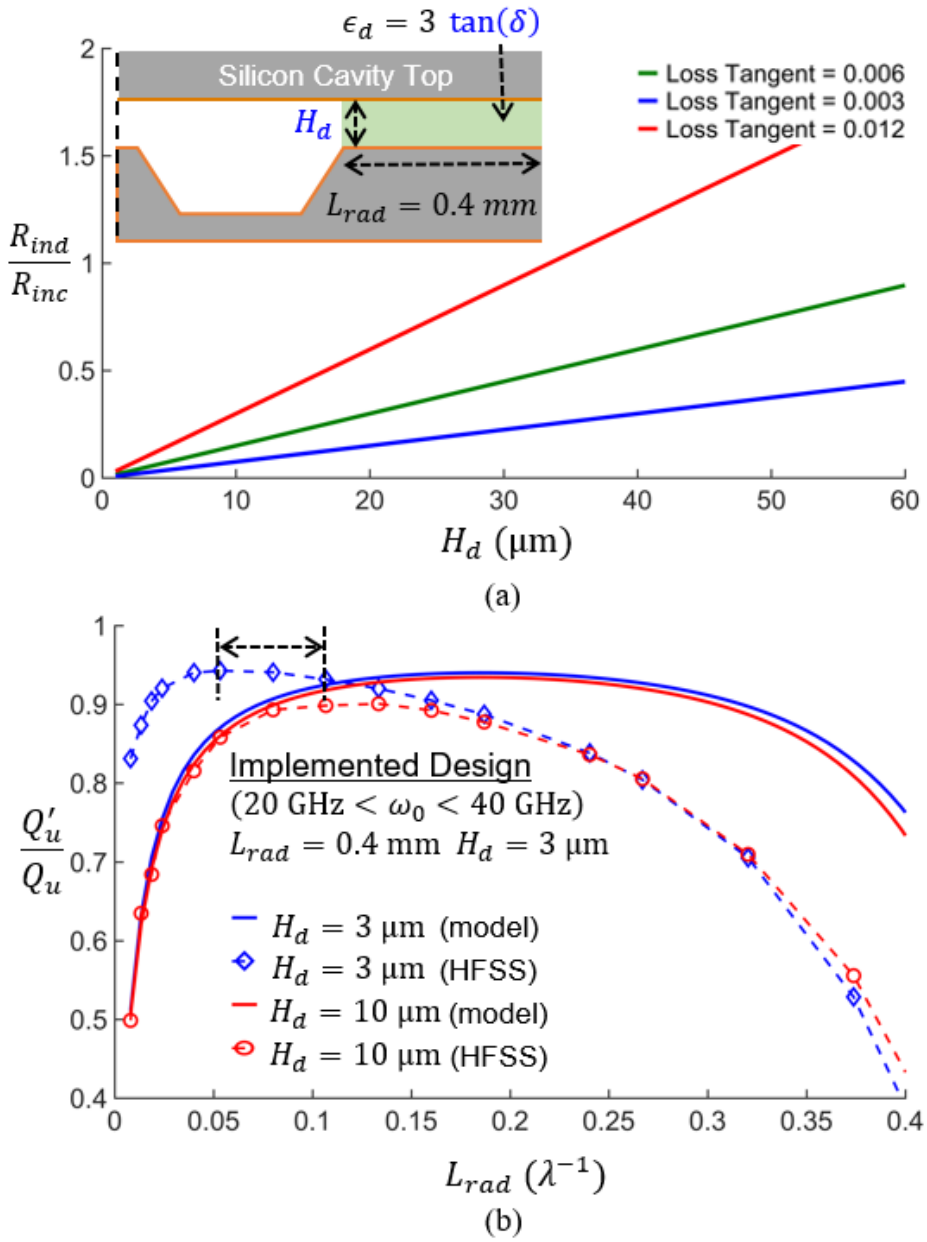

Fig. 4.6. (a) Resistive part of the input impedance, (b) ratio of the conductive loss and the dielectric loss.

It should be noted that a thinner dielectric layer is preferred and that there exists an optimal L_{rad} at about 0.1λ (0.4 mm) for which Q_u is maximized. This matches expectation since L_{rad} needs to be large enough to support return current, but not so large as to create excessive conduction loss from the resultant standing wave on the radial line.

It is essential to see that there is only a 5% difference between an optimized bi-directional tuned resonator implementation and the uni-directional tuned resonators for the filter reported in [58]. The reason is that the resistive loss due to conventional bonding is compara-

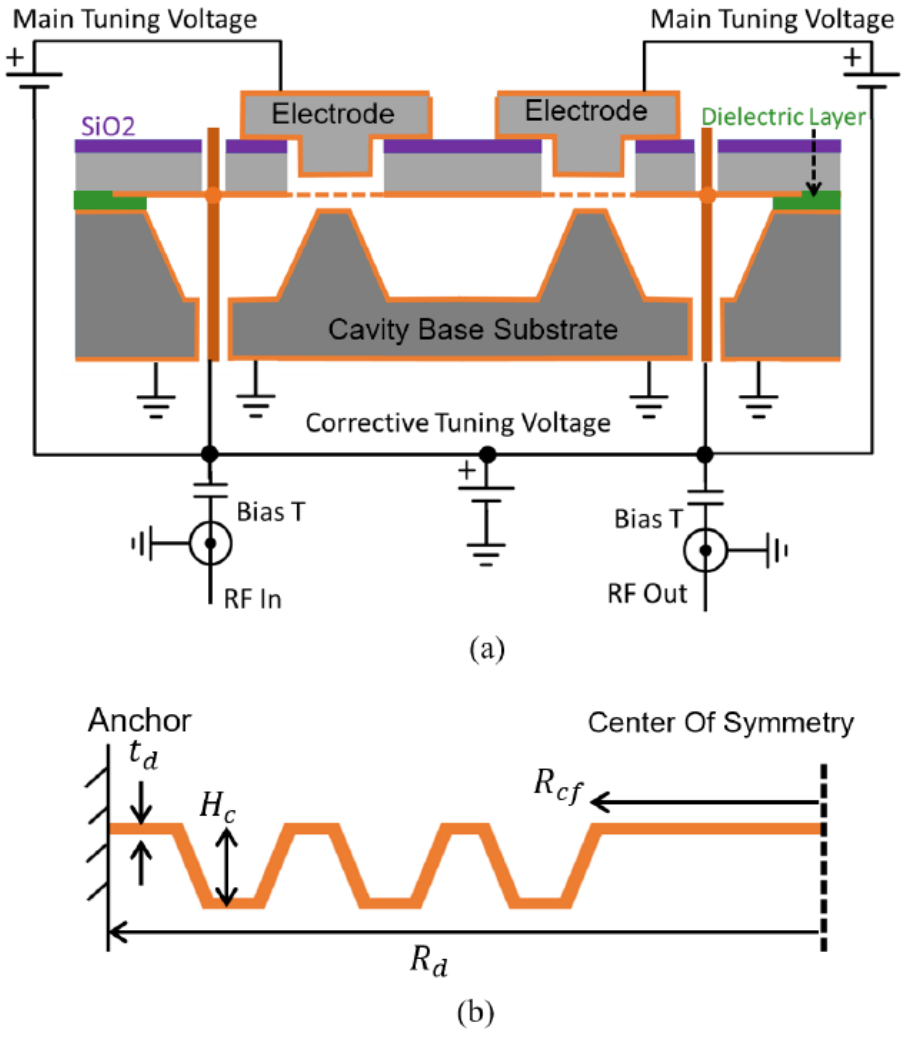

Fig. 4.7. (a) Conceptual draw of the filter, (b) Cross-section of the corrugated diaphragm.

ble to the MOM seal. To this end, it is demonstrated that implementing such bi-directional tuning does not negatively impact RF performance.

4.2.2 Bi-directional MEMS Tuner Design

Fig. 4.7 shows the conceptual drawing of the MEMS tuner design. In the main tuning mode, since the top electrode radius is comparable to R_d and far larger than g_{DC0}, it is reasonable to approximate the loading on the diaphragm as uniformly distributed pressure P_m. According to [59], the induced MCD center deflection Δg can be calculated as:

$$P_m = \frac{4t_d}{R_d^2}\left(\sigma_{eff} + A_p\frac{E_d t_d^2}{4R_d^2}\right)\Delta g + \left(B_p\frac{E_d t_d}{R_d^4}\right)\Delta g^3 \tag{4.9}$$

in which E_d, ν, t_d, R_d are Young's modulus, Poisson ratio, diaphragm thickness, and diaphragm radius respectively. σ_{eff} is the effective intrinsic stress:

$$\sigma_{eff} = \frac{\sigma_o}{1 + 3\left(\frac{H_c}{t_d}\right)^2\left(\frac{R_d - R_{cf}}{2R_{cf}}\right)} \tag{4.10}$$

in which, σ_o, H_c, R_{cf} represent, intrinsic stress of the metallic film, corrugation height, and diaphragm center flat area radius. A_p and B_p in (4.9) are dimensionless coefficient of the linear and nonlinear tension terms respectively:

$$A_p = \frac{2(q+1)(q+3)}{3\left(1 - \frac{\nu^2}{q^2}\right)} \tag{4.11}$$

$$B_p = 32\left(\frac{1}{q^2 - 9}\right)\left(\frac{1}{6} - \frac{3 - \nu}{(q - \nu)(q + 3)}\right) \tag{4.12}$$

q is a profile factor whose squared value is the ratio of corrugation rigidity with respect to bending in tangential and radial directions:

$$q^2 = \frac{R_d + 2N_c H_c}{R_d}\left(1 + 1.5\left(\frac{H_c}{t_d}\right)^2\right) \tag{4.13}$$

in which N_c is the corrugation number.

In correction actuation mode, since R_{post} is much smaller than R_d, the loading is a concentric force F_c on the diaphragm center. In this case, (4.9) is modified to:

$$F_c = \left(\frac{4t_d}{R_d^2}\left(\sigma_{eff} + A_p\frac{E_d t_d^2}{4R_d^2}\right)\Delta g + \left(B_p\frac{E_d t_d}{R_d^4}\right)\Delta g^3\right)A_e \tag{4.14}$$

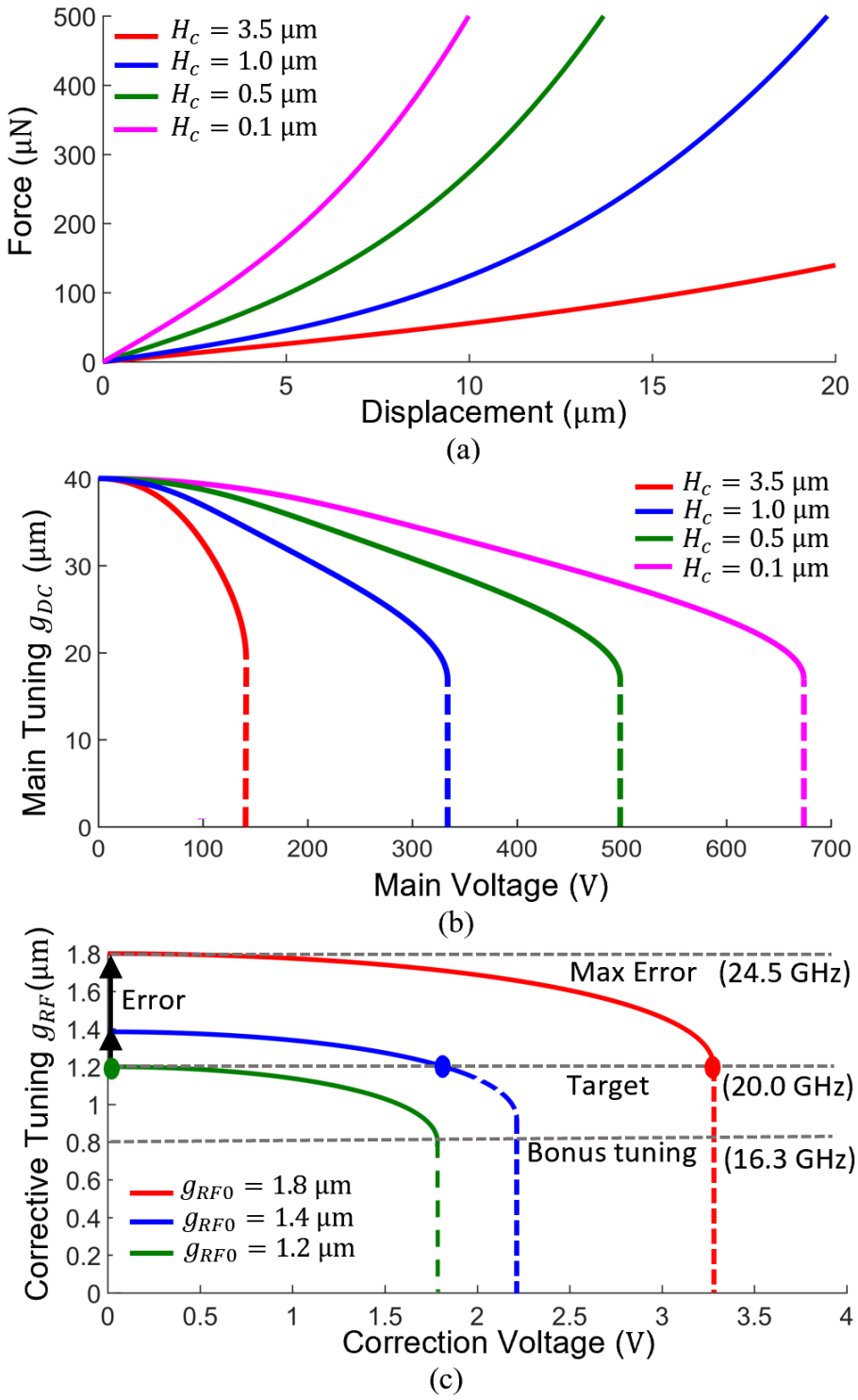

Fig. 4.8. (a) Tuning range versus H_c, (b) Pull-down voltage of the main tuning versus H_c, (c) Pull down voltage for the corrective tuning versus H_c.

in which A_e is the effective area:

$$A_e = \frac{(1+q)}{2(3+q)}\pi R_d^2. \tag{4.15}$$

As seen from the above analytical equations, a larger R_d reduces bending rigidity for lower actuation voltage as well as the stress for less creep. In this work, without losing generality, an R_d value of 0.9 mm is set as the largest allowed value restricted by the cavity design. A thinner t_d is more cost-effective and preferable to mitigate the high tuning voltage. Nevertheless, the metallic diaphragm is part of the cavity top ceiling conductor and is required to be thicker than the RF skin depth of the lowest tuned frequency. As such, the t_d in this work equals 1 μm as a result of balancing the trade-offs above. Low σ_o is preferable, however it remains a challenge to achieve with excellent uniformity over the wafer. In this work, with careful stress control, the fabrication resulted in intrinsic tensile stress values ranging from 0 to 45 MPa

H_c, which is less limited and can be accurately controlled during manufacturing, remains the main design parameter. Fig. 4.8(a) demonstrates its significance. H_c tailors diaphragm rigidity and is directly proportional to actuation linearity. As such, the actuation force required to actuate the diaphragm center by 15 μm reduces 8× when H_c is increased from 0.1 to 3.5 μm.

To further quantify the actuation performance, main tuning electro-static pressure P_m is approximated by the parallel plates model:

$$P_m = \frac{\epsilon_0 V^2}{2\left(g_{DC0} - \Delta g\right)^2} \tag{4.16}$$

while the corrective concentric force can be calculated as:

$$F_c = \frac{(\pi R_{post}^2)\epsilon_0 V^2}{2\left(g_{RF0} - \Delta g\right)^2} \tag{4.17}$$

The solution of equating (4.9), (4.16) and (4.14), (4.17) describes the voltage-deflection curves of main and corrective tuning respectively. Assuming g_{DC0} is 40 μm, Fig. 4.9(b) shows increasing the corrugation height from 0.1 μm to 3.5 μm reduces the main actuation voltage from nearly 600 V down to 120 V.

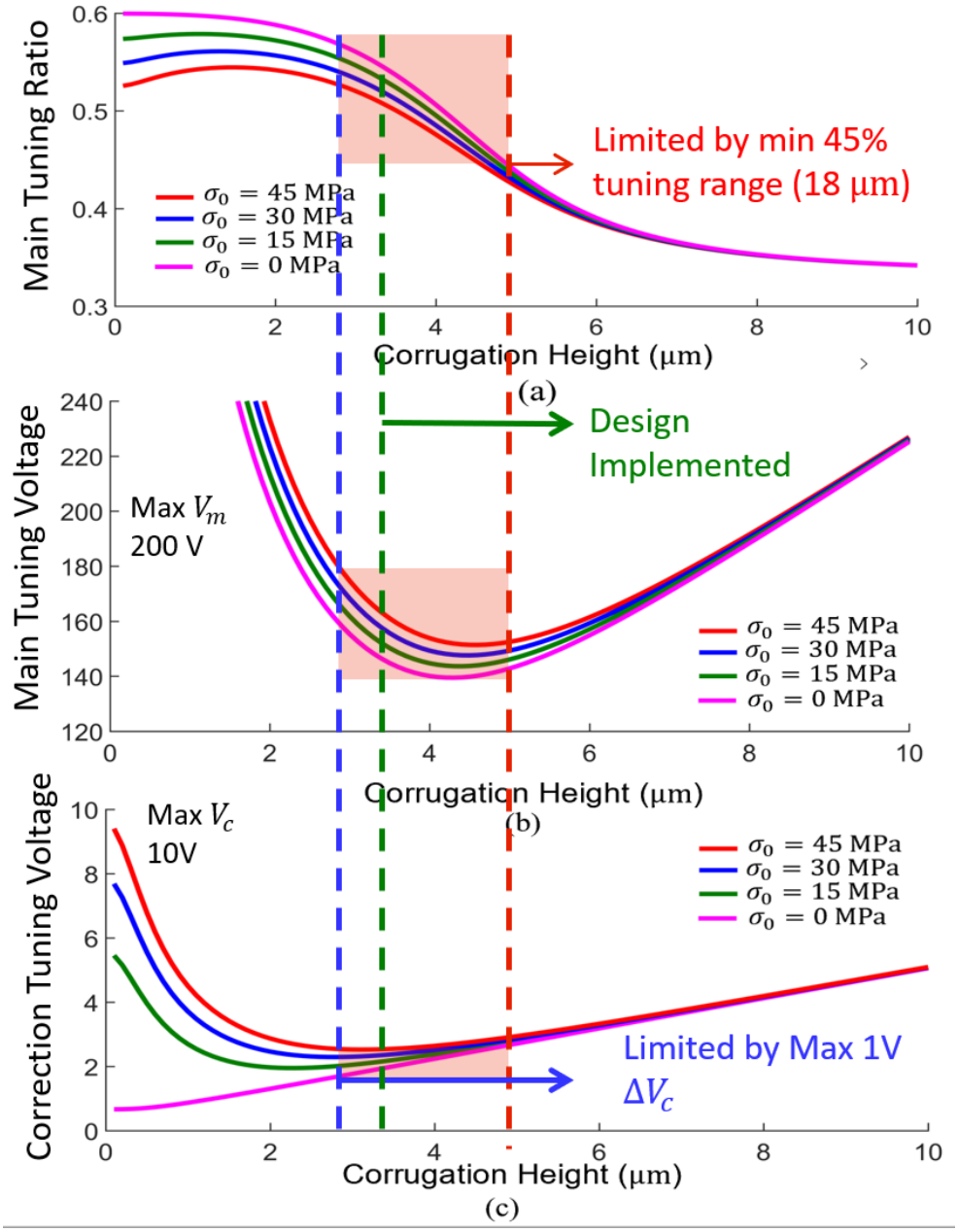

Fig. 4.9. (a) Tuning range versus H_c, when g_{DC0} = 40 μm (b) Pull-down voltage of the main tuning versus H_c, (c) Pull down voltage for the corrective tuning versus H_c.

.

Fig. 4.8(c) shows the voltage-deflection tuning curve for corrective tuning. This assumes g_{RF0} is initially at the desired 1.2 μm then drifts to a higher position over time or operation cycles. The corrective bending operates at the quasi-linear region of the force-displacement curve. The maximum correctable creep-induced error is up to 33% of g_{RF0}, which translates into a 22% drift of the initial unbiased frequency f_0. Such a level of correction is sufficient for the typically measured frequency drift, which is less than 10%.

Fig. 4.9 sheds more light on the MCD design strategies. Increasing H_c suppresses both the third order term and a portion of the linear term—σ_{eff}. Shallow corrugations (H_c less than 3.5 μm here), significantly reduces the main tuning voltage while maintaining a similar tuning range. Further, deeper H_c enhances bending linearity and suppresses tuning voltage variation at the cost of tuning range reduction.

It is critical to see from Fig. 4.9(c) that corrugations are necessary for corrective tuning. Otherwise, the result is a low yield design whose control voltage is sensitive to the intrinsic stress. On the other hand, since g_{RF0} is typically more than 10× smaller than g_{DC0}, a low voltage is capable of making effective corrective tuning, fulfilling the prerequisite in the sense that a thin layer of dielectric can hold such voltage without breakdown.

4.2.3 RF-MEMS Co-design Flow

The overall RF-MEMS co-design process is summarized in the following steps:

Step 1: Based on the required g_{RF0}, choose an H_d value that is as thin as possible but thicker than g_{RF0} to offset non-ideal assembly effects. In this example, g_{RF0} is 1.4 μm, and H_d is selected to be 3 μm.

Step 2: Perform the RF analysis and locate the optimized *Lrad* value for maintaining highest possible Q_u. Fig. 4.6(b) shows that the optimized *Lrad* equals 0.4 mm for this example.

Step 3: Choose a g_{DC0} value such that the targeted maximum diaphragm deflection g_{RFmax} is around 45% g_{DC0}. For the targeted 18 μm tuning in this work, g_{DC0} equals 40 μm

Step 4: Determine the limitation of bias voltages. In this case, V_c must be less than 10 V to prevent thin dielectric break down, and the required control circuit variation for the corrective pull-down voltage must be less than 1 V. The maximum main tuning voltage is 200 V.

Step 5: Based on the given t_d, R_d, and g_{RF0} values, complete a MEMS analysis like the one shown in Fig. 4.9. Here, fulfilling the prerequisite tuning ratio of 45% requires H_c to be less than 5 μm. The maximum tolerable variation of the correction pull-down voltage demands that H_c must be deeper than 3 μm. Both the main and corrective tuning voltages are not the limiting factors in this case.

Step 6: Choose an optimal H_c within the allowable range. In this case H_c = 4 μm results in a minimal tuning voltage and H_c = 3 μm results in a maximized tuning range. In this work, H_c = 3.5 μm is selected as a balanced option.

4.3 Fabrication and Assembly

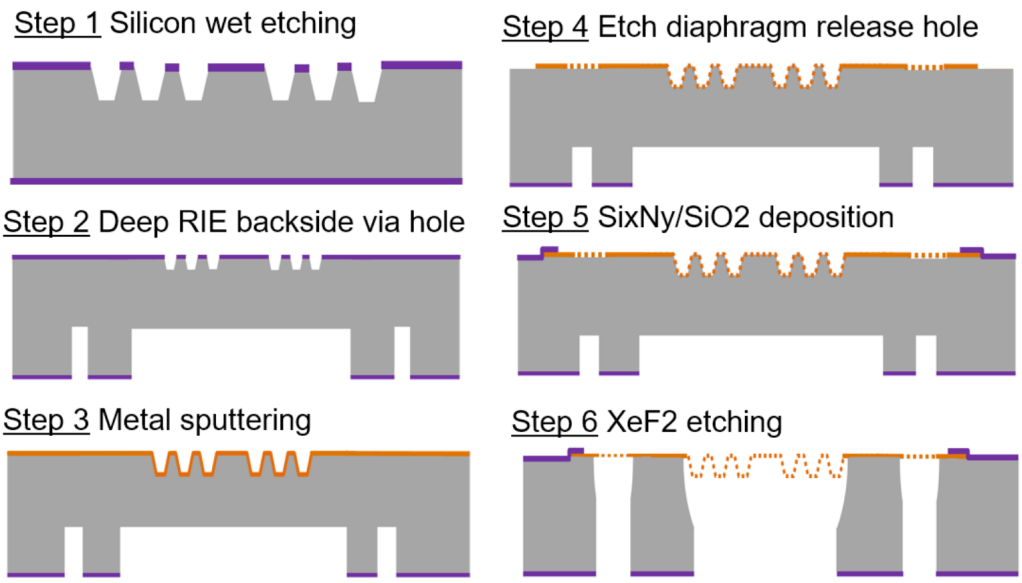

Fig. 4.10. Updated diaphragm fabrication flow enabling bi-directional tuning.

Fig.4.10 summarizes the fabrication flow of the MEMS diaphragm die. Comparing to the uni-directional tuner reported in Chapter II, enabling bi-directional tunability costs only one additional mask (deposition and patterning of the silicon dioxide layer).

Fig. 4.12 shows the conceptual assembly process. The authors conducted all of the fabrication and assembly process with university facilities. Fig. 4.13(a)-(e) summarizes the fabrication results.

The first step uses a wafer or die to align the cavity posts with the centers of the diaphragm. Afterward, a thin layer of polymethyl methacrylate (PMMA) is dropped on the boundary surface of the cavity dies, timely bringing the two pieces in contact with pressure. The device is then heated to 120 °C for 60 seconds before being slowly cooled down to room temperature to build solid bonding between the two silicon dies. The cured PMMA layer acts as an adhesion agent as well as the MOM seal insulator. The contact pressure is characterized so that the overall thickness of the dielectric layer is about 3 μm.

In the second step, the diaphragm is released by placing the bonded dies into a xenon di-fluoride silicon etching chamber, removing the sacrificial silicon layer and enabling a quality assurance check of the RF gap g_{RF0} through the diaphragm backside via hole shown in Fig. 4.13(c)

The third step, similar to the first step, is to bond the silicon die into the metal package. Two coaxial port center pins penetrate the small diaphragm on the silicon top ceiling covering the via holes. The remaining broken small diaphragm seals the cavity, as shown in Fig 4.13(d), and proves to be a reliable DC connection. Furthermore, such a design provides good mechanical isolation from external vibration and thermal expansion. The last step is to bond the top electrodes with the same PMMA adhesion technique and then wire bond them to the daughter board on the package.

Fig. 4.11(b) depicts a detailed cross-section view after assembly. Compared to the current state-of-the-art uni-directional tuner fabrication flow reported in [13], the proposed design costs only one additional mask (deposition and patterning of the silicon dioxide layer). On the other hand, using PMMA adhesion bonding rather than Au-Au thermal

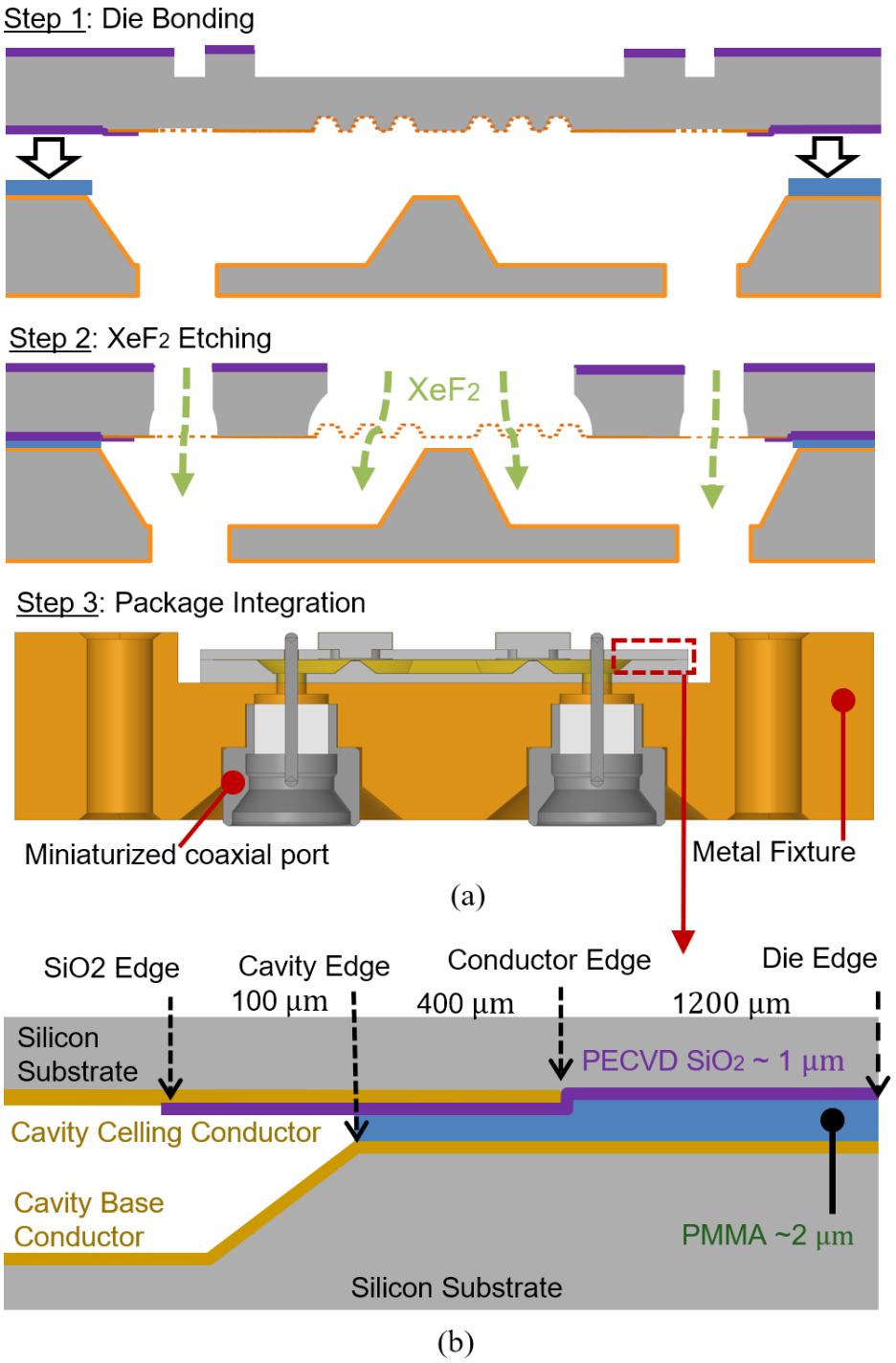

Fig. 4.11. (a) Die and package assembly flow, (b) Cross-section view of the die bonding junction.

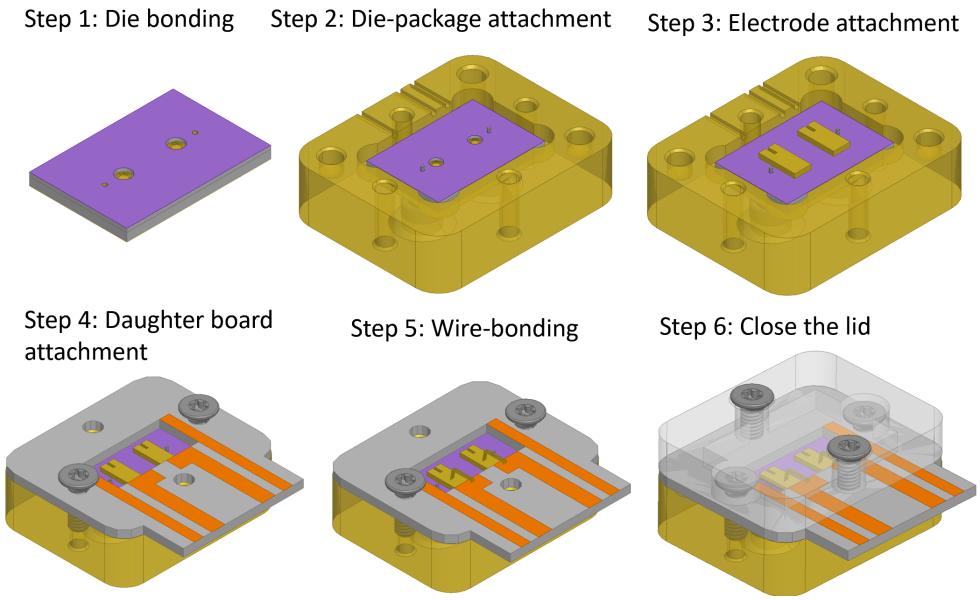

Fig. 4.12. Conceptual view of filter assembly flow.

compression bonding simplifies the die bonding process and is preferable since thermal compression bonding is a relatively complicated process.

4.4 Measurements

4.4.1 MEMS Tuning Performance

Fig. 4.14(a) shows the test setup for measuring the MCD force-deflection curve. A released diaphragm is placed on a PI 611 high precision Z stage (with a resolution of 0.1 μm). On top of the diaphragm center, there is a needle coupled with a force sensor (with a resolution of 1 μN). The Z stage gradually elevates the diaphragm and stops when the needle tip bends the diaphragm downwards by 18 μm. The software synchronously records the force and position data while the stage decreases, releasing the bent diaphragm with a step of 2 μm until zero force is observed. Fig. **??**(a) shows the measured data is in good agreement with the theoretical deflection predicted by (4.11). Comparing to the pure gold MCD reported in [13], the MCD becomes stiffer due to introducing vanadium elements.

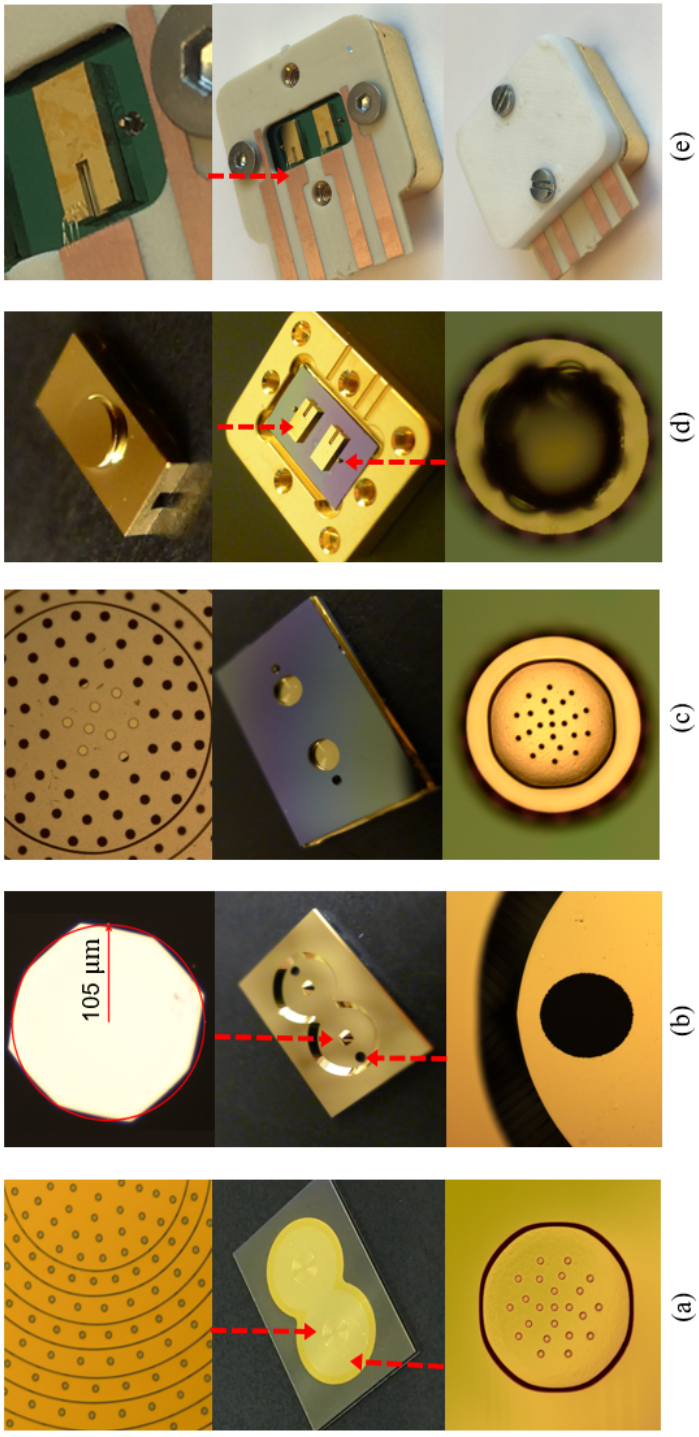

Fig. 4.13. (a) Photo of fabricated diaphragm, (b) Photo of fabricated cavity die, (c) Photo of sample after die-to-die bonding, (d) Photo of sample after package embedding, (e) Photo of sample final presentation.

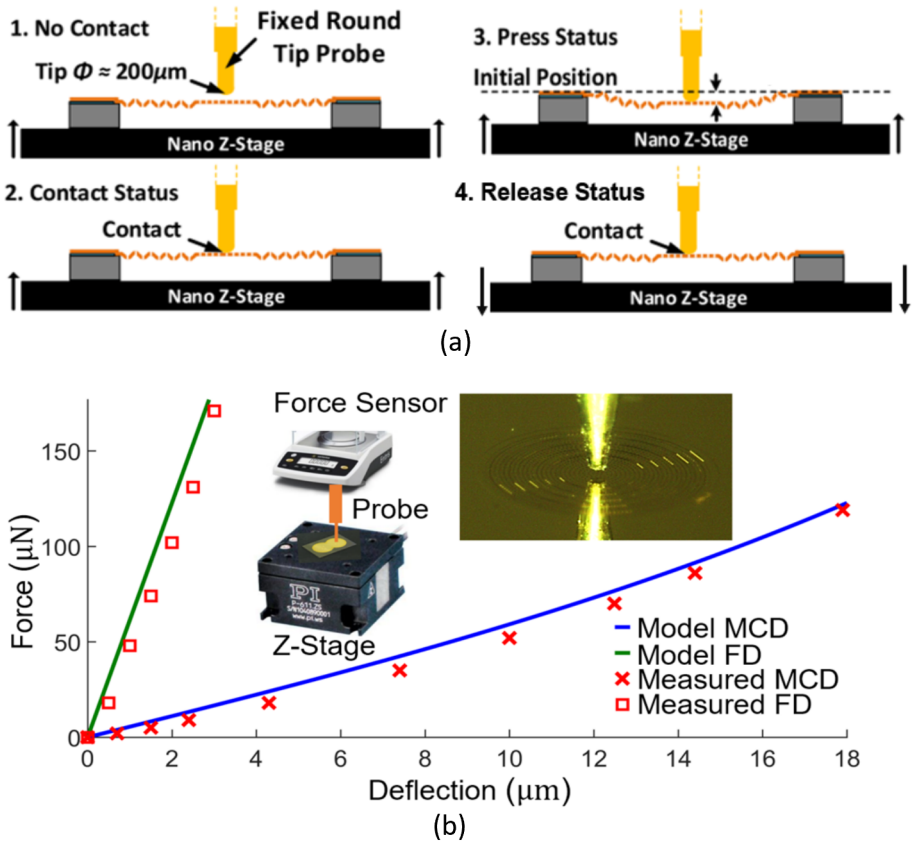

Fig. 4.14. (a) MEMS diaphragm bending characterization flow, (b) Measured diaphragm bending behavior: flat versus corrugated.

4.4.2 Filter RF Performance

An Agilent E8361A vector network analyzer measures the filters S-parameters. The measurements show the main frequency tuning range is 21.3–39.6 GHz and the corrective tuning range is 21.3–18.9 GHz. By fitting the HFSS simulation results, the extracted experimentally-achieved effective diaphragm deflections are 16.5 μm (main tuning) and 0.4 μm (corrective tuning). Fig. 4.15(b)(c) depicts the extracted frequency-displacement curve for the main tuning as well as for the corrective tuning, and both show good agreement with the analytical model.

As shown in Fig. 4.16, over the frequency tuning range, the measured filter bandwidth varies from 0.31–1.81 GHz and the measured insertion loss is 3.14–0.78 dB over the full

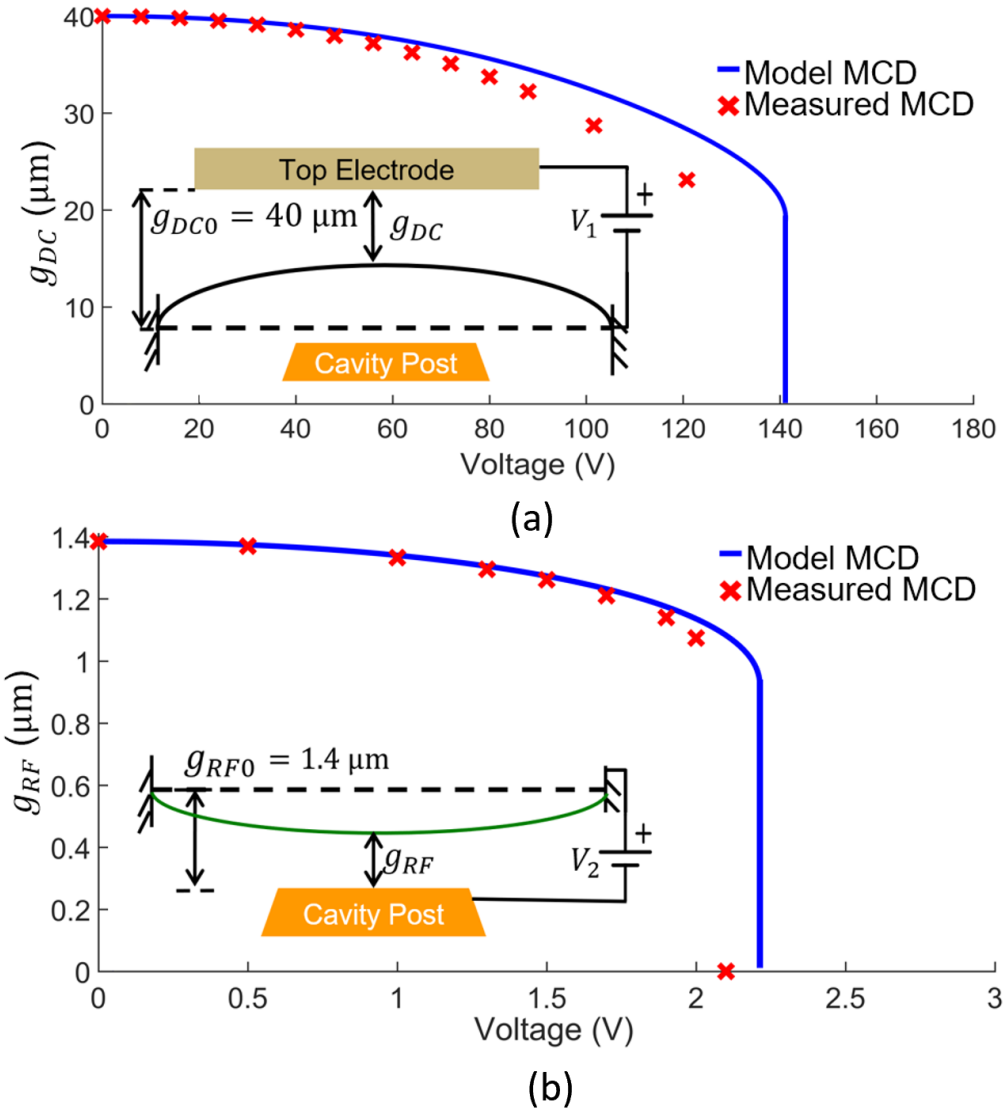

Fig. 4.15. (a) Measured main tuning performances, (b) Measured corrective tuning performances.

tuning range. As a proof of Fig. 4.16(b), the extracted MOM-sealed resonator quality factor is 265 to 510, which is comparable to the conventionally sealed resonator having the same cavity designs (Fig. 4.16(c)).

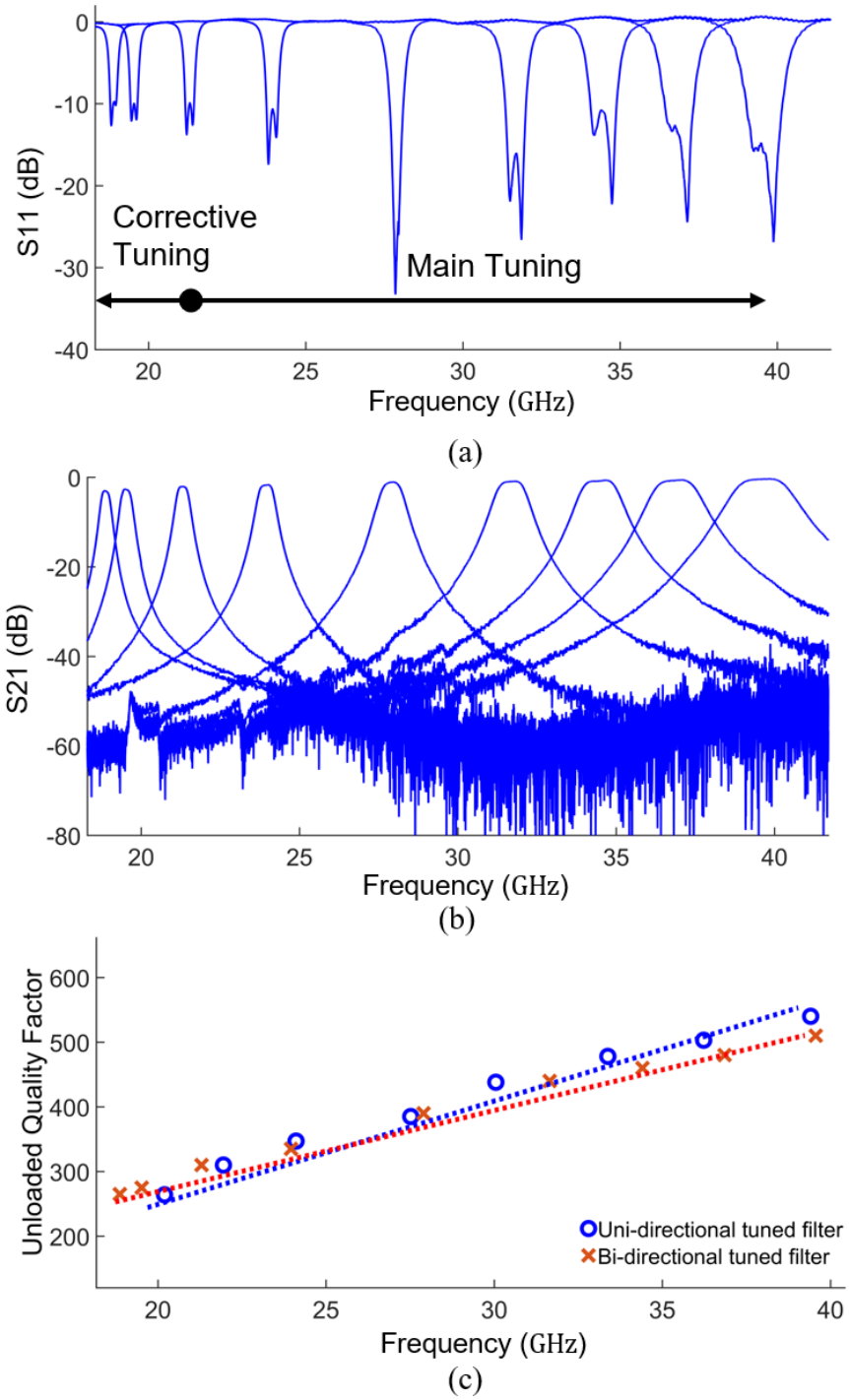

Fig. 4.16. (a) Measured bi-directional tunable EVA filter reflection coefficient, (b) Measured bi-directional tunable EVA filter transmission coefficient, (c) Measured bi-directional tunable EVA filter Q_u versus EVA technology with conventional tuner.

4.4.3 Tuning Stability Measurements

Using the same S-parameter measurement setup, frequency tuning stability experimental characterizations were performed. The setup records only one resonance extracted by the reflection coefficient, while placing the second filter resonance more than 10 GHz away from the resonance under test. Starting from the initial frequency (20 GHz), where the membrane is relaxed, a Keithley 2100 source meter supplies a bias voltage to drive the resonance to a designated frequency (32 GHz for this measurement). After 100 seconds, the bias voltage is set to 0 V, and the resonance frequency is recorded over time. The measured results show that there is a hysteresis effect that creates a time delay for the resonance to return to its original, unbiased frequency. Without reverse bias correction, it takes about 100 seconds to recover the RF gap from 1.5 μm to 1.4 μm. With corrective tuning, this hysteresis effect can be corrected by less than 2.5 V.

4.5 Conclusions

This paper presents a bi-directional tunable all-silicon MEMS EVA cavity filter and significantly extends this idea by introducing, for the first time, two key enabling technologies: a) a new metal-oxide-metal (MOM) sealed cavity that maintains high quality without requiring complicated metal bonding; and b) a new electrostatic bi-directional MEMS tuner that implements the needed frequency tuning without lowering the resonator quality factor. Furthermore, we explore important design and fabrication trade-offs regarding sensitivity to non-ideal effects (residual stress, fabrication imperfections). As a result, an optimal all-silicon manufacturing process is presented for the first time. The measured RF performance of a typical filter in the 20-40 GHz range is shown and is directly compared to the conventional uni-directional cavity-MEMS filters. Although both filters demonstrate the same measured RF performance and quality factor (approximately 250-500 for both of them), the new bi-directional design readily corrects the residual post-bias displacement of 0.1 μm by applying less than 2.5 V. Note that this displacement would otherwise lead to a

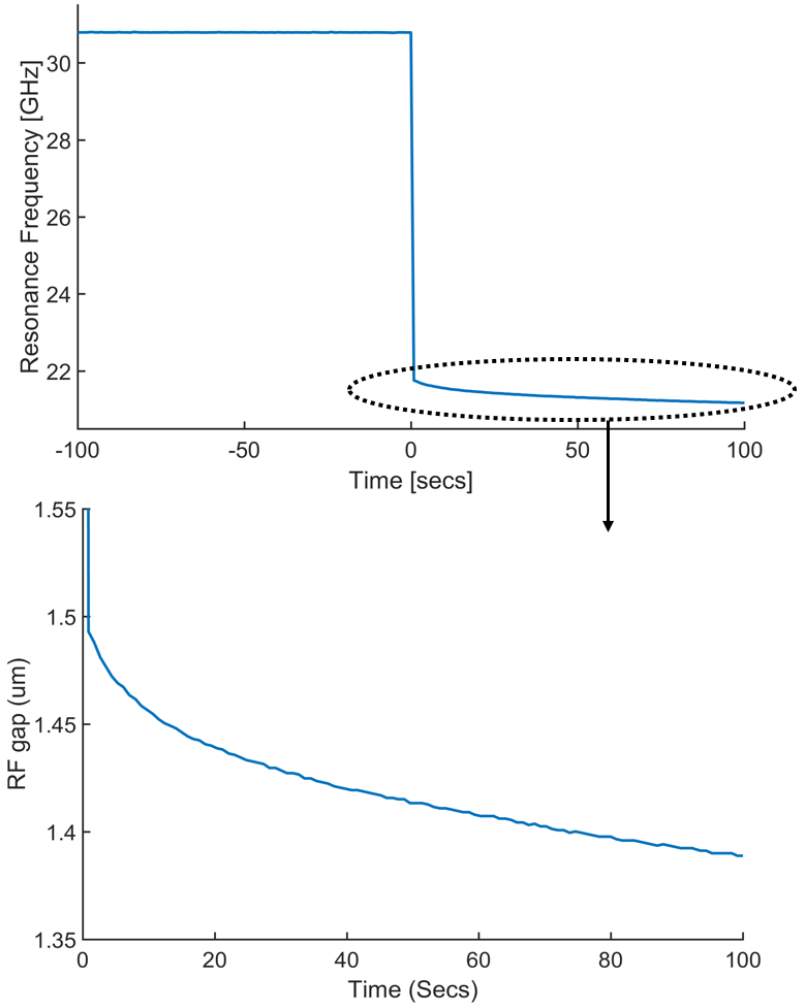

Fig. 4.17. Measured non-ideal filter tuning effect due to diaphragm visco-elasticity.

frequency drift of over 1 GHz. For the uni-directional case, it takes over 100 seconds to recover this error.

4.6 Related Publications

- **Z. Yang**, R. Zhang, and D. Peroulis, "Design and optimization of bi-directional tunable all-silicon evanescent-mode cavity filter" *IEEE Tran. Microw. Theory Tech.*, under review.

5. SUMMARY

The objective of this dissertation is to advance the state-of-art filter technology for next-generation front-ends. The evanescent-mode cavity resonator tunable filter has already demonstrated state-of-art performance in the C to L bands. MEMS tuned all-silicon EVA resonator proved that this concept is capable of being implemented at higher frequency bands, which are strong candidates for 5G communication standards.

Demonstration of high-performance EVA cavity filters is challenging due to the design and fabrication challenges from both the RF and MEMS aspects. Filter frequency tuning range and tuning stability are limited by MEMS tuner structural (stress, temperature) and material (creep, fatigue) stability. Filter RF performance such as Q_u, inter-resonator and external coupling, require careful design and optimization to accomplish low loss, small BW variation and impedance matching over wide tuning frequency range. Filter biasing voltage and package design are also critical for system-level compatibility.

In this dissertation, the author demonstrated the first K band high Q_u tunable filter with near octave tuning. The micro-corrugated diaphragm is incorporated to reduce bias voltage while increased MEMS diaphragm's tuning stability. Co-sputtered Au-V diaphragm, replaced pure gold, with engineered recipe further enhanced the tuning stability by 7×.

Analytical models and design techniques of the resonator, inter-resonator coupling and external-coupling are developed to optimize the filter performance under MEMS, and silicon micro-machining constraints. An optimized two-pole filer design is fabricated and the measurements demonstrated tuning range of 20-40GHz, relative bandwidth 1.9%-4.7%, and full tuning range impedance matching.

Lastly, the filter technology is further advanced by employing a bi-directional tuner. Such bi-directional tunability enables effective voltage compensation over the full tuning range. Such design does not introduce significant fabrication complexity. Furthermore, no RF performance degradation is observed by the proposed RF optimization method. A

detailed RF-MEMS co-design, and optimization flow of the implemented MEMS micro-corrugated diaphragm that maximizes the tunability under certain RF, biasing, and fabrication limitations are discussed. A proof-of-concept, two-pole filter is fabricated and demonstrates a measured bi-directional tuning range from 18.9 to 39.6 GHz, in which the forward (main) actuation tunes from 21.3 to 39.6 GHz with 120 V and the reverse (corrective) actuation tunes from 21.3 down to 18.9 GHz with 2 V. The measured filter insertion loss varies from 3.14 to 0.78 dB and its instantaneous bandwidth from 0.31 to 1.81 GHz. The unloaded quality factor is extracted as 265–510 which is comparable to the state-of-the-art filter of this type employing conventional uni-directional tuners. Frequency hysteresis effect of the device is characterized, and such non-ideal effect is correctable with less than 2.5V.

5.1 Comparison with State-Of-The-Art Results

The MEMS enabled all-silicon EVA tunable filter design of this work builds upon the all-silicon concept that was first presented in [34] and was further advanced into a tunable filter in [13]. However due to the proposed filter design methodology, this work exhibits 22% wider tuning range, 1.9× lesser bandwidth variation and 2× wider impedance matching as well as acceptable matching over the entire tuning range. Furthermore, the frequency stability of this work is significantly improved by employing creep-resistive Au-V diaphragm that exhibits 7× slower frequency drift rate than pure Au diaphragms [13]. A more complete comparison with alternative 3D tunable bandpass filters is summarized in Table 5.1. As can be seen, the filter presented in this work exhibits the highest tunability (100%) which is significantly higher than filters based on conventional cavities (e.g. [10, 60–62]) whose tunability is less than 5%. Such tunability also outperforms other EVA tunable filers, such as for example, the ones in [26], [62]. This is because the integrated MEMS tuner is capable of providing capacitance variation of over 10-to-1.

Moreover, the presented filter offers the most compact cavity volume. This conclusion is based on calculating the wavelength-normalized resonator volume at the lowest achievable frequency.

$$\overline{Volume_R} = \frac{ResonatorVolume}{(\lambda_L)^3} \tag{5.1}$$

where λ_L is the wavelength at the lower edge of the band (20 GHz in our case).

We can also observe that the filter in this work outperforms all filters listed in the table especially for the non-EVA cavity implementations [10], [9], [60–62]. In addition, [60] is demonstrated by manual—potentially motorized—tuning. In addition, the tuning of [61, 62] involves air-pressure actuation and step-motor system respectively. These actuation solutions typically occupy larger volumes making the overall filter size much larger than the filter architecture in this work. Lastly, the filter of this work demonstrates the highest FOM among all other filter technologies. Note that the FoM of the tunable filter is defined as in [63] and is summarized as

$$FoM = \frac{f_H - f_L}{\sqrt{BW_H BW_L IL_H IL_L}} \tag{5.2}$$

where f_H, f_L are the highest and lowest achieved filter center frequencies, BW_H, BW_L, IL_H, IL_L are bandwidths and insertion losses at the highest and lowest tuned frequencies.

Table 5.1.
Performance Comparison of K-band MEMS Tunable Filters

Work	Freq, GHz	FBW,%	IL, dB	Q_u	Order	Filter Technology	Tuning,%	$\overline{Volume_R}$	FoM, dB^{-1}
[10]	21.5-22.25	4.4-4.7	0.8-1.3	500-650	4	Waveguide (MEMS)	3.48	0.2036	0.73
[60]	19.7-19.9	0.3	1.1	12000	4	Waveguide (Manual)	1	0.3099	3.36
[61]	94-96.59	4.1-4.3	2.36-2.4	400	2	Waveguide (MEMS)	2.8	0.1935	0.26
[62]	19.7-20.2	1	0.2-0.22	15500-16000	6	Cavity (Step Motor)	2.5	5.8105	11.9
[64]	4.07-5.58	0.8-1.1	3.18-4.91	354-400	2	EVA (MEMS)	37.1	0.0019	8.66
[26]	63.2-67.4	3.4-8.3	1.4-5	68-108	2	EVA (MEMS)	6.6	0.0125	0.45
[9]	4.64-4.82	0.4-0.5	1.03-2.1	510-1220	2	DR Cavity (MEMS)	3.9	0.0059	5.38
This work	20-40	1.9-4.7	0.8-2.9	264-540	2	EVA (MEMS)	100	0.0018	15.54

$\overline{Volume_R}$ is the normalized volume of single resonator derived as (5.1)

5.2 List of Original Accomplishments Described in This Dissertation

1. First demonstrated K-Ka band MEMS tunable all silicon cavity filter with high Q_u (550–750) and wide frequency range 23-35GHz.

2. First implemented micro-corrugated diaphragm into the EVA cavity filter and demonstrated 80% of bias voltage reduction.

3. Show characterized EVA cavity filter cycling performance of more than 1 billion cycles without failure.

4. Enhanced filter tuning stability (7×) by using a co-sputtered Au-V diaphragm.

5. Developed new analytical models and design guidelines of the all-silicon resonator to optimize Q_u with tuner design constraints.

6. First developed analytical models and design guideline of all-passive inter-resonator coupling structure to achieve lowest frequency dispersion.

7. Proposed a full passive external feeding structure which is integrated into the filter package to tailor the input/output coupling strength.

8. Demonstrated an EVA cavity tunable filter with largest frequency range 20 to 40 GHz with least fractional bandwidth variation ranging from 1.9% to 4.7% and impedance matching over the whole tuning range.

9. First enabled bi-directional electro-statical tuning an EVA cavity tunable filter without RF performance degradation nor MEMS structural complications.

5.3 Future Work

The first challenge that can be explored in the future is further reducing the form factor. The tunable EVA filter technology demonstrated in this work comes with a metallic package housing coaxial connectors. To further reduce its form factor, a planar RF input/output feeding structure is preferable to allow direct flip-chip bonding of filter die on the PCB board. Nevertheless, novel impedance machine structures are required. Impedance matching over an octave tuning range is typically very challenging for planar feeding structures. On the other hand, antenna size has similar frequency dependency as a filter. High-efficiency antenna demands a significant amount of area. Integration front end elements such as patch antennas on the same filter die will make volume even better utilized and more cost-effective.

The second aspect that can be explored is the mechanical structure of the corrugated diaphragm. Due to the limitation of fabrication technology, in this work, the corrugations only exist on one side of the diaphragm center plane. Such structural asymmetry bends the diaphragm under intrinsic stress exists. Such a problem can be fully addressed if employing symmetrically corrugated diaphragm. Diaphragm of this type will remain flat as long as the stress is tensile. Such design may be realized by using two types of photo-resist as sacrificial layers.

The third direction worth studying is the filter design automation by machine learning algorithms. There are a few tens of independent design parameters involved in this design work. Despite the developed design flows typically requires many iterations to reach the optimal design for given specifications. It is feasible to automatically generate and simulate a great number of test samples with variations of design parameters then using a machine learning algorithm to do the training. Once the model is converged, the whole design and optimization can be fully automated to significantly reduce the design lead time.

The last interesting point to experiment is enabling open-loop filter tuning control scheme by the machine learning algorithm. Despite the fact that bi-directional tuning provides full range tuning correction capability, sensing of the RF gap with high-resolution

during filter operation remains a challenge. Employing open-loop control is the ultimate goal to make such technology cost effective. Machine learning is a promising technology worth to experiment with on this application. During the training process, the actual diaphragm position can be correlated to the biasing voltage. If the training set is sufficiently large, the trained model can eventually predict the bias voltage for a given target frequency.

REFERENCES

REFERENCES

[1] P. Bahramzy, P. Olesen, P. Madsen, J. Bojer, S. Caporal, D. Barrio, A. Tatomirescu, P. Bundgaard, A. S. Morris, and G. F. Pedersen, "A tunable RF front-end with narrowband antennas for mobile devices," *IEEE Trans. Microw. Theory Tech.*, vol. 63, no. 10, pp. 3300–3310, 2015.

[2] T. C. Lee, J. Lee, and D. Peroulis, "Dynamic bandpass filter shape and interference cancellation control utilizing bandpass-bandstop filter cascade," *IEEE Trans. Microw. Theory Tech.*, vol. 63, no. 8, pp. 2526–2539, 2015.

[3] Y. Shim, Z. Wu, and M. Rais-Zadeh, "A high-performance continuously tunable MEMS bandpass filter at 1 GHz," *IEEE Trans. Microw. Theory Tech.*, vol. 60, no. 8, pp. 2439–2447, 2012.

[4] C. C. Cheng and G. M. Rebeiz, "High-Q 4-6-GHz suspended stripline RF MEMS tunable filter with bandwidth control," *IEEE Trans. Microw. Theory Tech.*, vol. 59, no. 10, pp. 2469–2476, 2011.

[5] W. Tang and J.-S. Hong, "Varactor-tuned dual-mode bandpass filters," *IEEE Trans. Microw. Theory Tech.*, vol. 58, no. 8, pp. 2213–2219, 2010.

[6] J. Ni and J.-S. Hong, "Compact varactor-tuned microstrip high-pass filter with a quasi-elliptic function response," *IEEE Trans. Microw. Theory Tech.*, vol. 61, no. 11, pp. 3853–3859, 2013.

[7] R. Stefanini, M. Chatras, A. Pothier, C. Guines, and P. Blondy, "High-Q 3D tunable RF MEMS filter with a constant fractional bandwidth," in *Proc. 8th Eur. Microw. Integr. Circuits Conf.*, Nuremberg, Germany, 2013, pp. 1–4.

[8] K. Entesari and G. M. Rebeiz, "A 12-18-GHz three-pole RF MEMS tunable filter," *IEEE Trans. Microw. Theory Tech.*, vol. 53, no. 8, pp. 2566–2571, 2005.

[9] W. D. Yan and R. R. Mansour, "Tunable dielectric resonator bandpass filter with embedded MEMS tuning elements," *IEEE Trans. Microw. Theory Tech.*, vol. 55, no. 1, pp. 154–159, 2007.

[10] L. Pelliccia, F. Cacciamani, P. Farinelli, P. Ligander, and O. Persson, "High-Q MEMS-tunable waveguide filters in K-band," in *42nd Eur. Microw. Conf.*, Amsterdam, The Netherlands, 2012, pp. 273–276.

[11] J.-R. Mao, W.-W. Choi, K.-W. Tam, W. Q. Che, and Q. Xue, "Tunable bandpass filter design based on external quality factor tuning and multiple mode resonators for wideband applications," *IEEE Trans. Microw. Theory Tech.*, vol. 61, no. 7, pp. 2574–2584, 2013.

[12] Y. Zheng, M. Sazegar, H. Maune, X. Zhou, J. R. Binder, and R. Jakoby, "Compact substrate integrated waveguide tunable filter based on ferroelectric ceramics," *IEEE Microw. Wirel. Components Lett.*, vol. 21, no. 9, pp. 477–479, 2011.

[13] Z. Yang and D. Peroulis, "A 23-35 GHz MEMS tunable all-silicon cavity filter with stability characterization up to 140 million cycles," in *IEEE MTT-S Int. Microw. Symp. Dig.*, Tampa, USA, 2014, pp. 1–3.

[14] M. D. Hickle, M. D. Sinanis, and D. Peroulis, "Tunable high-isolation W-band bandstop filters," in *IEEE MTT-S Int. Microw. Symp. Dig.*, Phoenix, USA, 2015, pp. 1–4.

[15] A. J. Alazemi and G. M. Rebeiz, "A low-loss 1.4-2.1 GHz compact tunable three-pole filter with improved stopband rejection using RF-MEMS capacitors," in *IEEE MTT-S Int. Microw. Symp. Dig.*, San Francisco, USA, 2016, pp. 1–4.

[16] M. A. El-Tanani and G. M. Rebeiz, "High-performance 1.5-2.5-GHz RF-MEMS tunable filters for wireless applications," *IEEE Trans. Microw. Theory Tech.*, vol. 58, no. 6, pp. 1629–1637, 2010.

[17] K. Y. Lee and G. M. Rebeiz, "A miniature 8-16 GHz packaged tunable frequency and bandwidth RF MEMS filter," *2009 IEEE Int. Symp. Radio-Frequency Integr. Technol. RFIT 2009*, pp. 249–252, 2009.

[18] S. S. Attar, S. Setoodeh, P. D. Laforge, M. Bakri-Kassem, and R. R. Mansour, "Low temperature superconducting tunable bandstop resonator and filter using superconducting RF MEMS varactors," *IEEE Trans. Appl. Supercond.*, vol. 24, no. 4, 2014.

[19] F. Huang, S. Fouladi, and R. R. Mansour, "High-Q tunable dielectric resonator filters using MEMS technology," *IEEE Trans. Microw. Theory Tech.*, vol. 59, no. 12, pp. 3401–3409, 2011.

[20] S. Fouladi, F. Huang, W. D. Yan, and R. R. Mansour, "High-Q narrowband tunable combline bandpass filters using MEMS capacitor banks and piezomotors," *IEEE Trans. Microw. Theory Tech.*, vol. 61, no. 1, pp. 393–402, 2013.

[21] D. Peroulis, E. Naglich, M. Sinani, and M. Hickle, "Tuned to resonance: transfer-function-adaptive filters in evanescent-mode cavity-resonator technology," *IEEE Microw. Mag.*, vol. 15, no. 5, pp. 55–69, 2014.

[22] P. Blondy and D. Peroulis, "Handling RF power: the latest advances in RF-MEMS tunable filters," *IEEE Microw. Mag.*, vol. 14, no. 1, pp. 24–38, 2013.

[23] L. Pelliccia, P. Farinelli, V. Nocella, F. Cacciamani, F. Gentili, and R. Sorrentino, "Discrete-tunable high-Q E-plane filters," in *43rd Eur. Microw. Conf.*, Nuremberg, Germany, 2013, pp. 1215–1218.

[24] H. Joshi, H. H. Sigmarsson, D. Peroulis, and W. J. Chappell, "Highly loaded evanescent cavities for widely tunable high-Q filters," in *IEEE MTT-S Int. Microw. Symp. Dig.*, Honolulu, Hawaii, 2007, pp. 1–4.

[25] E. J. Naglich, J. Lee, H. H. Sigmarsson, D. Peroulis, and W. J. Chappell, "Intersecting parallel-plate waveguide loaded cavities for dual-mode and dual-band filters," *IEEE Trans. Microw. Theory Tech.*, vol. 61, no. 5, pp. 1829–1838, 2013.

[26] D. Psychogiou, D. Peroulis, Y. Li, and C. Hafner, "V-band bandpass filter with continuously variable centre frequency," *IET Microwaves, Antennas Propag.*, vol. 7, no. 8, pp. 701–707, 2013.

[27] J. Small, M. S. Arif, A. Fruehling, and D. Peroulis, "A tunable miniaturized RF MEMS resonator with simultaneous high Q (500-735) and fast response speed (< 10-60 μs)," *J. Microelectromechanical Syst.*, vol. 22, no. 2, pp. 395–405, 2013.

[28] R. Stefanini, J. D. Martinez, M. Chatras, A. Pothier, V. E. Boria, and P. Blondy, "Ku band high-Q tunable surface-mounted cavity resonator using RF MEMS varactors," *IEEE Microw. Wirel. Components Lett.*, vol. 21, no. 5, pp. 237–239, 2011.

[29] X. Liu, L. P. B. Katehi, W. J. Chappell, and D. Peroulis, "High-Q tunable microwave cavity resonators and filters using SOI-based RF MEMS tuners," *J. Microelectromechanical Syst.*, vol. 19, no. 4, pp. 774–784, 2010.

[30] ——, "Power handling of electrostatic MEMS evanescent-mode (EVA) tunable bandpass filters," *IEEE Trans. Microw. Theory Tech.*, vol. 60, no. 2, pp. 270–283, 2012.

[31] M. S. Arif and D. Peroulis, "All-silicon technology for high-Q evanescent mode cavity tunable resonators and filters," *J. Microelectromechanical Syst.*, vol. 23, no. 3, pp. 727–739, 2014.

[32] M. S. Arif, W. Irshad, X. Liu, W. J. Chappell, and D. Peroulis, "A high-Q magnetostatically-tunable all-silicon evanescent cavity resonator," in *IEEE MTT-S Int. Microw. Symp. Dig.*, Baltimore, USA, 2011, pp. 1–4.

[33] W. Irshad and D. Peroulis, "A 12-18 GHz electrostatically tunable liquid metal RF MEMS resonator with quality factor of 1400-1840," in *IEEE MTT-S Int. Microw. Symp. Dig.*, Baltimore, USA, 2011, pp. 1–4.

[34] M. S. Arif and D. Peroulis, "A 6 to 24 GHz continuously tunable, microfabricated, high-Q cavity resonator with electrostatic MEMS actuation," in *IEEE MTT-S Int. Microw. Symp. Dig.*, Montreal, Canada, 2012, pp. 1–3.

[35] P. Scheeper, W. Olthuis, and P. Bergveld, "The design, fabrication, and testing of corrugated silicon nitride diaphragms," *J. Microelectromechanical Syst.*, vol. 3, no. 1, pp. 36–42, mar 1994.

[36] D. Zhang, B. Tang, Y. Cheng, and K. Sato, "Fast Si (100) etching with a smooth surface near the boiling temperature in surfactant-modified tetramethylammonium hydroxide solutions," *Micro Nano Lett.*, vol. 9, no. 9, pp. 582–584, 2014.

[37] P. Pal, K. Sato, M. A. Gosalvez, Y. Kimura, K.-i. Ishibashi, M. Niwano, H. Hida, B. Tang, and S. Itoh, "Surfactant adsorption on single-crystal silicon surfaces in TMAH solution : orientation-dependent adsorption detected by in situ infrared spectroscopy," *J. Microelectromechanical Syst.*, vol. 18, no. 6, pp. 1345–1356, 2009.

[38] C. W. Tan and J. Miao, "Optimization of sputtered Cr/Au thin film for diaphragm-based MEMS applications," *Thin Solid Films*, vol. 517, no. 17, pp. 4921–4925, 2009.

[39] E. Higurashi, D. Chino, and T. Suga, "Au-Au Surface-activated bonding and its application to optical microsensors with 3-D structure," *IEEE J. Sel. Topitcs QUANTUM Electron.*, vol. 15, no. 5, pp. 1500–1505, 2009.

[40] M. McLean, W. L. Brown, and R. P. Vinci, "Temperature-dependent viscoelasticity in thin Au films and consequences for MEMS devices," *J. Microelectromechanical Syst.*, vol. 19, no. 6, pp. 1299–1308, 2010.

[41] M. T. Lin, R. R. Chromik, N. Barbosa, P. El-Deiry, S. Hyun, W. L. Brown, R. P. Vinci, and T. J. Delph, "The influence of vanadium alloying on the elevated-temperature mechanical properties of thin gold films," *Thin Solid Films*, vol. 515, no. 20-21, pp. 7919–7925, 2007.

[42] C. Palego, J. Deng, Z. Peng, S. Halder, J. C. M. Hwang, D. Froehand, D. Scarbrough, C. L. Goldsmith, I. Johnston, S. K. Sampath, and A. Datta, "Robustness of RF MEMS capacitive switches in harsh environments," in *IEEE Trans. Microw. Theory Tech.*, vol. 57, no. 12, 2009, pp. 3262–3269.

[43] J. Li and A. Dasgupta, "Failure-mechanism models for creep and creep rupture," *IEEE Trans. Reliab.*, vol. 42, no. 3, pp. 339–353, 1993.

[44] M. Abu Khater and D. Peroulis, "Real-time feedback control system for tuning evanescent-mode cavity filters," *IEEE Trans. Microw. Theory Tech.*, vol. 64, no. 9, pp. 2804–2813, 2016.

[45] D. M. Pozar, *Microwave engineering*. New York, NY, USA: Wiley, 2005.

[46] H. H. Sigmarsson, "Widely tunable, high-Q, evanescent-mode cavity filters: Fabrication, control, and reconfigurability," Ph.D. dissertation, Purdue University, 2010.

[47] E. M. Popescu and S. Song, "Trapezoidal waveguides: first-order propagation equivalence with rectangular waveguides," *J. Phys. A Math. Theor.*, vol. 40, no. 48, pp. 14 555–14 574, 2007.

[48] G. F. Craven and C. K. Mok, "The design of evanescent mode waveguide bandpass filters for a prescribed insertion loss characteristic," *IEEE Trans. Microw. Theory Tech.*, vol. 19, no. 3, pp. 295–308, 1971.

[49] C. K. Mok, "Design of evanescent-mode waveguide diplexers," *Trans. Microw. Theory Tech.*, vol. 21, no. 1, pp. 43–48, 1973.

[50] J.-C. Nanan, J.-W. Tao, H. Baudrand, B. Theron, and S. Vigneron, "A two-step synthesis of broadband ridged waveguide bandpass filters with imporoved performances," *IEEE Trans. Microw. Theory Tech.*, vol. 39, no. 12, pp. 2192–2197, 1991.

[51] N. Marcuvitz, *Waveguide handbook*. Stevenage, UK: IET, 1951.

[52] J.-S. Hong, *Microstrip filters for RF/microwave applications*. New York, NY, USA: WILEY, 2011.

[53] J. Li, Z. Yang, D. Psychogiou, M. D. Sinanis, and D. Peroulis, "Creep-resistant nanocrystalline gold-vanadium alloyed microcorrugated diaphragms (MCDS)," in *Transducers*, Anchorage, USA, 2015, pp. 1–4.

[54] Y.-c. Wu, M. A. Khater, and D. Peroulis, "Real-time temperature compensation control system for tunable cavity-based high-Q filters," in *IEEE MTT-S Int. Microw. Symp. Dig.*, Phoenix, AZ, 2015, pp. 1–3.

[55] A. Dec and K. Suyama, "Micromachined varactor with wide tuning range," *Electron. Lett.*, vol. 33, no. 11, pp. 922–924, 1997.

[56] D. Peroulis, S. P. Pacheco, K. Sarabandi, and L. P. B. Katehi, "Electromechanical considerations in developing low-voltage RF MEMS switches," *IEEE Trans. Microw. Theory Tech.*, vol. 51, no. 1 II, pp. 259–270, 2003.

[57] S. L. March, "Analyzing lossy radial-line stubs," *IEEE Trans. Microw. Theory Tech.*, vol. 33, no. 3, pp. 269–271, mar 1985.

[58] Z. Yang and D. Peroulis, "A 20-40 GHz tunable MEMS bandpass filter with enhanced stability by gold-vanadium micro-corrugated diaphragms," in *IEEE MTT-S Int. Microw. Symp. Dig.*, San Francisco, USA, 2016, pp. 1–3.

[59] M. Füldner, A. Dehé, and R. Lerch, "Analytical analysis and finite element simulation of advanced membranes for silicon microphones," *IEEE Sens. J.*, vol. 5, no. 5, pp. 857–863, 2005.

[60] C. Arnold, J. Parlebas, and T. Zwick, "Reconfigurable waveguide filter with variable bandwidth and center frequency," *IEEE Trans. Microw. Theory Tech.*, vol. 62, no. 8, pp. 1663–1670, 2014.

[61] F. Sammoura and L. Lin, "Micromachined W-band polymeric tunable iris filter," *Microsyst. Technol.*, vol. 17, no. 3, pp. 411–416, 2011.

[62] B. Yassini, M. Yu, and B. Keats, "Ka-Band fully tunable cavity filter," *IEEE Trans. Microw. Theory Tech.*, vol. 60, no. 12, pp. 4002–4012, 2012.

[63] V. Pleskachev and I. Vendik, "Figure of merit of tunable ferroelectric planar filters," in *33rd Eur. Microw. Conf. EuMC 2003*, vol. 1, Munich, Germany, 2003, pp. 191–194.

[64] S. J. Park, I. Reines, C. Patel, and G. M. Rebeiz, "High-Q RF-MEMS 4–6 GHz tunable evanescent-mode cavity filter," *IEEE Trans. Microw. Theory Tech.*, vol. 58, no. 2, pp. 381–389, 2010.

VITA

VITA

ZhengAn Yang born in Hangzhou, China. He received his B.S. degree in Electrical Engineering at Purdue University West Lafayette in 2009 then joined Ph.D. program and worked with Prof. Dimitrios Peroulis as a graduate research assistant. His research topics include mm-wave RF device design, MEMS design, micro-fabrication, and measurement automation. His works were recognized as the finalist and won the third place award of IEEE MTT-S IMS Student Paper Competition in 2014 and 2017 respectively. He was also the recipient of the 2nd Place Award of IEEE MTT-S IMS Student Design Competition on switchable RF-MEMS filter in 2016. Since Jan. 2017, he joined Qualcomm Techology Inc. working as a senior hardware engineer.